EXPERIMENTAL TESTS OF GAUGE THEORIES

G. Barbiellini
Laboratori Nazionali di Frascati, INFN, Frascati, Italy.

1. INTRODUCTION

The principle of local gauge invariance for the Lagrangian of the free particles (the free spinors, for example) fixes the interaction between the spin ½ particles and the gauge field (spin 1 particles). The form of the interaction is obtained by replacing in the Lagrangian the momentum operator (∂_μ) by the covariant derivative [for Quantum Electrodynamics (QED): $\partial_\mu \to D_\mu = \partial_\mu + iqA_\mu$].

The introduction of the gauge field through the covariant derivative (or generalized momentum) established the Lorentz structure of the interaction. The gauge field A_μ transforms under the Lorentz group as the vector ∂_μ.

This is evident in electrodynamics where all the experimental phenomena are well described by the free charged particle Lagrangian applying the gauge principle that defines the vector potential. Evidence for the vector nature of most of the other known interactions (weak and strong interactions) has been growing for many years owing to the results of many ingenious experiments. In Sections 2 and 3 I present the recent results on elementary particle physics, which support the most general properties of the gauge theories, such as

i) The Lorentz nature of the gauge interaction.

ii) The universality of the weak coupling constant that derives from the non-Abelian gauge nature of the symmetry of the weak-interaction Lagrangian.

The enormous amount of information collected on weak charged-current (CC) and neutral-current (NC) interactions is also valid support for the most popular gauge theory of the electroweak interaction: the standard model of Glashow, Salam and Weinberg (GSW) based on the $SU(2)_L$ symmetry for the weak isodoublet and the U(1) symmetry of the weak hypercharge. Awaiting the discovery of the predicted intermediate vector bosons (IVB) of the weak interaction and the measurement of their mass and spin, the experiments that probe the Lorentz structure of the weak interaction are spin-correlation or angular-distribution measurements. The following reactions (some of them well investigated in the past and improving continuously, and some others only very recently experimentally discovered) are the main support for the V,A nature of the weak interaction and for the universal coupling of the spinors of different flavours to the IVB.

i) *Purely leptonic interactions*

Decay	Scattering	
$\mu \to \nu_\mu \bar{\nu}_e e$	$\nu_\mu e^- \to \mu^- \nu_e$	(CC)
$\tau \to \nu_\tau \bar{\nu}_\ell \ell$	$\nu e \to \nu e$	(NC)
	$e\bar{e} \to \begin{cases} e\bar{e} \\ \mu\bar{\mu} \\ \tau\bar{\tau} \end{cases}$	

ii) *Semileptonic interactions*

Decay	Scattering	
$\pi(K) \to \{^{\mu\nu}_{e\nu}$	$(\bar{\nu})_\mu "q" \to \mu^{\pm} X$	(CC)
	$(\bar{\nu})_\mu "q" \to (\bar{\nu})_\mu X$	(NC)
$D(B) \to \ell \bar{\nu}_\ell X$	$e(\mu) "q" \to e'(\mu') X$	
	$e\bar{e} \to q\bar{q}$	

Sections 2 and 3 on the electroweak interaction will end with a review of the limit imposed by the present experimental errors on some alternative theory to the standard model (SM) as, for instance, the left-right symmetric model based on the $SU(2)_R \times SU(2)_L \times U(1)$ group.

The impressive amount of experimental data collected in strong-interaction experiments supports the hypothesis that the underlying theory for these interactions is also a local gauge theory based on the SU(3) invariance of the degree of freedom that characterizes the "hadron": the colour -- red, blue and yellow.

Sections 4 and 5 contain a review of some relevant experiments that have attempted a verification of QCD. While in the lectures by Landshoff the theoretical difficulties of formulating precise numerical predictions from QCD theory have been discussed, in this experimental review the main emphasis will be on the limitations found by working on the experiments supposed to produce decisive tests on QCD. Section 6 is devoted to the description of the tremendous experimental effort that is being put into the search for the baryon number violation, which is the astonishing prediction of the most ambitious gauge theory -- the Grand Unified Theory (GUT).

As seen in the lectures by Peccei, the coupling constants of the known gauge theories $SU(3)_c$, $SU(2)_L \times U(1)$, g_1, g_2, and g_3 evolve with the interaction energy and show a possible unification point at very high energy. If the unification of the g_i is not accidental, there is the possibility that the three interactions at the unification energy obey a simple symmetry group G that contains $SU(3)_c$ $SU(2)_L$ $U(1)$. The symmetry of G is broken at different energy scales to give more restrictive symmetry of the Lagrangian; the only exact symmetries that survive at low energies are $SU(3)_c$ and U(1) of electromagnetism (EM). In some formulations of the GUT, for example SU(5), the baryon number is not conserved and there is a prediction for the proton decay and its lifetime of $\tau = 10^{29\pm2}$ yr.

The large value τ predicts a new very rare radioactivity of matter. A series of sophisticated experiments, using massive and heavily instrumented targets, are in progress or are projects to accomplish the difficult task of detecting the energy release of $\sim$ 1 GeV caused by a proton decay, inside a population of more than 10^{30} nucleons, at a frequency of $\sim$ one event per year.

2. HELICITY CONSERVATION IN VECTOR AND AXIAL-VECTOR CURRENT-CURRENT INTERACTIONS

The helicity is the relativistic analogy of the spin and is the projection of the four-vector

$$S_p = \left(\vec{\xi} + \frac{(\vec{p}\cdot\vec{\xi})\,\vec{p}}{m(m+E)} , \vec{p}\cdot\vec{\xi} \right)$$

along the direction of the four momentum p. Here, $\vec{\xi}$ = angular momentum on the particle rest frame and m,E = particle mass and energy, respectively. It is relatively simple to show that vector (V), and axial vector (A) interactions conserve helicity, while scalar (S) and pseudoscalar (PS) interactions flip the helicity.

Let us recall briefly the derivation of the helicity conservation in the V and A interactions. For the Dirac spinors, the kinetic term of the Lagrangian is

$$\mathcal{L}_{kin} = \bar{f}\,\gamma\,\frac{\partial}{\partial x}\,f = \bar{f}\,\gamma\,\frac{\partial}{\partial x}\left[\frac{1}{2}(1-\gamma_5)+\frac{1}{2}(1+\gamma_5)\right]f$$

Using the following property of the γ_5 matrix:

$$(1 \pm \gamma_5)(1 \pm \gamma_5) = 2\,(1 \pm \gamma_5)$$

we get

$$\mathcal{L}_{kin} = \bar{f}_L\,\gamma\,\frac{\partial}{\partial x}\,f_L + \bar{f}_R\,\gamma\,\frac{\partial}{\partial x}\,f_R$$

where

$$f_L = \frac{1}{2}(1-\gamma_5)f\,;\quad f_R = \frac{1}{2}(1+\gamma_5)f$$

Since the V and A interactions have the same Lorentz structure as the operator ∂_μ, their application produces in the Lagrangian the creation of a left-handed spinor and the annihilation of a right-handed antispinor, or vice versa for an initial right-handed spinor.

In the same way it is easy to show that the S and PS interactions flip the helicity as follows:

$$f\bar{f} = \bar{f}_L f_R + \bar{f}_R f_L$$

Scalar and pseudoscalar interactions cannot be introduced by the principle of local gauge invariance.

The previous property of V, A, S, and PS interactions can be memorized graphically with the help of the following diagrams:

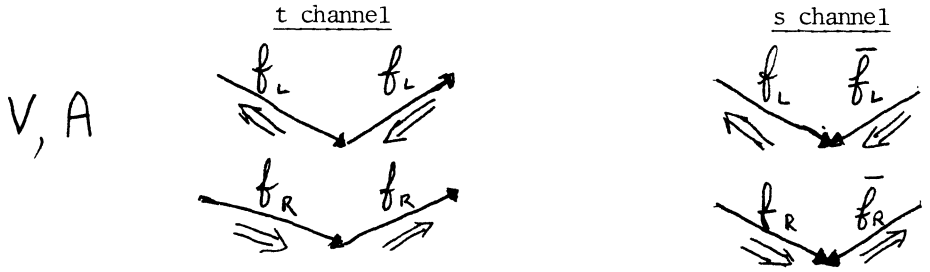

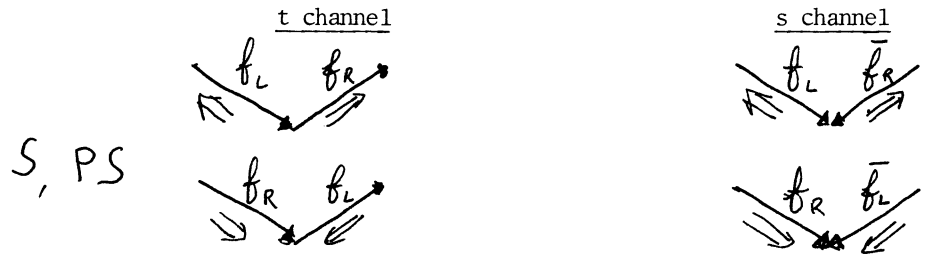

2.1 Experimental measurement of the μ^+ polarization in charged-current muon-antineutrino nucleon interactions

The measurement of the helicity of positive muons produced in neutrino reactions at high Q^2 solves the problem of whether the CC is only V and A interactions or a mixture of S, P, and T (tensor) simulating the same inelasticity distribution ($y = E_h/E$) as predicted for V and A. The μ^+ from the reaction

$$\bar{\nu}_\mu \, Fe \longrightarrow \mu^+ + X \qquad (1)$$

are expected to have the same helicity as the incoming $\bar{\nu}_\mu$ beam for V and A interactions. The helicity of the $\bar{\nu}_\mu$ is determined by the zero (or small) mass of the neutral lepton, by angular momentum conservation, and by the measured μ^+ polarization in the pion decay:

$$\pi^- \longrightarrow \mu^- \bar{\nu}_\mu \qquad (2)$$

The measurement of the μ^+ polarization from reaction (1) requires three major components:

i) An intense $\bar{\nu}_\mu$ beam.

ii) A massive target where the antineutrino-induced CC reactions take place.

iii) A polarimeter to measure the μ^+ polarization.

The intense $\bar{\nu}_\mu$ beam is provided by the so-called Wide Band Beam (WBB) of the CERN SPS.

As shown schematically in Fig. 1, the WBB of $\bar{\nu}_\mu$ is produced in the following way: the high-intensity proton beam ($\sim 10^{13}$ protons per pulse) accelerated at 400 GeV in the SPS is directed onto a beryllium target. The secondary pion and kaon produced in the (pBe) interaction are sign-selected and focused in a parallel beam by an achromatic (momentum-independent) system of lenses (the Van der Meer horns). The parallel beam of charged particles is drifted in an empty region ($\sim$ 300 m long), where a certain fraction of π and K decay mainly through the channels $\pi(K) \rightarrow \bar{\nu}_\mu \mu^-$. At the end of the decay tunnel a massive shielding of iron and earth absorbs the muons before they reach the region of the active neutrino detectors. The energy spectrum of the (anti)neutrino beams crossing the detector is shown in Fig. 2.

A tiny fraction of the neutrino beam interacts with the small cross-section (0.4×10^{-38} E cm^2 GeV^{-1}) in the instrumented iron focusing spectrometer magnet and hadron calorimeter of the CERN-Dortmund-Heidelberg-Saclay (CDHS) Collaboration.

The CDHS apparatus behaves as an active target, measures the kinematical variables of reaction (1), and absorbs the hadron shower. The penetrating μ^+, for a given range of energy, reach the Amsterdam-CERN-Hamburg-Moscow-Rome (CHARM) apparatus where their polarization is analysed. The orientation of the μ^+ spin is measured by a spin precession in a weak magnetic field (58 G) and through the behaviour of the backward-forward asymmetry of decay positrons versus time. The experiment is shown schematically in Fig. 3a. The experimental data are expressed by

$$R(t) = \frac{N_B(t) - N_F(t)}{N_B(t) + N_F(t)} = R_0 \cos(\omega t + \Phi) + R_1$$

where $N_{B(F)}(t)$ is the number of detected positron decays, backward or forward, relative to the incoming μ^+ direction, ω is the angular velocity of the spin precession and Φ is the phase related to the sign of the polarization. In the figure is shown the behaviour of R(t) versus time for a time interval $t \simeq 3\tau$ (where τ is the muon lifetime). The experimental points (Fig. 3b) start from $t > 1$ μs owing to different time restrictions applied at the data collection and analysis level. The fit of the sinusoidal behaviour of R(t) gives the following result:

$$R_0 = 0.11 \pm 0.03 \qquad \Phi = -3.03 \pm 0.09$$

The quantity R_0 is related to the μ^+ polarization $[P(\mu^+)]$ through the parameters describing the μ^+ decay

$$\mu^+ \rightarrow e^+ \nu_e \bar{\nu}_\mu$$

and to the slowing down of the μ^+ in the polarimeter material. The result on $P(\mu^+)$ is derived by the measurement of R_0 and the calculation relating $P(\mu^+)$ to R_0. The μ^+ polarization value experimentally measured is

$$P(\mu^+) = 0.80 \pm 0.07\,(stat) \pm 0.14\,(syst)$$

From this $P(\mu^+)$ value the following limit for the S, P, and T interactions in CC antineutrino-induced reactions is derived: $\sigma_{S,P,T}/\sigma_{tot} < 0.22$ at the 95% confidence level (CL). The average momentum transfer of the CC interaction is $Q^2 = 4.5$ GeV/c^2.

The same analysis can be carried out for different data subsets in the bin of y (the inelasticity E_h/E_ν). The results are shown in Fig. 4. The same events are also presented as a function of x and Q^2 in Figs. 4b and c. Since at $y = 0$ the eventual contributions to σ of the S and P interactions vanish, normalizing $P(\mu^+)$ to 1 at $y = 0$, the fit to the value of $P(\mu^+)$ versus y gives the highest sensitivity to possible S and P contributions to CC antineutrino interactions. From the results shown in Fig. 5 the following limit to the S and P contributions is derived:

$$\sigma_{S,P}/\sigma_{tot} \leq 7\% \quad \text{at } 95\% \text{ C.L.}$$

The previous results extend to the semileptonic reaction at a high Q^2 value the very stringent limits on S and P contributions to weak processes derived by the accurate study of the μ decay.

2.2 Universality of the charged-current coupling in lepton decay

The muon decay has been in the past and -- with the advent of the new high-intensity low-energy machines (the pion factory) -- is still at present an important field for the investigation of the weak interaction. The muon has only one decay allowed by energy and leptonic flavour conservation

$$\mu \rightarrow \nu_\mu \, e \, \bar{\nu}_e$$

The muon decay has been thoroughly studied both theoretically and experimentally.

Since the muon decay is the corner stone of all possible weak CC decays, including the "superweak" proton decay, it is a useful exercise to recall the main steps in computing the muon lifetime.

The general effective Lagrangian of the four fermions participating in the muon decay is

$$\mathcal{L} = \frac{G}{\sqrt{2}} \left[(\bar{e} O_\alpha \nu)(\bar{\nu} O_\alpha \mu) + (\bar{\mu} O_\alpha \nu)(\bar{\nu} O_\alpha e) \right]$$

G is the Fermi constant and the symbols e, μ, and ν represent the spinor wave functions of the different leptons. The operator O_α for the V - A interaction is

$$O_\alpha = \gamma_\alpha (1 + \gamma_5)$$

From this Lagrangian and the phase-space factor for the three-body final state, the following differential decay width is derived:

$$d W = \frac{(2\pi)^2 |M|^2}{E_\mu} \frac{d^3 \vec{K}}{(2\pi)^3 E} \frac{d^3 \vec{q}_1}{(2\pi)^3 \omega_1} \frac{d^3 \vec{q}_3}{(2\pi)^3 \omega_2} \delta^4 (K + q_1 + q_2 - p)$$

where

$(\vec{K},E) \equiv$ electron four-momentum

$(\vec{q}_1,\omega_1) \equiv$ (anti)neutrino four-momentum

$M \equiv (G/2)(\bar{e} O_\alpha \mu)(\bar{\nu} O_\alpha \nu)$.

The integration over all the neutrino variables and the electron angular distribution gives

$$d W = \frac{G^2 \mu^5}{96 \pi^3} (3 - 2x) x^2 dx$$

where x is the reduced electron energy ($x = 2E/\mu$) and μ is the muon mass. After integration over x

$$\tau_\mu = \frac{1}{W} = \frac{1}{\int \frac{dW}{dx} dx} = \frac{192 \pi^3}{G^2 \mu^5}$$

Experimentally

$\tau_\mu = (2.197120 \pm 0.00007)10^{-6}$ s (Particle properties data book)

$\tau_\mu = (2.196950 \pm 0.00006)10^{-6}$ s (New measurement at the TRIUMPH accelerator)

the high-precision measurement of τ gives the following value for the Fermi coupling constant

$$G = (1.16637 \pm 0.00002) \times 10^{-5} \text{ Gev}^{-2}$$

The μ meson is the heavy brother of the electron, the difference being only the mass and a new quantum number, the lepton flavour, which is introduced to account for the experimental observation that $\mu \to e\gamma$ is highly forbidden. The partial width for the $\mu \to e\gamma$ decay is

$$B = \frac{\Gamma(\mu \to e\gamma)}{\Gamma(\mu \to \nu_\mu e \bar{\nu}_e)} \leq 2 \times 10^{-10}$$

2.3 The τ meson

Since the discovery of the τ meson at the e^+e^- storage ring SPEAR in 1975 the problem of the lepton generation has been widened from the mystery of two unexplained families to that of three generations.

All the experimental information collected on the τ heavy "lepton" (which is a contradiction in words) is in agreement with a universal V - A coupling for its CC decay and with the existence of a new species of neutrino, the ν_τ. The lepton-flavour conservation forbids the decay otherwise allowed by energy conservation and the spin-statistics relation

$$\tau \to e\bar{e}e \quad , \quad \tau \to \mu\bar{\mu}\mu$$

The direct evidence for ν_τ is still missing, but the hypothesis of the existence of three families of left doublets responsible for the purely leptonic CC interaction

$$\begin{pmatrix} \nu_e \\ e \end{pmatrix}_L \quad , \quad \begin{pmatrix} \nu_\mu \\ \mu \end{pmatrix}_L \quad , \quad \begin{pmatrix} \nu_\tau \\ \tau \end{pmatrix}_L$$

is largely accepted.

The point-like nature of the third lepton is proved at the same level of "elementarity" as that of the muon by the beautiful PETRA and PEP experiments on the reactions

$$e\bar{e} \to \mu\bar{\mu} \quad , \quad e\bar{e} \to \tau\bar{\tau}$$

that will be reviewed later. The universality of the V - A coupling has been experimentally established, recently, by the measurement of the τ lifetime.

The most precise measurement of the τ lifetime has been obtained with an improved version of the Mark II experiment at SLAC (the Mark II detector is directly derived from the Mark I, the apparatus where the τ heavy lepton was discovered).

The measurement of the lifetime of short-lived particles is today an important experimental issue; it is worth while spending some time to study the Mark II τ lifetime measurement in detail. The value theoretically expected for the τ lifetime is computed according to the weak-interaction universality by scaling the muon lifetime for the differences in mass and considering the many possible decay channels open to the τ decay owing to its mass value.

The τ mass is $M_\tau = 1.784$ GeV. The known τ decays and their branching ratios are given in Table 1.

Table 1

τ decay channels

Decay channel	Branching ratio (B) (%)
$\tau \to \mu\nu\nu$	17
$\tau \to e\nu\nu$	17
$\tau \to \pi\nu$	22
$\tau \to \pi\nu$	8
$\tau \to 3\pi\nu + m\pi^0$	15.3
$\tau \to 5\pi\nu$	< 0.7

Let us consider the purely leptonic τ decay $\tau \to e\bar{\nu}_e\nu_\tau$ analogous to the $\mu \to e\bar{\nu}_e\nu_\mu$ decay. The τ lifetime is computed in the following ways:

$$W(\tau \to e\,\bar{\nu}_e\,\nu_\tau) = \frac{G^2 M_\tau^5}{192\pi^3}$$

$$W(\tau \to all) = W(\tau \to e\,\bar{\nu}_e\,\nu_\tau)\,\frac{W(\tau \to all)}{W(\tau \to e\,\bar{\nu}_e\,\nu_\tau)}$$

$$\tau_\tau = \frac{1}{W} = \frac{1}{W(\tau \to e\,\bar{\nu}_e\,\nu_\tau)} \cdot B_{e\,\bar{\nu}_e\,\nu_\tau} = 2.85\ 10^{-13}\ \text{sec}$$

The mean free path of the τ lepton is $c\tau\beta\gamma$ and corresponds to $\sim$ 700 μm at the present storage-rings energy. The measurement of such short decay paths is done only with specialized detectors such as nuclear emulsions or solid-state chambers with very high space accuracy. These techniques are not of simple application in e^+e^- storage-ring experiments, where the τ pairs to be studied are produced in relatively large quantities. So the τ lifetime measurement is done by improving the space resolution of the conventional wire chambers, and the lifetime is measured on a statistical basis over the large sample of τ that can be collected in the storage rings.

At the e^+e^- storage rings the τ production is due to the annihilation process $e^+e^- \to \tau^+\tau^-$. The cross-section for the previous point-like process is

$$\sigma(e\bar{e} \to \tau\bar{\tau}) = \sigma(e\bar{e} \to \mu\bar{\mu}) = \frac{4\pi\alpha^2}{3s^2} = \frac{88}{s}\ \text{nb GeV}^{-2}$$

where s is the square of the total centre-of-mass energy. For a collected luminosity of $\sim 30\ \text{pb}^{-1}$ at $s = 900\ \text{GeV}^2$, about 3000 reactions (3b) are produced.

2.4 The experimental technique

The τ lifetime is measured by finding the vertex of the three-prong τ decay product from the decay $\tau \to \pi\pi\pi$ and measuring the flight distance between the interaction point and the τ vertex projected along the τ momentum.

Figure 6 shows the geometry of the reaction. The position of the beams is taken at the origin O, the vertex position is measured at V, and $\vec{\mu}$ is the normalized τ momentum $\vec{\mu} = \vec{p}/E_{beam}$. The problem is to measure $\ell = c\tau\beta\gamma \simeq 3 \times 10^{10} \times 2.8 \times 10^{-13} \times 15/1.78 = 7.1 \times 10^{-2}$ cm, when the errors on V and O are of the order of 0.1 cm.

The value ℓ can be determined only statistically and not on the single-event basis. To use the full statistical power reduction coming from the large sample of events collected to evaluate the final value of ℓ, the systematic errors have to be under control at the desired level of the statistical error. Many tests to verify and control the systematic errors have been done on the beam position measured with other processes. The distribution is given in Fig. 7. Unfolding this distribution with the computed distribution for particles with zero lifetime one gets

$$\ell = (710 \pm 120)\ \mu\text{m}$$

From this value, after radiative correction [change of γ since $\langle E_\tau \rangle \leq E_{beam}$] and correction for hadron contamination, the following value of the lifetime is derived:

$$\tau_\tau = (3.31 \pm 0.57 \pm 0.60) \times 10^{-13}\ \text{sec}$$

in good agreement with the prediction obtained assuming the universality of the Fermi coupling G, whose value is precisely measured in the muon lifetime experiment.

2.5 Universality of the neutral-current coupling and the standard model

The universality of the NC interaction comes as for the CC interaction from the charge carried by the IVB. The charge is transferred with the same value from one flavour line to the other. The non-Abelian nature of the $SU(2)_L$ symmetry of the weak interaction predicts the universal strength for the NC as well as for the CC interactions.

The physical IVB exchanged in NC is a linear mixing of the gauge field W_μ^3 of the $SU(2)_L$ and the gauge field B_μ of the U(1) symmetry. The two linear combinations are interpreted as the zero-mass photon and the massive physical Z^0. The effective coupling in NC reactions is universal in strength but changes from reaction to reaction according to the weak isospin and the charge of the particles involved in the process. Table 2 gives the relevant quantities to predict the NC coupling in the interaction involving the members of the first flavour generation ν, e, u, and d.

Table 2

Neutral current coupling

Particle	t	t_3	Y	Q	Z^0 coupling = $t_3 - Q \sin^2\theta$
ν_L	½	½	-1	0	½
ℓ_L	½	-½	-1	-1	$-½ + \sin^2\theta$
ℓ_R	0	0	-2	-1	$\sin^2\theta$
u_L	½	½	⅓	⅔	$½ - ⅔ \sin^2\theta$
d_L	½	-½	⅓	-⅓	$½ - ⅓ \sin^2\theta$
u_R	0	0	⅔	⅔	$-⅔ \sin^2\theta$
d_R	0	0	⅔	⅓	$⅓ \sin^2\theta$

An identical table is valid for the second (μ, s, c, ...) and third (τ, b, t, ...) flavour generations. Universality in NC implies flavour independence of the coupling constant given in the table.

2.6 Deep inelastic scattering of charged leptons on isoscalar targets and the electroweak interference

The deep inelastic scattering of charged leptons on nucleons at high energy and Q^2 is described by the following two graphs:

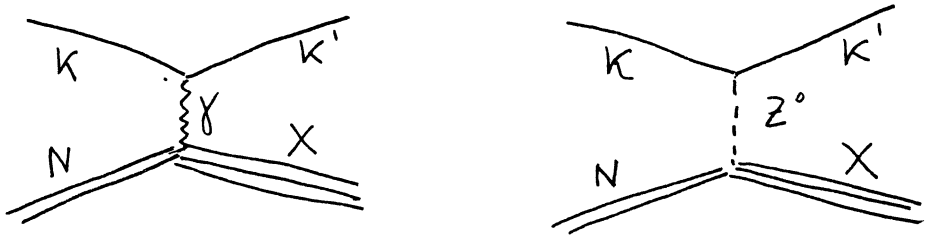

The kinematical variables defined by the lepton line are

$$Q^2 = 2KK'(1-\cos\theta)$$
$$\nu = K - K'$$

or the most common adimensional variables

$$x = Q^2/2M\nu$$
$$y = \nu/K$$

The cross-section due to the one-photon exchange is

$$\frac{d\sigma}{dQ^2 d\nu} = \frac{\pi\alpha^2}{4K^2\sin^4\frac{\theta}{2}}\frac{1}{KK'}\left[W_2\cos^2\frac{\theta}{2} + 2W_1\sin^2\frac{\theta}{2}\right]$$

where the $W_{1,2}$ represent the structure functions of the nucleon.

The celebrated experiment at SLAC on the deep inelastic electron-nucleon scattering suggested a particular dependence of $W_{1,2}$ on Q^2 and ν, the so-called scaling law. The behaviour of the $W_{1,2}$ functions stimulated the formation of the concept of a point-like object in the proton, the parton model, today identified with the quark parton model (QPM).

In this model the deep inelastic scattering is interpreted as an incoherent superposition of elastic scattering of the leptons on the quarks contained in the nucleon; each quark carries a fraction x of the nucleon momentum.

The cross-section of the elastic process $\ell q \to \ell q$ due to the photon exchange is

$$\frac{d^2\sigma}{dQ^2 d\nu} = \frac{\pi\alpha^2}{4K^2 \sin^4\frac{\theta}{2}} \frac{1}{K K'} \left[e_i^2 \cos^2\frac{\theta}{2} + \frac{e_i^2 Q^2}{4M^2x^2} 2\sin^2\frac{\theta}{2} \right] \delta\left(\nu - \frac{Q^2}{2Mx}\right)$$

If the substitutions

$$W_1^i = e_i^2 \frac{Q^2}{2M^2x^2} \delta\left(\nu - \frac{Q^2}{2Mx}\right)$$

$$W_2^i = e_i^2 \delta\left(\nu - \frac{Q^2}{2Mx}\right)$$

are introduced in the cross-section formula, this becomes:

$$\frac{d^2\sigma}{dQ^2 d\nu} = \frac{\pi\alpha^2}{4K^2 \sin^4\frac{\theta}{2}} \frac{1}{K K'} \left[W_2^i \cos^2\frac{\theta}{2} + W_1^i \sin^2\frac{\theta}{2} \right]$$

The nucleon form factors in this scheme are

$$W_1 = \sum_i \int_0^1 dx f_i(x) e_i^2 \frac{Q^2}{2M^2x^2} \delta\left(\nu - \frac{Q^2}{2Mx}\right)$$

$$W_2 = \sum_i \int_0^1 dx f_i(x) e_i^2 \delta\left(\nu - \frac{Q^2}{2Mx}\right)$$

Introducing the two form factors $F_{1,2}$ through the relation

$$F_1(Q^2,\nu) = W_1(Q^2,\nu); \quad F_2(Q^2,\nu) = \frac{\nu W_2(Q^2,\nu)}{M}$$

The following relation between F_1 and F_2 is derived

$$2x F_1(x) = F_2(x)$$

The previous derivations justify the hypothesis of the nucleon structure function in terms of the parton and give the relation (4) known as the Callan-Gross relation. This relation is a consequence of the spin ½ of the quark and is quite precisely verified in the experiment, giving support to the QPM.

3. THE ELECTROWEAK INTERFERENCE IN CHARGED LEPTON-NUCLEON SCATTERING

3.1 Polarized electron-deuteron scattering

Parity non-conservation in the deep inelastic scattering of longitudinally polarized electrons from unpolarized deuterons has been detected in the celebrated SLAC experiment at a value of the momentum transfer around 1 $(GeV/c)^2$. As seen before, the deep inelastic scattering is an incoherent superposition of elastic scattering of leptons on quarks (in the case of the deuteron nuclei there is the same amount of u and d quarks).

The graphs representing the polarized electron quark scattering are:

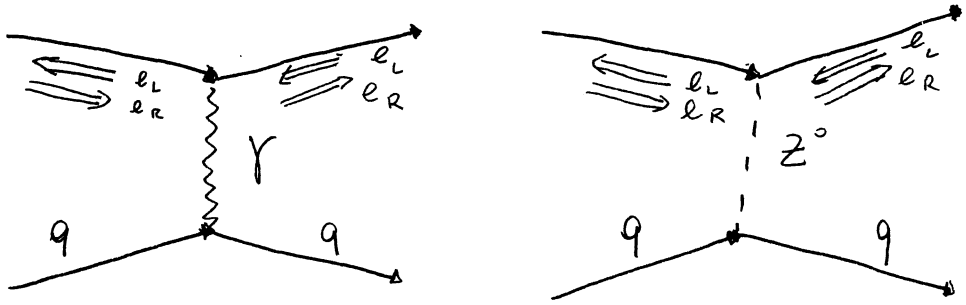

The EM electron-quark coupling is independent of the electron longitudinal polarization while the Z^0 quark coupling has different values for left-handed (e_L) and right-handed (e_R) electrons (Table 2). The quantity to be measured is the relative asymmetry

$$A = \frac{\sigma_R - \sigma_L}{\sigma_R + \sigma_L}$$

The deuteron is an isoscalar target and contains the same amount of u and d quarks.

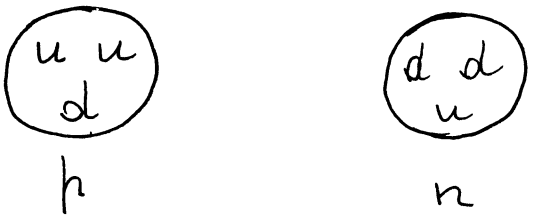

Let us compute the quantities $\sigma_{R,L}$ considering the elementary subprocesses on the quarks u and d, and applying the helicity rules.

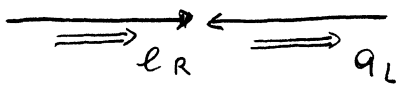

$(1-y)^2$

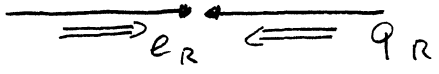

const.

$$\sigma_{e_R d_L} \alpha \left| \frac{1/3}{Q^2} + \frac{e_R d_L}{M^2} \right|^2 \times (1-y)^2$$

$$\sigma_{e_R u_L} \alpha \left| \frac{-2/3}{Q^2} + \frac{e_R u_L}{M^2} \right|^2 \times (1-y)^2$$

$$\sigma_{e_R d_R} \alpha \left| \frac{1/3}{Q^2} + \frac{e_R d_R}{M^2} \right|^2$$

$$\sigma_{e_R u_R} \left| \frac{-2/3}{Q^2} + \frac{e_R u_R}{M^2} \right|^2$$

At the value of momentum transfer squared (Q^2) of the SLAC experiment the quantity $\sigma_R + \sigma_L$ is dominated by the photon exchange. The quantity $\sigma_R - \sigma_L$ is given mainly by the $\gamma - Z^0$ interference term. Adding the u- and d-quark contributions the following expressions are derived for $\sigma_{R,L}$

$$\sigma_R \alpha \frac{5}{9} \frac{1}{Q^4}\left[1+(1-y)^2\right] + \frac{2}{3}\frac{e_R}{Q^2M^2}\left[(1-y)^2 q_L + q_R\right]$$

and

$$\sigma_L \alpha \frac{5}{9} \frac{1}{Q^4}\left[1+(1-y)^2\right] + \frac{2}{3}\frac{e_L}{Q^2M^2}\left[(1-y)^2 q_R + q_L\right]$$

where

$y = \nu/E_0$

$q_{L,R} = d_{L,R} - 2u_{L,R}$

$M = Z^0$ mass

E_0 = incoming electron energy.

The asymmetry is given by the following parity-violating expression:

$$A = \frac{3}{5}\frac{Q^2}{M^2}\left[e_R q_R - e_L q_L + \frac{(1-y)^2(e_R+e_L)(q_L-q_R)}{1+(1-y)^2}\right]$$

If the helicity couplings are expressed in terms of the weak angle, $\sin^2\theta$, the asymmetry becomes

$$A = BQ^2\left[a_1 + a_2\,\frac{1-(1-y)^2}{1+(1+y)^2}\right] \qquad (5)$$

where

$$B = \frac{9}{10}\,\frac{G}{2\sqrt{2\pi}\,\alpha} = 1.6\times10^{-4}\ \text{GeV}^{-2}$$

$$a_1 = 1 - 20/9\,\sin^2\theta$$

$$a_2 = 1 + 4\sin^2\theta$$

The experimental values of the asymmetries are shown in Fig. 8 versus y for different electron energies E_0. The results of the experiment are shown in Fig. 9 where the asymmetry values expected with the SM are also represented for different values of $\sin^2\theta$. The fit of the experimental data to the SM gives $\sin^2\theta = 0.224 \pm 0.020$.

3.2 Charge asymmetry in the deep inelastic muon-carbon scattering

The electroweak interference has been experimentally proved recently in the deep inelastic scattering of muons on carbon nuclei. The high-energy high-intensity CERN SPS muon beam allows the exploration of the effects at a Q^2 value of the order of 10^2 $(\text{GeV/c})^2$, where the asymmetry has a value of a few per cent. The quantity B measured by the Bologna-CERN-Dubna-Munich-Saclay (BCDMS) Collaboration working with the 200 GeV CERN muon beam on a 40 m long carbon target is

$$B = \frac{\sigma_L^+ - \sigma_R^-}{\sigma_L^+ + \sigma_R^-}$$

where

$$\sigma_L^+ \propto \left|\ \mu_L^+ \to \mu_L^+ + q \to q \ (\gamma) \ +\ \mu_L^+ \to \mu_L^+ + q \to q \ (Z^0)\ \right|^2$$

and the other σ have the obvious interpretation ($\pm$ for the muon charge, R,L for the muon helicity). The carbon nucleus is an isoscalar target with an equal number of u and d quarks. Let us apply the simple rule of helicity conservation in the elastic muon quark scattering to the following elementary processes

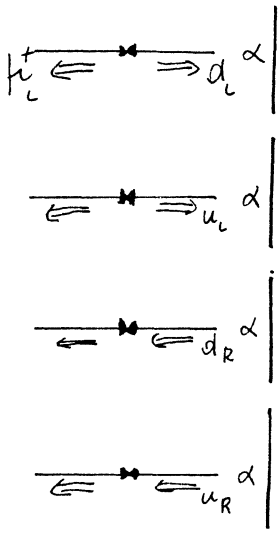

$$\left| -\frac{1/3}{Q^2} + \frac{1}{M^2}\,\mu_L^+ d_L \right|^2$$

$$\left| \frac{2/3}{Q^2} + \frac{1}{M^2}\,\mu_L^+ u_L \right|^2$$

$$\left| \frac{-1/3}{Q^2} + \frac{1}{M^2}\,\mu_L^+ d_R \right|^2 \times (1-y)^2$$

$$\left| \frac{2/3}{Q^2} + \frac{1}{M^2}\,\mu_L^+ u_R \right|^2 \times (1-y)^2$$

Neglecting the term proportional to $1/M^4$

$$\sigma_L^+ \propto \frac{10}{9}\frac{1}{Q^4} + \frac{2\,\mu_L^+}{Q^2M^2}\left[-\frac{1}{3}d_L + \frac{2}{3}u_L + (1-y)^2\left(\frac{-d_R}{3} + \frac{2u_R}{3}\right)\right]$$

$$\sigma_R^- \propto \frac{10}{9}\frac{1}{Q^4} + \frac{2\,\mu_R^-}{Q^2M^2}\left[\frac{1}{3}d_R - \frac{2}{3}u_R + (1-y)^2\left(\frac{d_L}{3} - \frac{2u_L}{3}\right)\right]$$

The expression for B in terms of the helicity couplings ($\mu_{R,L}$ and $q_{R,L}$) is

$$B = Q^2 K \frac{1+(1-y)^2}{1+(1-y)^2}\left(\mu_L^+ + \mu_R^-\right)\left[\left(d_R - d_L\right) - 2\left(u_R - u_L\right)\right]$$

The expression for B shows that the quantity is almost parity conserving since the quark term is axial vector and the dominant part of the μ term is also axial vector. A typical event of deep inelastic μC scattering as seen in the BCDMS apparatus is shown in Fig. 10. The radiative corrections to the raw data to evaluate the quantity B are quite important owing to the one-photon - two-photon interference. The value of B is presented in Fig. 11 for two muon momenta. The value of B is plotted versus the variable g(y), where

$$g(y) = \frac{1-(1-y)^2}{1+(1-y)^2}$$

The result of the fit gives the B slope

$$b = \left[-1.5 \pm 0.4\ (\mathrm{Stat}) \pm 0.16\ (\mathrm{Syst})\right] \times 10^{-4}$$

This result, if interpreted as a measurement of the third component of the μ^+ weak isospin, gives

$$I^{\mu^-}_{3R} = 0 \pm 0.07$$

proving that the muon, behaving in the NC weak interaction as the electron, forms a doublet $\binom{\nu}{\mu}_L$ if left-handed and a singlet when right-handed.

If the results on B are interpreted in terms of the SM the sensibility to the value of $\sin^2\theta$ is not large since the axial term dominates, but a value of $\sin^2\theta$ can be extracted plotting in the plane $a_\mu v_\mu$ the μC scattering data and the results on the muon asymmetry from the reaction $e^+e^- \to \mu^+\mu^-$ studied at the electron-positron storage rings. From Fig. 12 we get $v_\mu = -0.17 \pm 0.36$ and $\sin^2\theta_W = 0.21 \pm 0.09$. The value of $\sin^2\theta$ from the deep inelastic μC scattering has within experimental errors the same value as the one from the electron-deuteron scattering, proving the electron-muon universality in the NC interaction.

3.3 Neutrino-induced neutral current interaction on leptons and quarks

The scattering of muon neutrinos (ν_μ) on electrons (e) is of particular theoretical interest because of its simplicity. The $\nu_\mu e$ reaction involves only free point-like particles and its cross-section can be computed in the SM with high accuracy. Since the SM is a renormalizable theory, the higher order correction to the so-called Born approximation can be computed. The first-order graph for the $\nu_\mu e$ scattering is:

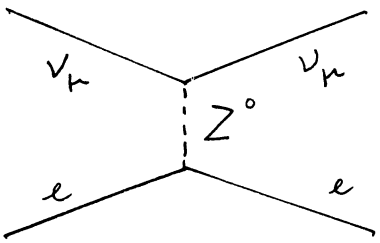

In computing the cross-section the (anti)neutrino masses are taken equal to zero. The helicity rule and the angular momentum conservation prescribe the behaviour either of the angular distributions or of the inelasticity $y = E_e/E_\nu$ of the scattered electron as follows:

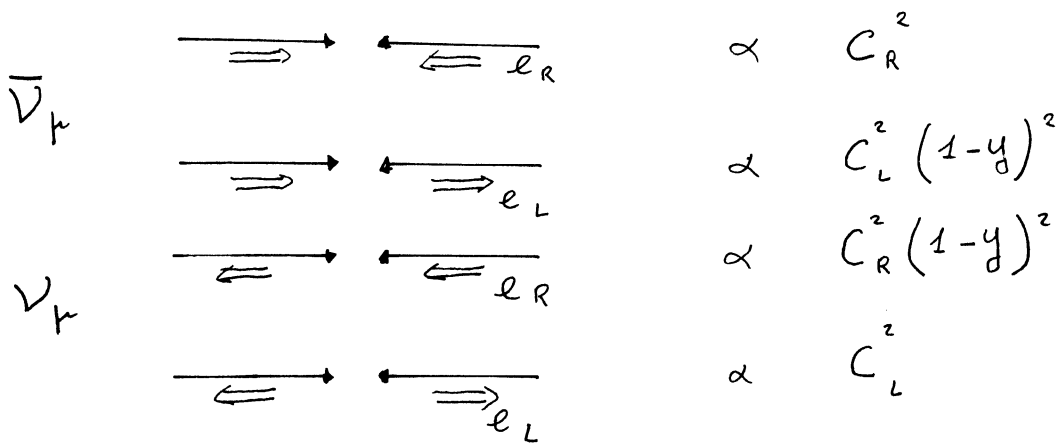

The differential ν and $\bar{\nu}$ electron cross-sections are

$$\frac{d\bar{\sigma}}{dy} = \frac{2G^2 E m}{\pi}\left[C_R^2 + C_L^2 (1-y)^2\right]$$

$$\frac{d\sigma}{dy} = \frac{2G^2 E m}{\pi}\left[C_L^2 + C_R^2 (1-y)^2\right]$$

where m is the electron mass and the terms $O(m/E_\nu)$ have been neglected. The integration on y from zero to one gives

$$\bar{\sigma} = \frac{2G^2 E m}{\pi}\left[C_R^2 + \frac{C_L^2}{3}\right]$$

$$\sigma = \frac{2G^2 E m}{\pi}\left[C_L^2 + \frac{C_R^2}{3}\right]$$

In the SM

$$C_L^2 = \frac{1}{2} - \sin^2\theta$$

$$C_R^2 = \sin^2\theta$$

The measurement of the ratio $R = \sigma/\bar{\sigma}$ allows the determination of the weak angle in a way that is independent of the value of the NC coupling and consequently that does not require the hypothesis of the minimal Higgs structure (Higgs isodoublet).

In terms of the helicity coupling

$$R = \frac{3C_L^2 + C_R^2}{3C_R^2 + C_L^2}$$

and expressed as a function of $\sin^2\theta$

$$R = 3\,\frac{1 - 4\sin^2\theta + 16/3\,\sin^4\theta}{1 - 4\sin^2\theta + 16\sin^4\theta}$$

The quantity R has been experimentally determined. The two cross-sections have been measured with a single apparatus at the CERN SPS neutrino beam.

The (anti)neutrino electron cross-section has been determined based on a sample of 46 ± 12 neutrino and 77 ± 19 antineutrino events induced in the CHARM fine-grain calorimeter by the horn-focused WBB. The few $\nu_\mu e$ scattering events are extracted from a total of 1.2×10^6 neutrino and 1.5×10^6 antineutrino interactions. The candidates are searched for amongst the muonless showers produced at small angle in respect to the beam direction.

The shower developments have the characteristics of an EM shower of high energy ($7.5 < E < 30$ GeV). The candidates are shown in Fig. 13, where their distribution is plotted versus $E^2\theta^2$. The main source of systematic error in the $\sigma(\bar{\sigma})$ cross-section determination comes from the background subtraction. The experimental result on R is

$$R = 1.37 \pm \begin{matrix} 0.65 \\ 0.44 \end{matrix}$$

In Fig. 14 is plotted the expected theoretical value of R versus $\sin^2\theta$ (dashed line). The experimental value of R compared with the full line (modification of R versus $\sin\theta$ due to the experimental acceptance) gives

$$\sin^2\theta = 0.215 \pm 0.04\,(\text{Stat}) \pm 0.015\,(\text{Syst})$$

3.4 Neutrino scattering on "quarks"

To a very good approximation the neutrino-nucleon as well as the electron-nucleon scattering is described by the point-like interaction of the lepton against the three valence quarks with the addition of a slowly varying amount of antiquark sea $[\alpha(Q^2)]$. At this stage the flavour mixing due to the Cabibbo angle can be neglected. The quark NC coupling is studied comparing the rate of muon (anti)neutrino-induced events without muons in the final state with that of the events induced by the CC interactions. The ratio of the two yields is almost independent from the uncertainties coming from the existence of the quark colour interaction to form the final bound state (hadrons). Assuming zero mass for ν ($\bar{\nu}$) and V - A types of interaction of the CC, the events have the following y distribution:

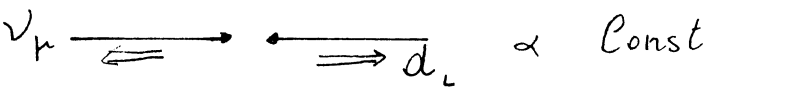

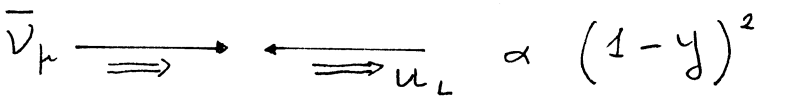

Introducing the fraction α of sea antiquarks, the CC y distribution is

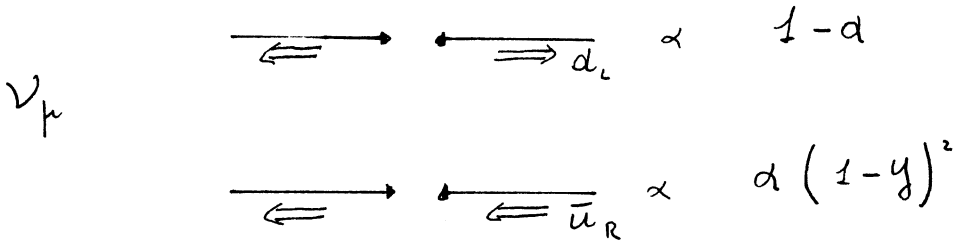

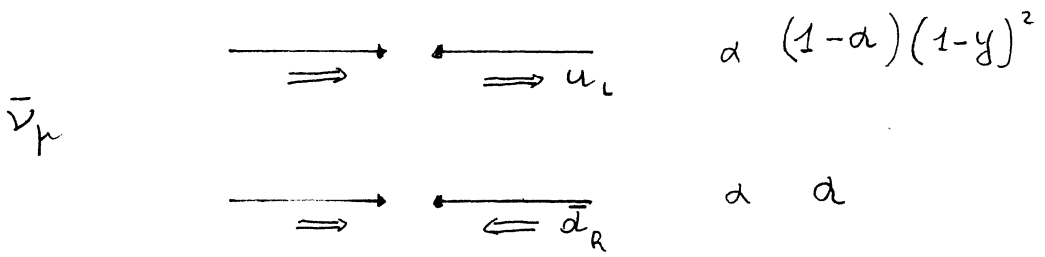

In the NC interactions the neutrinos communicate with both helicity quarks with different coupling. For an isoscalar target (u = d):

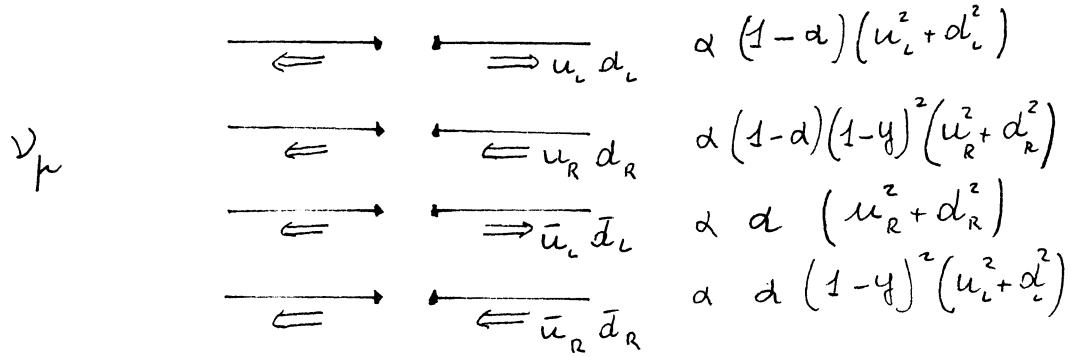

$$\sigma^{cc} \propto (1-\alpha) + \alpha (1-y)^2$$

$$\bar{\sigma}^{cc} \propto (1-\alpha)(1-y)^2 + \alpha$$

$$\sigma^{NC} \propto q_L^2 \left[(1-\alpha) + \alpha (1-y)^2\right] + q_R^2 \left[(1-\alpha)(1-y)^2 + \alpha\right]$$

$$\bar{\sigma}^{NC} \propto q_L^2 \left[(1-y)^2(1-\alpha) + \alpha\right] + q_R^2 \left[(1-\alpha) + \alpha (1-y)^2\right]$$

where $q^2_{L,R} = u^2_{L,R} + d^2_{L,R}$ for an isoscalar target.

After integration on y the cross-section becomes

$$\sigma^{cc} \propto 1 - 2/3\ \alpha$$

$$\bar{\sigma}^{cc} \propto 1/3 + 2/3\ \alpha$$

$$\sigma^{NC} \propto q_L^2\ (1 - 2/3\ \alpha) + q_R^2\ (1/3 + 2/3\ \alpha)$$

$$\bar{\sigma}^{NC} \propto q_L^2\ (1/3 + 2/3\ \alpha) + q_R^2\ (1 - 2/3\ \alpha)$$

Introducing the ratios R and $\bar{R}$ of the NC to CC cross-sections for neutrinos and antineutrinos,

$$R = \frac{\sigma^{NC}}{\sigma^{CC}} = q_L^2 + q_R^2 / \varepsilon$$

$$\bar{R} = \frac{\bar{\sigma}^{NC}}{\bar{\sigma}^{CC}} = q_L^2 + q_R^2 \times \varepsilon$$

$$\varepsilon = \frac{3 - 2a}{1 + 2a}$$

from the measured quantities R and $\bar{R}$ we derive the left- and right-handed quark coupling

$$q_L^2 = \frac{\varepsilon^2}{\varepsilon^2 - 1} \left(R - \bar{R} / \varepsilon^2 \right)$$

$$q_R^2 = \frac{\varepsilon}{\varepsilon^2 - 1} \left(\bar{R} - R \right)$$

In the SM q_L^2 and q_R^2 are related to $\sin^2 \theta$. The value of $\sin^2 \theta$ is measured in terms of R, $\bar{R}$, and the amount of sea quarks α.

The dependence on the sea quarks disappears in the ratio

$$R' = \frac{(\sigma - \bar{\sigma})^{NC}}{(\sigma - \bar{\sigma})^{CC}} = q_L^2 - q_R^2 = \rho \left(\frac{1}{2} - \sin^2 \theta \right)$$

where $\rho = M_W^2 / (M_Z^2 \cos^2 \theta) = 1$ in the SM.

Experimentally the measurement of R′ is more subject to systematic errors owing to the normalization error on the flux of the ν beams, while the two ratios R and $\bar{R}$ are flux independent.

The results from the recent analysis of the experimental data from the high-statistics electronics experiment on an isoscalar target (CHARM) keeping ρ as a free parameter are

$$\rho^2 = 1.02 \pm 0.023 \quad ; \quad \sin^2 \theta = 0.247 \pm 0.038$$

If ρ is fixed at the value $\rho = 1$ the CHARM data from the Narrow Band Beam (NBB) exposure give

$$\sin^2 \theta = 0.230 \pm 0.023$$

Figure 15 shows the neutrino (antineutrino) energy spectra of the NBB for a given value of the detector radius. The NBB is derived from a momenum-selected beam of π and K. The two-body decay of π and K of given momentum allows the correlation of the neutrino energy with the decay angle and so with detector radius. The two neutrino lines correspond to the different θ values in the π and K two-body decay

$$\pi \rightarrow \mu \nu \quad ; \quad K \rightarrow \mu \nu$$

Figure 16 shows the status of the measurement of R and $\bar{R}$ obtained from different detectors, including electronic calorimeters and bubble chambers.

3.5 Deep inelastic scattering of the neutrino (antineutrino) on protons and neutrons: charged current and neutral current

The deep inelastic scattering of neutrinos on an isoscalar target (u = d) gives information on the weak quark coupling $q^2 = u^2 + d^2$. The use of a hydrogen and a deuteron target is necessary to separate the u and d contributions.

The cross-sections for CC and NC reactions on protons (p) and neutrons (n), in terms of the quark couplings and neglecting the antiquark contribution, are given by the expressions:

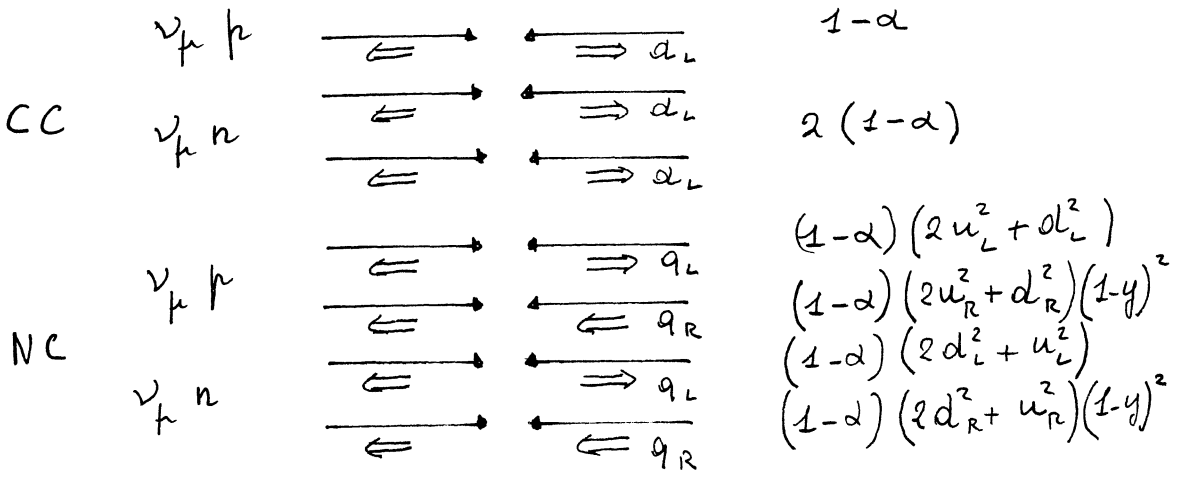

The upper part of this expression represents the elementary subprocesses of the νp scattering, the lower that of the νn scattering. The ratios of NC to CC events induced by neutrino interactions on protons and neutrons are

$$R_p = \frac{\sigma_p^{NC}}{\sigma_p^{CC}} = (2u_L^2 + d_L^2) + (2u_R^2 + d_R^2)(1-y)^2$$

$$R_n = \frac{\sigma_n^{NC}}{\sigma_n^{CC}} = \frac{1}{2} \times \left[(2d_L^2 + u_L^2) + (2d_R^2 + u_R^2)(1-y)^2\right]$$

The values of R_p and R_n are measured in the hydrogen and deuteron bubble-chamber exposures. The recently measured values averaged over different experiments are

$$R_p = 0.49 \pm 0.03 \qquad R_n = 0.26 \pm 0.03$$

All the experimental information collected on isoscalar targets and on hydrogen and deuteron allows the model-independent evaluation of the left- and right-handed NC quark coupling. Table 3 gives the result of this analysis.

The ratio of NC to CC events induced by antineutrino interactions $\bar{R}_p$ has also been measured on hydrogen and gives $\bar{R}_p = 0.36 \pm 0.06$. The combined information on R_p and $\bar{R}_p$ shown in Fig. 17 gives the following value for $\sin^2 \theta$

$$\sin^2 \theta = 0.19 \pm 0.05$$

in good agreement with the world average of $\sin^2 \theta = 0.232 \pm 0.009$.

Table 3

Quark NC coupling

Coupling	Exp. value	Predicted value (SM with $\sin^2 \theta = 0.23$)
u_L^2	0.13 ± 0.03	$\frac{1}{2} - \frac{2}{3} \sin^2 \theta = 0.12$
d_L^2	0.17 ± 0.03	$-\frac{1}{2} + \frac{1}{3} \sin^2 \theta = 0.18$
u_R^2	0.03 ± 0.01	$-\frac{2}{3} \sin^2 \theta = 0.024$
d_R^2	0.00 ± 0.01	$\frac{1}{3} \sin^2 \theta = 0.006$

3.6 Generation universality in the neutral current quark interaction

The data on deep inelastic neutrino-nucleon scattering in the analysis presented in the previous section have been interpreted in terms of the u and the d quark inside the nucleon, the small contribution due to the amount of the strange quark present in the nucleon sea being neglected. An attempt to extract the NC strange quark coupling from the global fit of the y distribution of CC and NC events has recently been carried out by the CHARM Collaboration (Fig. 18). The result of the fit allows the determination of the quark's coupling to the NC

$$\frac{g_s^2}{g_d^2} = \frac{s_L^2 + s_R^2}{d_L^2 + d_R^2} = 1.39 \pm 0.43$$

in agreement with the universality predicted by the SM for quarks of the same charge and different flavour.

The CDHS Collaboration has derived the NC charm quark coupling from the study of the mass distribution of neutrino-induced events with two muons in the final state. In the

analysis the hypothesis is made that the dimuon events with mass around 3 GeV are produced according to the gluon Z^0 fusion mechanism, as shown in Fig. 19. Comparing the neutrino with the muon-induced dimuon events (in the J/ψ mass region) and assuming the gamma gluon fusion mechanism for the muon-induced events, the following NC charm coupling is deduced from the experimental data

$$\frac{g_c^2}{g_u^2} = 2.1 \pm 1$$

This result within large errors is also in agreement with quark weak universality.

3.7 Electroweak effects in e^+e^- annihilations

With the advent of the high-energy e^+e^- rings PETRA and PEP, the electroweak interactions can be investigated in a clean way at high values of the momentum transfer ($Q^2 \simeq 1000$ GeV^2). At the PETRA energy the e^+e^- annihilation into a fermion (f) and an antifermion ($\bar{f}$) is described by the following graphs:

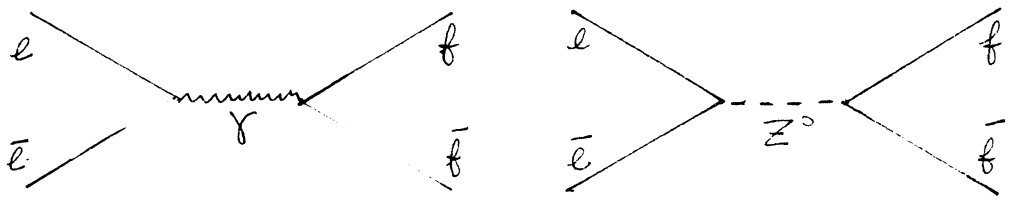

The final fermion angular distribution is determined by the following helicity amplitudes:

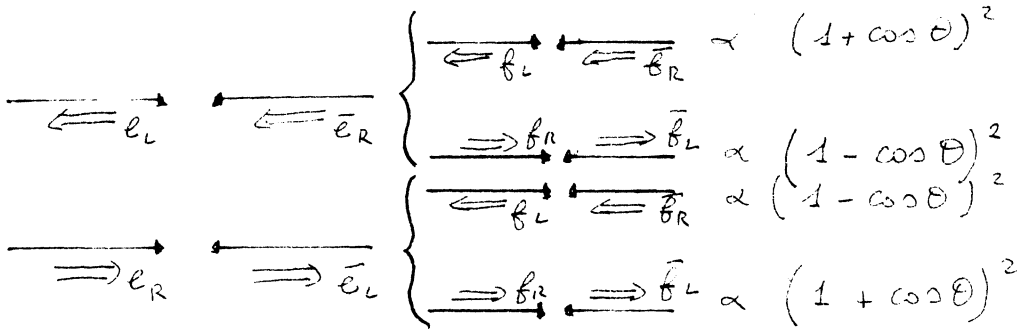

The cross-section is proportional to

$$(1+\cos\theta)^2\left[\left|\frac{ef}{Q^2}+\frac{e_L f_L}{Q^2+M^2}\right|^2+\left|\frac{ef}{Q^2}+\frac{e_R f_R}{Q^2+M^2}\right|^2\right]+(1-\cos\theta)^2\left[\left|\frac{ef}{Q^2}+\frac{e_L f_R}{Q^2+M^2}\right|^2+\left|\frac{ef}{Q^2}+\frac{e_R f_L}{Q^2+M^2}\right|^2\right]$$

where Q^2 is the square of the momentum transfer, f is the electric fermion charge, M is the Z^0 mass, and θ is the angle between the final fermion f and the electron:

The differential cross-section, neglecting the square of the contribution of the Z^0 exchange, is

$$\frac{d\sigma}{d\cos\theta} = \frac{4\alpha^2 f^2}{Q^4}\left[\left(1+\cos^2\theta\right)+\frac{1}{2}\left(1+\cos^2\theta\right)\frac{Q^2}{e_f M^2}\left(e_L+e_R\right)\left(f_L+f_R\right)+\frac{1}{2}\cos\theta\frac{Q^2}{e_f M^2}\left(e_L-e_R\right)\left(f_L-f_R\right)\right]$$

The term proportional to cos θ leads to a backward-forward asymmetry A

$$A = \frac{\sigma(\theta)-\sigma(\pi-\theta)}{\sigma(\theta)+\sigma(\pi-\theta)} \simeq \frac{1}{2}\cos\theta\frac{Q^2}{e_f M^2}\frac{\left(e_L-e_R\right)\left(f_L-f_R\right)}{1+\cos^2\theta}$$

At PEP and PETRA energies Q^2 = 841 and 1200 GeV^2 the expected asymmetries for different $f\bar{f}$ pairs are

$$A_{lepton} = -7.9\%$$
$$A_d = -24\%$$
$$A_u = -12\% \ .$$

The integrated asymmetry depends upon the experimental acceptance so the electroweak couplings are usually derived by the fit to the events angular distribution. The figures show a compilation of the angular distribution of the events for μ and τ pairs obtained by the four PETRA experiments (CELLO, JADE, MARK J, TASSO).

Tables 4 and 5 are a resumé of the μ and τ asymmetry values, as measured up to the summer 1982 at PEP and PETRA.

Table 5

Results from PEP and PETRA on the asymmetry in the reaction $e^+e^- \to \tau^+\tau^-$

Experiment	$\sqrt{s}$ (GeV)	$A_{\tau\tau}$ (%)	Expected in GSW for $\sin^2\theta = 0.23$
MAC	29	-1.3 ± 2.9	-6.3
MARK II	29	-3.2 ± 5.0	-5.0 ($\lvert\cos\theta\rvert < 0.7$)
PEP results combined	29	-1.7 ± 2.5	-6.0
CELLO	34.2	-10.3 ± 5.2	-9.2
JADE (prelim.)	34.2	- 7.9 ± 3.9	-9.2
MARK-J	34.6	- 8.4 ± 4.4	-9.4
TASSO	34.4	- 5.4 ± 4.5	-9.3
PETRA results combined	34.4	-7.9 ± 2.2	-9.3

Table 4

Results from PEP and PETRA on the asymmetry of $e^+e^- \to \mu^+\mu^-$

Experiment	$\sqrt{s}$	Measured $A_{\mu\mu}$ (%)	Expected in GSW for $\sin^2\theta = 0.23$ (%)
MAC	29	-4.4 ± 2.4	-6.3
MARK II	29	-9.6 ± 4.5	-6.3
PEP results combined		-5.6 ± 2.3	-6.3
CELLO	34.2	-6.4 ± 6.4	-9.1
JADE	34.2	-10.8 ± 2.2	-9.2
MARK-J	34.6	-10.4 ± 2.1	-9.4
TASSO	34.4	-10.4 ± 2.3	-9.3
PETRA results combined	34.4	-10.4 ± 1.4	-9.3 for $m_Z = 90$ GeV -7.9 for $m_Z = \infty$

The data on the lepton asymmetry are in good agreement with the SM and give the first indication of the mass of the Z^0 pole, $50 < M_Z < 106$ GeV at the 95% confidence level (Fig. 20).

3.8 Electron-positron annihilation into a quark-antiquark pair

At the present e^+e^- rings' energy, five different quark flavours contribute to the $e\bar{e} \to q\bar{q}$ reaction (q = u, d, s, c, b). The e^+e^- annihilation into hadrons, if the leading hadron flavour can be tagged, gives the possibility of studying the NC heavy-quark coupling.

The backward-forward asymmetry for the charm quark has been investigated with large statistical errors by the TASSO Collaboration. The c quark tagging is done by the reconstruction of the D* mass. The D* formation is the largest fraction of the c fragmentation and the D* identification is helped by the small Q value of the reaction chain

$$D^* \longrightarrow D^0 \pi \longrightarrow K^- \pi^+ \pi$$

The angular distribution of the D* in the e^+e^- annihilation, as measured in the TASSO solenoid, is shown in Fig. 21. From the fit to the experimental points the value of the c quark asymmetry is: $\langle A_c \rangle = -0.35 \pm 0.14$, compared with the predicted value of $A_c = -0.14$. Other information on electroweak effects in $e^+e^- \to$ hadrons has been extracted by the measurement on the total hadron cross-section

$$R = \frac{\sigma^{tot}_{hadron}}{\sigma_{\mu\bar{\mu}}} = 3 \sum_{flavour} \left[Q_f^2 + 2 Q_f (\ell_L + \ell_R)(f_L + f_R) f(\hat{Q}) \right]$$

After the QCD correction to the R value to account for the deviation from the simple QPM expectations [assuming a given value of the QCD scale Λ (where Λ = 0.3 GeV)], the R dependence on s can be interpreted as due to the electroweak effects. The experimental data (shown in Fig. 22) are in agreement with a value of the average vector coupling $(f_L + f_R)$ to the quark corresponding to the universal coupling with $\sin^2 \theta = 0.25$. The experimental data come from the PETRA Collaborations JADE, MARK J, and TASSO.

In conclusion, the weak interactions have been investigated for a large number of physical phenomena ranging from low Q^2 (atomic parity violation and neutrino-electron scattering) to the highest Q^2 available in e^+e^- annihilation. The SM is able to describe all these phenomena with a single universal parameter, the weak angle $\sin^2 \theta$ (Fig. 23).

Alternative models to the SM, such as the popular left-right symmetric model $SU(2)_L \times SU(2)_R \times U(1)$ are, of course, also able to describe (with more parameters) the weak processes, but until now there is no compelling evidence for any departure from the simple SM. The future steps that will more deeply validate (or invalidate) the SM are

i) the discovery of the IVB,

ii) the consistency of the value of the measured IVB mass with the computed value (first and second order), given the low energy input.

The input for these computations are the low Q^2 value of $\sin^2 \theta$ (to be known with a few per cent accuracy) and the mass value of all quarks, including the still missing top quark.

4. EXPERIMENTAL TESTS ON QUANTUM CHROMODYNAMICS

The most acknowledged success of quantum chromodynamics (QCD) is the quark-parton model (QPM). The experimental apparatuses available have, until now, allowed the observation, as a result of particle interactions, of leptons (electron, muons ...) and/or hadrons (pion, kaon, protons, ...), but physicists have accepted the quark hypothesis and have learned to think of the elementary process as due to quark-quark or quark-lepton interactions. The quarks are expected to be bound because the QCD forces confine them to the hadron bag.

This way of thinking is a dramatic change compared to the orthodoxy of the 1960's. The experimental results on the deep inelastic scattering (DIS) of electrons on nucleons were the first indication of the parton constituents of the proton. The interpretation of the SLAC data (Fig. 24) on the DIS by Bjorken was initially done in terms of the current algebra on the light cone, but for such a small space-time volume that the point-like interaction of the nucleon with the virtual photon became mathematically equivalent to the parton-photon interaction (proposed by R. Feynman), illustrated by the following diagram:

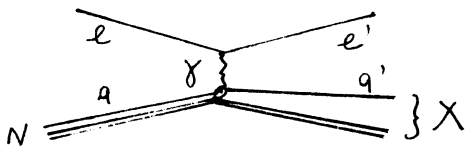

The identification of the parton with the quark (proposed by Gell-Mann and Zweig) was the next step forward in the interpretation of the DIS data. Since the first SLAC experiment (at intermediate electron energy and momentum transfer $E \approx 20$ GeV, $Q^2 \approx 5$ GeV^2), many experimental results on DIS have been obtained using different incident lepton beams (electrons, muons, and neutrinos) covering a wide range of Q^2. The agreement between the experimental results is satisfactory and the collection of DIS data constitutes a solid basis for the validity of the QPM as well as of the QCD that accounts for the small logarithmic departure from the QPM predictions. The QPM can be considered as the zeroth-order approximation of the QCD theory.

4.1 Review of the experimental status of deep inelastic lepton-nucleon scattering

The basic ingredients of the DIS of leptons on nucleons are:

i) the lepton current which is exactly defined by the precisely verified experimental law of the lepton-number conservation;

ii) the point-like nature of the lepton vertex where the spinor field-gauge boson field interaction is known.

The diagram below illustrates schematically the lepton-nucleon scattering and defines the kinematic quantities of the scattering.

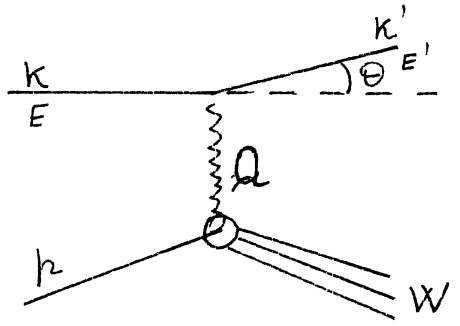

$$Q^2 = 4EE'\sin^2\frac{\theta}{2}$$

$$\nu = E - E'$$

$$x = Q^2/2M\nu$$

The cross-section of the DIS of charged leptons on nucleons is derived as in the book by Aitchison and Hey (p. 80; see Bibliography) and expressed as a function of the variables defined in the above diagram:

$$\frac{d\sigma}{d\Omega\, dE'} = \frac{4\alpha^2 (E')^2}{Q^4}\left[\cos^2\frac{\theta}{2}\, W_2(\nu, Q^2) + 2\sin^2\frac{\theta}{2}\, W_1(\nu, Q^2)\right]$$

If expressed as a function of the dimensionless variables

$$x = Q^2/2M\nu \;\; ; \;\; y = (E - E')/E$$

the cross-section is

$$\frac{d\sigma}{dx\,dy} = \frac{4\pi\alpha M E}{Q^4}\left[y^2 \times F_1(x,Q^2) + \left(1 - y - \frac{Mxy}{2E}\right) F_2(x,Q^2)\right]$$

For neutral incident leptons (neutrinos), the helicity and the V - A nature of the neutrino-gauge boson (W) interaction introduces a new term (a parity-violating one) in the expression of the cross-section, which is

$$\frac{d\sigma^{(\bar{\nu})}}{dx\,dy} = \frac{G^2 M E}{\pi}\left[y^2 \times F_1(x,Q^2) + \left(1 - y - \frac{Mxy}{2E}\right) F_2(x,Q^2) \pm y\left(1 - \frac{y}{2}\right) \times F_3(x,Q^2)\right]$$

The main differences between the charged lepton-nucleon DIS (a) and the neutrino nucleon DIS (b) are:

i) The propagator effect:
   (a) propagator $\propto \frac{1}{Q^2}$
   (b) propagator $\propto \frac{1}{Q^2 + M_W^2} \approx \frac{1}{M_W^2}$

ii) The photon exchange [pure vector (V) interaction]. This is parity-conserving, while the ν-W coupling is V - A and gives the maximum parity violation. The $\pm$ sign in front of the structure F_3 takes into account the change of helicity and consequently of coupling of the neutrino with the W and of the antineutrino with the W.

iii) The structure functions F_i. These have the same analytical dependence upon the variables x and Q^2, but differ by a multiplicative constant for charged or neutral lepton-nucleon DIS. The multiplicative constant is due to the different electric or weak charge of the quarks.

Figures 25a and b illustrate some of the differences in doing experiments on the DIS of leptons on nucleons using muon or neutrino beams. As already mentioned, the DIS experiments are today done with different beams (e, μ, ν) and at the highest Q^2 and energy available at the present accelerators. The DIS study will be extended to very high Q^2 and ν values with the advent of the electron-proton (ep) collider as proposed by the HERA project. As shown in Fig. 26, the realization of the HERA project will allow the experimentation of ep DIS at $Q^2 \approx 10^5$ GeV^2 and $\nu = E - E' \simeq 1.5 \times 10^3$ GeV.

4.2 The quark-parton model and the scaling law of the structure functions (F_i)

The experimental data on ep DIS at intermediate Q^2 values ($2 \leq Q^2 \leq 8$ GeV^2) collected at SLAC are shown in Fig. 27. The data show that for a given $x = 1/\omega$ value the structure function W_2 is independent of Q^2. This behaviour of the W_2 is known as the scaling law.

The interpretation of the scaling of the structure functions was given by Bjorken in 1969 in terms of the QPM and predicts, at large Q^2 values compared to the square of the proton mass,

$$F_i(x,Q^2) \longrightarrow F_i(x)$$

when

$$Q^2 \longrightarrow \infty \quad \Rightarrow x = \frac{Q^2}{2M\nu} = \text{const.}$$
$$\nu \longrightarrow \infty$$

In Aitchison and Hey it is shown how the QPM predicts scaling, and the structure functions F_2 are interpreted as probability distributions $q_i(x)$ of finding the quark q_i carrying a fraction x of the nucleon momentum,

$$2x F_1(x) = F_2(x) = \sum e_i^2 x q_i(x)$$

where e_i is the electric charge of the quark q_i. The relation between F_1 and F_2 is a consequence of the spin of the quark and is known as the Callan-Gross relation.

The electron-proton DIS is described according to the proton (u u d) structure functions

$$F_2^{ep}(x) = \frac{4}{9} x\left[u^p(x) + \bar{u}^p(x)\right] + \frac{1}{9}\left[d^p(x) + \bar{d}^p(x)\right]$$

where 4/9, 1/9 are the square of the elctric charge (2/3, 1/3) of the u and d quarks, and $u^p(x)$ and $d^p(x)$ represent the probability of finding in the proton a quark u or d with a fractional momentum x. For the DIS of electrons on protons p ≡ (u u d) and on neutrons n = (d d u), the isospin invariance relation gives

$$u^p(x) = d^n(x)$$

The structure functions $F_i(x)$ are

$$\frac{1}{x}F_2^{ep} = \frac{4}{9}\left[u(x) + \bar{u}(x)\right] + \frac{1}{9}\left[d(x) + \bar{d}(x)\right]$$

$$\frac{1}{x}F_2^{en} = \frac{1}{9}\left[u(x) + \bar{u}(x)\right] + \frac{4}{9}\left[d(x) + \bar{d}(x)\right]$$

The index p of u^p and d^p has been omitted for simplicity. If the SU(2) isospin invariance is valid for the antiquark sea in the nucleon

$$\bar{d}(x) = \bar{u}(x)$$

the following relation is valid

$$F_2^{ep} - F_2^{en} = \frac{x}{3}\left[u(x) - d(x)\right]$$

The experimental x distribution of $F_2^{ep} - F_2^{en}$ is shown in Fig. 28.

The nucleon structure function deduced from the experimental data of DIS of charged leptons on nucleons and of neutrinos on nucleons can be compared with the value predicted by the QPM.

$$F_2^{\nu N} = 2x\left[u(x)+\bar{u}(x)+d(x)+\bar{d}(x)+O(s)\right]$$

$$F_2^{eN} = \frac{5}{9}x\left[u(x)+\bar{u}(x)+d(x)+\bar{d}(x)+O(s)\right]$$

The term O(S) is a small correction due to the presence of a strange quark s in the nucleon sea.

The relation between $F_2^{\nu N}$ and F_2^{eN} is well verified experimentally, as shown in Fig. 29, where the data of the two CERN muon experiments [being done by the European Muon Collaboration (EMC) and the BCDMS Collaboration] are compared with the results obtianed in the CERN neutrino beams by the CDHS Collaboration. The integral of $F_2(x)$ over all the x values ($0 \leq x \leq 1$) is interpreted in the QPM as the fraction of nucleon momentum (ε) carried by the valence quark that interacts with the virtual exchanged boson (γ,W).

The numerical integration over the data shows that only approximately one half of the nucleon momentum is carried by the quark; the remaining momentum is carried by the gluons that do not interact with the gauge bosons (γ,W). The quark and antiquark x distributions in the nucleon are determined in the DIS of (anti)neutrinos on nucleons:

$$d\sigma^{\nu}+d\sigma^{\bar{\nu}} \propto F_2^{\nu N} = 2x\left[u+d+\bar{u}+\bar{d}\right]$$

$$d\sigma^{\nu}-d\sigma^{\bar{\nu}} \propto xF_3 = 2x\left[u-\bar{u}+d-\bar{d}\right]$$

$$\frac{F_2^{\nu N}+xF_3}{2} = 2x\left[u+d\right] \propto q(x)$$

$$\frac{F_2^{\nu N}-xF_3}{2} = 2x\left[\bar{u}+\bar{d}\right] \propto \bar{q}(x)$$

The antiquark distribution derived by the analysis of the experimental data collected by the CDHS Collaboration is shown in Fig. 30.

The review of the DIS of leptons on nucleons shows that the QPM explains quite well the nucleon structure and that the quarks are indeed responsible for the DIS of the leptons.

4.3 Departure from the scaling behaviour of the structure functions and the QCD interpretation

The experimental data of DIS of leptons on nucleons shown in Fig. 31 for different x bins and as a function of Q^2 indicates a slow dependence on Q^2. The value of F_2 at large x ($x \geq 0.45$) is slightly decreasing at large Q^2 ($Q^2 > 20$ GeV^2).

The amount of scaling violation is quantified by $b = d \ln F_2 / d \ln Q^2$. Figure 31 shows the slope b as measured in three high-energy lepton-nucleon DIS experiments.

The deviation from the scaling behaviour of the structure function is predicted in QCD. The mathematical description of the Q^2 evolution of the structure functions is given by the Altarelli-Parisi equations.

The equations derive the evolution of F_2 as a function of the variable $t = \ln \alpha_s(Q^2)/\alpha_s(Q_0^2)$ from the knowledge of quark and gluon distributions at $t = 0$, where α_s is the coupling "constant" of QCD and is a logarithmic function of Q^2 and of the QCD scale parameter Λ.

Introducing $G(x,0)$, $V(x,0)$, and $S(x,0)$ as the gluon, the valence quark, and the sea quark x-distributions, respectively, at $t = 0$, the structure functions F_i can be expressed as

$$x F_3(xQ^2) = E_v(xt) \odot V(x,0)$$

$$F_2(xQ^2) = E_{FF}(xt) \odot [V(x0) + S(x0)] + E_{FG}(xt) \odot G(x0)$$

$$2\bar{q}(xQ^2) = [E_{FF}(xt) - E_v(xt)] \odot V(x0) + E_{FF}(xt) \odot S(x,0) + E_{FG}(xt) \odot G(x,0)$$

where the symbol $\odot$ stands for the convolution integral and $E_{V,FF,FG}(x,t)$ represent the QCD predicted evolution of non-singlet (valence) quarks into non-singlet quarks, of singlet quarks into singlet quarks, and of singlet quarks into gluons plus quarks, respectively. Their expression is determined by the Altarelli-Parisi equations when the scale parameter Λ is fixed. The initial values of $V(x,0)$, $S(x,0)$, and $G(x,0)$ cannot be computed by the QCD perturbative theory and have to be fixed by the experiment.

An analysis based on high-statistics neutrino-nucleon DIS data collected using the CERN WBB and the CHARM detector have shown the validity of the Altarelli-Parisi method, measured the gluon distribution in the nucleon, and determined the value of the QCD scale parameter Λ in the lowest order of QCD ($\Lambda_{L.O.}$):

$$\Lambda_{LO} = \left(187^{+130}_{-110} \pm 70\right) \text{ Mev}$$

from the analysis of xF_3 and

$$\Lambda_{LO} = \left(190^{+70}_{-40} \pm 70\right) \text{ Mev}$$

from F_2.

The results of the CHARM analysis are shown in Fig. 32, where xF_3, F_2, and $\bar{q}$ are shown plotted against Q^2. The evolution of the gluon distribution function is shown in Figs. 33a and b.

In Landshoff's lectures at this school it has been shown that the determination of Λ from the data is not free of theoretical ambiguities. The experimental situation also poses some problems in spite of the good quality of the experimental data; the evolution of the structure functions with Q^2 is quite slow and the accuracy of the data is still not adequate to correctly determine the logarithmic effect induced by the QCD high-order terms. Table 6 giving the Λ values derived from different DIS lepton-nucleon experiments, reflects the incertitude of the experimental status of Λ measurements.

Table 6

The measurement of Λ in deep inelastic scattering

Experiment	$\Lambda_{L.O.}$ (MeV)	$\Lambda_{\overline{MS}}$ (MeV)
μFe (EMC)	$112 \pm 20 \,^{+\,114}_{-\,70}$	$170 \,^{+\,155}_{-\,105}$
μH_2 (EMC)	$110 \,^{+\,60}_{-\,90} \,^{+\,124}_{-\,70}$	$145 \,^{+\,150}_{-\,90}$
μC (BCDMS)	$85 \,^{+\,60}_{-\,40} \,^{+\,90}_{-\,70}$	
νFe (CDHS) (singlet fit)	$290 \pm 80 \pm 120$	$300 \pm 80 \pm 120$
νFe (CDHS) (F_2 fit)	$180 \pm 30 \pm 100$	
$\nu CaCO_3$ (CHARM) (singlet fit)	$187 \,^{+\,130}_{-\,110} \pm 70$	
$\nu CaCO_3$ (CHARM) (F_2 fit)	$190 \,^{+\,70}_{-\,40} \pm 70$	

Table 6 shows that the experimental situation on the Λ value as derived by the fundamental process of DIS of leptons on nucleons is not completely settled, and the most conservative statement on Λ is that the QCD scale is ≈ 0.1 GeV. Another element of incertitude in the determination of Λ from the DIS data is that most of the data have been collected on bound nuclei. The EMC have recently shown that contrary to expectation even at high ν and Q^2 values the nucleon structure functions feels nuclear effects other than the Fermi motion. Figure 34 shows the ratio $F_2^{\mu\nu}$ as measured on iron and deuterium plotted against x for $\langle Q^2 \rangle \approx 50$ GeV^2.

This brief review of the experimental situation of DIS of leptons on nucleons shows that experimental data are in qualitative agreement with the prediction of QCD but quantitative tests of QCD in DIS phenomena are at the moment not possible because of both theoretical and experimental inaccuracies.

4.4 The e^+e^- annihilation into hadrons

The study of the e^+e^- annihilation into hadrons has provided the most convincing evidence of the role of the quarks in hadron physics. The experimental results on the cross-section measurement for the process

$$e^+e^- \rightarrow \text{hadrons} \ ,$$

collected at different e^+e^- storage rings, are shown in Fig. 35. The cross-section data are presented as a ratio between the cross-section of the process under study and the cross-section for the production of a point-like $\mu^+\mu^-$ particle pair:

$$R = \frac{\sigma(e\bar{e} \to \text{hadrons})}{\sigma(e\bar{e} \to \mu\bar{\mu})}$$

The high values of R at some values of the c.m.s. energy $\sqrt{s}$ in a narrow interval $\Delta\sqrt{s}$ are indicative of the production of the bound state of a quark-antiquark pair. The R peaks are the best demonstration of the existence of the quark generations.

The very narrow width of the $Q_i\bar{Q}_i$ system of the last two discovered quark flavours [charm (c), beauty (b)] is explained by the $Q\bar{Q}$ annihilation into three gluons as predicted by QCD.

The energy conservation does not allow the decay of the $C\bar{C}$ or the $B\bar{B}$ $^3S_1$ state into a pair of charmed or beauty mesons since $M_{J/\psi} < 2M_D$ and $M_T < 2M_B$. The $^3S_1$ $Q\bar{Q}$ system decays into three coloured gluons. The three-gluon decay is the lowest order decay of the $Q\bar{Q}$ system into non-coloured hadrons allowed by spin and colour conservation.

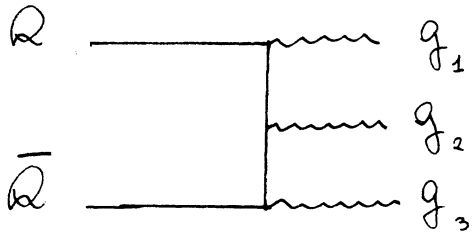

The width of the previous decay is small because the process is proportional to the third power of the QCD coupling constant α_s. The value of R in the energy interval between two flavour thresholds is constant (after the resonance wiggling) and is

$$R = 3\sum_f e_f^2$$

where e_f is the electric charge of the quarks q_f that can be produced at the value of the c.m.s. energy $\sqrt{s}$. The value of R is in agreement with the hypothesis of coloured quarks with fractional electronic charge. At the high energy of the e^+e^- system available at the PETRA and PEP storage rings the e^+e^- annihilation into hadrons appears most of the time as a system of two hadron jets at $\sim 180°$ as illustrated in Fig. 36, which displays an event recorded on the detector of the JADE Collaboration. The two jets are interpreted as the result of the fragmentation of the $q\bar{q}$ pairs produced by the virtual photon

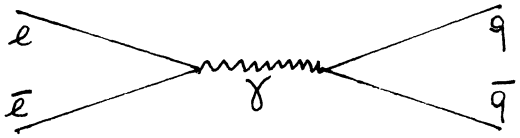

The angular distribution of the jet relative to the beam has been measured and is proportional to $1 + \cos^2\theta$, as expected for spin 1/2 particles. The e^+e^- storage rings experiments have in this way determined the existence of the different quark flavours and measured the spin and the electric charge of the quarks. The study of the e^+e^- annihilation into hadrons is strong support for the validity of the QPM.

4.5 The QCD predictions for the e^+e^- physics

The e^+e^- storage rings have a unique feature in that the energy of the virtual annihilation photon can be accurately tuned to the energy of the bound system of the quark-antiquark pair. The e^+e^- storage rings are the most effective factories for the $Q\bar{Q}$ bound states called "Onia". The study of the physical properties of the Onia states allows the investigation of the quark-quark potential in the quark bound state. The quark-quark potential V can, in principle, be derived by QCD; in practice it is approximated by two terms, one reflecting the asymptotic QCD behaviour and the other describing phenomenologically the confinement forces.

$$V(r) = \frac{-4\alpha_s(r)}{3\,r} + a\,r + V_0$$

The previous potential and the quark spin and angular momentum predict the level splitting of the $Q\bar{Q}$ state as shown in Fig. 37.

The lower energy level is the state $^3S_1$. As previously seen, the $^3S_1$ state can only decay into hadrons through the three-gluon annihilation. The width of this decay is

$$\Gamma\left(^3S_1 \rightarrow g_1 g_2 g_3 \rightarrow \text{hadrons}\right) = \frac{160}{81}\left(\pi^2 - 9\right)\alpha_s^2 \frac{\left|^3S_1(0)\right|^2}{M^2}$$

Here $^3S_1(0)$ is the quark wave function at the origin and M is the mass of the Onium state. The width of the $^3S_1$ state decay into lepton pairs is

$$\Gamma\left(^3S_1 \rightarrow e^+e^-\right) = \frac{64\pi\alpha^2}{9}\,\frac{\left|^3S_1(0)\right|^2}{M^2}$$

The ratio of the widths is a measurement of the strength of the QCD coupling constant.

The experimental data on the J/ψ decay into hadrons and electron-positron pairs give the following values for J/ψ:

Mass (MeV)	Γ (MeV)	Γ_{ee} (MeV)	α_s
3.095	0.069	4.8×10^{-3}	0.19

A similar analysis to that carried out for the $B\bar{B}$ bound state $^3S_1$ was done by the CLEO Collaboration at the Cornell e^+e^- storage ring CESR and gives

$$\frac{\Gamma_{\mu\bar{\mu}}}{\Gamma} = 0.036 \pm 0.009$$

$$\alpha_s\left(0.48\,M_\gamma\right) = 0.152 \pm 0.02$$

$$\Lambda_{\overline{MS}} = 83\,^{+\,58}_{-\,33}\ \text{Mev}$$

The next Onium state expected to be discovered (the $T\bar{T}$ bound state) will have a mass larger than 38 GeV (from the negative search at PETRA up to this energy).

The study of such a high mass Onium state is expected to allow an important check on QCD predictions, such as the study of the existence of the three-gluon vertex, predicted by the non-Abelian nature of the symmetry of the colour forces $SU(3)_c$.

The existence of the three-gluon coupling can be proved if in the study of the four-jet annihilation of toponium the two contributions shown in the diagram below can be quantitatively separated

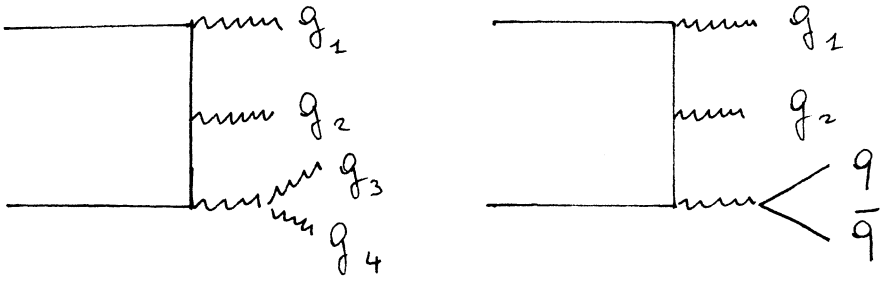

4.6 The e^+e^- annihilation into three hadron jets and the QCD predictions

A small fraction of the events of e^+e^- annihilation into hadrons at PETRA energy shows a topology of three jets of hadrons. The separation of the three-jet events from the larger category of the two-jet events is somehow model-dependent since fluctuation of the two-quark fragmentation into hadrons can simulate a three-jet configuration. This incertitude is evaluated using different hadronization schemes; the systematic error in the final result is evaluated from the discrepancy of the results derived using different fragmentation models.

Once the three-jet configuration and the jet energy is defined according to a given algorithm the experimental distribution of the events as a function of the fractional jet energies,

$$x_i = \frac{E_i}{2 E_{beam}}$$

can be compared with the theoretical predictions for the reaction $e\bar{e} \rightarrow q\bar{q}g$

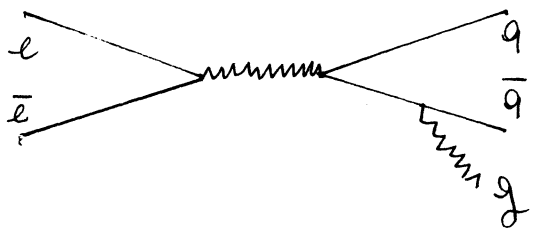

which is the candidate process to produce events with three hadron jets. The cross-section for the reaction $e^+e^- \rightarrow q\bar{q}g$ is

$$\frac{1}{\sigma_0}\frac{d\sigma}{dx_1 dx_2} = \frac{2\alpha_s}{3\pi}\left[\frac{x_1^2 + x_2^2}{(1-x_1)(1-x_2)} + \begin{matrix}1\to 2\\ 2\to 3\\ \cdots\end{matrix}\right] \text{ vector gluons}$$

$$\frac{\alpha_s}{3\pi}\left[\frac{x_3^2}{(1-x_1)(1-x_2)} + \begin{matrix}1\to 2\\ 2\to 3\end{matrix}\right] \text{ scalar gluons}$$

The analysis of the three-jet events made by the TASSO Collaboration at PETRA gives strong support to the vector-gluon hypothesis and derives a first-order value for α_s

$$\alpha_{3\,jets}^{(1)} = 0.17 \pm 0.02 \pm 0.03$$

The JADE Collaboration at PETRA has done a similar analysis considering first- and second-order QCD predictions. The results from the JADE Collaboration analysis are

$$\alpha_{3\,jets}^{(1)} = 0.20 \pm 0.01 \pm 0.01 \quad \text{1st order}$$

$$\alpha_{3\,jets} = 0.16 \pm 0.01 \pm 0.01 \quad \text{1st + 2nd order}$$

The value of α_s has been measured in many other methods related to e^+e^- physics. Table 7 gives a review of the results on α_s using different e^+e^- reactions.

Table 7

Experiment	Method	Fragmentation model	α_s
JADE	R = 3.93 ± 0.03 ± 0.09	-	0.14 ± 0.08 ($\sin^2\theta$ = 0.23)
MARK J	R = 3.84 ± 0.05 ± 0.22	-	$0 < \alpha_s < 0.22$ ($\sin^2\theta$ = 0.23)
TASSO	R = 4.01 ± 0.03 ± 0.20	-	0.24 ± 0.05 ± 0.13 ($\sin^2\theta$ = 0.23)
CELLO	3 jets	FF string	0.15 - 0.20 0.235 - 0.28
JADE	3 jets	FF string	0.20 ± 0.015 ± 0.03
MARK J	3 jets	FF	0.17 ± 0.003 ± 0.02
PLUTO	3 jets	FF	0.15 ± 0.02 ± 0.03
TASSO	3 jets	FF	0.19 ± 0.02 ± 0.03
Second-order QCD JADE	3 jets	FF string	0.16 ± 0.01 ± 0.03
TASSO	3 jets	FF	0.165 ± 0.015 ± 0.03

FF = Field-Feynman

String = Lund model

The agreement between the different experimental results on α_s is satisfactory, allowing for the large experimental incertitude. Nevertheless, the dispersion of the values of α_s clearly shows that this measurement is process-dependent and that the derivation of α_s from the data is model-dependent.

The incertitude in the measurement of a fundamental quantity such as the strength of the coupling constant α_s shows that in this fascinating domain of coloured forces between the quarks much more experimental and theoretical work is necessary to reach a quantitative level of comparison between theory and nature. The quality of the experimental data is expected to improve owing to the higher statistics that will be available in the future from the present PETRA and PEP experiments. The future Z^0 factories, LEP and the Stanford Linear Collider (SLC), will provide a very large number of $q\bar{q}$ and $q\bar{q}g$ events at high energy ($\sim$ 100 GeV). The advent of these new data will stimulate the already fast progress in developing the theoretical techniques for solving the difficult problems posed by QCD.

4.7 The deep inelastic hadron interactions

The hadron-hadron interactions in the QPM are described by the elementary scattering of one of the target partons on a beam parton:

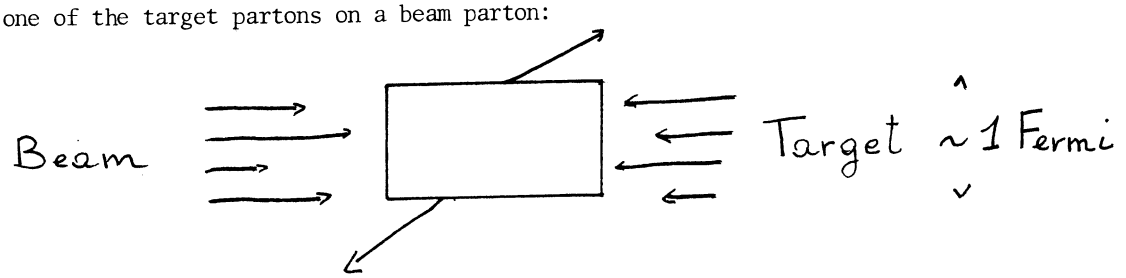

The hadron beam is a superposition of heterogeneous and coloured beams of constituents. The parton momenta are not monochromatic but have a distribution described by the hadron structure functions.

The elementary parton-parton scattering is kinematically defined by the partons' four-momentum:

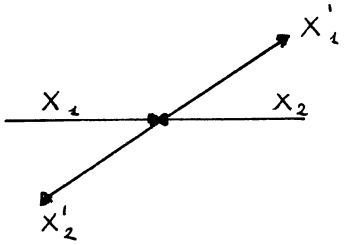

The square of the centre-of-mass energy of the parton-parton system is

$$\hat{s} = x_1 x_2 s$$

where $s = (p_1 + p_2)^2$ is the square of the total hadron-hadron energy.

The luminosity of the parton-parton system is related to the probability of finding the parton q with a fractional momentum x in the hadron.

The proton-(anti)proton collisions are described in terms of different parton-parton luminosity

$$\frac{d\mathcal{L}_{u\bar{u}}}{d\tau}, \quad \frac{d\mathcal{L}_{u\bar{d}}}{d\tau}, \quad \frac{d\mathcal{L}_{d\bar{d}}}{d\tau}, \quad \frac{d\mathcal{L}_{gg}}{d\tau}$$

where $\tau \equiv x_1 x_2$ is the fraction of the total c.m.s. energy squared carried by the parton-parton system.

For the $p\bar{p}$ collider the $u\bar{d}$ luminosity

$$\frac{d\mathcal{L}_{u\bar{d}}}{d\tau} = \int dx_1 dx_2 \, \delta(\tau - x_1 x_2) \left[f_{1u}(x_1) f_{2\bar{d}}(x_2) + f_{1\bar{d}}(x_1) f_{2u}(x_2) \right]$$

$f_{i,u}$ and $f_{i,\bar{d}}$ are the probability of finding in the proton or in the antiproton a $u(\bar{d})$ quark with fractional momentum x_i. The f_i can be deduced from the proton (antiproton) structure function. The parton-parton luminosities are shown in Fig. 38.

The effective cross-section for $p\bar{p} \to x$ is computed by integrating over τ the product of the effective luminosity $d\mathcal{L}/d\tau$ times the cross-section of the parton-parton interaction:

$$d\sigma_{eff} = \int d\tau \, \frac{d\mathcal{L}}{d\tau} \, d\sigma(\hat{s} = \tau s)$$

An important example of $d\sigma_{eff}$ is the annihilation of a $q\bar{q}$ pair into a lepton-antilepton pair [Drell-Yan (DY) process], illustrated by the diagram below:

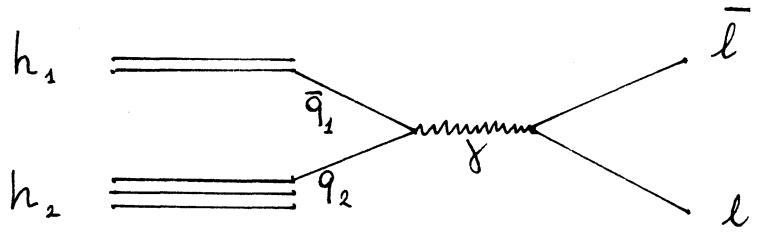

The cross-section for a $q\bar{q}$ annihilation into a lepton pair is

$$\frac{d\sigma}{dx_1 dx_2} = \frac{4\pi\alpha^2}{3s\tau} \left(\frac{1}{3}\right)_{Col} \left[\frac{4}{9} \frac{d\mathcal{L}_{u\bar{u}}}{dt} + \frac{1}{9} \frac{d\mathcal{L}_{d\bar{d}}}{d\tau} \right] \quad (6)$$

The DY $q\bar{q}$ annihilation has been experimentally investigated using different beams and targets as shown in Table 8. An ideal experimental situation for the investigation of the DY process is given by the $p\bar{p}$ collider.

As an exercise let us compute the expected cross-section for lepton-pair production at the CERN SPS collider for leptons with mass larger than 15 GeV. From the differential cross-section given in formula (6) and the luminosity of $u\bar{u}$ and $d\bar{d}$ shown in Fig. 39 one gets

$$s \frac{d\sigma}{d\tau} = \frac{4\pi\alpha^2}{9\tau} \frac{17}{36} 2 \frac{e^{-10\sqrt{\tau}}}{\tau}$$

$$\sigma(\tau > \tau_0) = \frac{34\pi\alpha^2}{81 s} \int_{\tau_0}^{\infty} \frac{d\tau}{\tau^2} e^{-10\sqrt{\tau}} \; ; \; \sigma(M \geq 15\,GeV) \approx 7 \times 10^{-35}\,cm^2$$

Table 8

Incident particle	Energy (GeV)	Accelerator	Accelerator
p	200-400	Fermilab	Two-arm spectrometer
p	400	Fermilab	Iron toroids
p	$\sqrt{s}$ = 62	ISR	Iron toroids
p	$\sqrt{s}$ = 30, 53, 62	ISR	Liquid argon cal.
$\pi^{\pm}(K^{\pm}p\bar{p})$	40 GeV	SPS	Ω spectrometer
$\pi^{\pm}K^{\pm}$	150 GeV	SPS	Dump + spectrometer
$\pi^{\pm}K^{\pm}p\bar{p}$	200 GeV		
π^{-}	280 GeV		
$\pi^{\pm}$	225 GeV	Fermilab	Dump + spectrometer

Using the same method it is possible to compute the rate predicted at the CERN SPS collider for the process

$$p\bar{p} \longrightarrow Z^{0}X \longrightarrow e\bar{e}$$

$$\sigma_{eff} = \frac{4\pi^2}{M_{Z^0}^2}(2J+1)\frac{B_{eff}\Gamma}{M_{Z^0}}\left(\tau\frac{dL}{d\tau}\right)_{\tau=\frac{M_{Z^0}^2}{S}} B_{Z^0\to e\bar{e}} \qquad (7)$$

where

$B_{eff} = B(Z \to u^c\bar{u}^c) + B(Z \to d^c\bar{d}^c) = 0.015$

$B(Z_0 \to e\bar{e}) = 0.03$

$J = Z_0$ angular momentum

$\Gamma = Z_0$ total width

$M = Z_0$ mass

Substituting in Eq. (7) the numerical values one get

$$\sigma_{eff} = 3 \times 10^{-35}\ cm^2$$

If the luminosity of the $p\bar{p}$ collider is

$$\mathcal{L} = 5 \times 10^{28}\ cm^{-2}\ sec^{-1}$$

for a full efficiency detector the rate of events for a Z^0 decay into an electron pair is 1 event approximately every 10^6 s.

The experimental results on the DY process have been compared with the first-order QCD predictions. The agreement between experimental results and the predictions is quite good, but the first-order correction to the QPM results are large and this casts some doubts on the validity of the perturbation expansion.

4.8 Large transverse momentum hadron-hadron scattering

The deep inelastic hadron interactions are an important field of investigation for the hard parton-parton scattering. In the parton model of the hadron the large transverse momentum (large p_T) of the hadron-hadron scattering is the result of the large-p_T parton-parton elastic scattering illustrated in the diagram below:

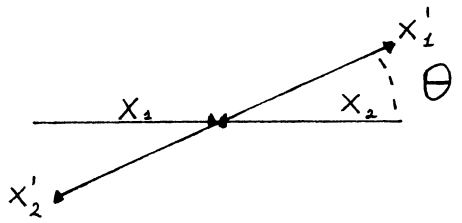

$$p_\perp = \frac{\sqrt{\tau s}}{2} \sin\theta$$

$$\sin\theta = \frac{2p_\perp}{\sqrt{\tau s}} = \frac{x_T}{\sqrt{\tau}}$$

If the charge of the scattered parton is not detected the cross-section is symmetric around 90° and

$$\theta \equiv \pi - \theta \,, \qquad 0 \le \theta \le \frac{\pi}{2}$$

The cross-section for the inclusive jet yield is

$$\frac{d\sigma^{eff}}{dp_\perp^2} = \int d\tau \frac{d\mathcal{L}}{d\tau} \frac{d\sigma}{dp_\perp^2}$$

The large-p_T jet can be produced by the scattering of different partons. The contributions to the inclusive jet yield due to every channel have been computed and the results are shown in Table 9.

Table 9*

The contributions of the different QCD subprocesses

	Subprocesses	$\lvert A\rvert^2$
1	$q_i q_j \to q_i q_j$, $q_i \bar{q}_j \to q_i \bar{q}_j$ $(i \neq j)$	$\frac{4}{9}(\hat{s}^2 + \hat{u}^2)/\hat{t}^2$
2	$q_i q_i \to q_i q_i$	$\frac{4}{9}\left(\frac{\hat{s}^2 + \hat{u}^2}{\hat{t}^2} + \frac{\hat{s}^2 + \hat{t}^2}{\hat{u}^2}\right) - \frac{8}{27}\frac{\hat{s}^2}{\hat{u}\hat{t}}$
3	$q_i \bar{q}_i \to q_i \bar{q}_i$	$\frac{4}{9}\left(\frac{\hat{s}^2 + \hat{u}^2}{\hat{t}^2} + \frac{\hat{t}^2 + \hat{u}^2}{\hat{s}^2}\right) - \frac{8}{27}\frac{\hat{u}^2}{\hat{s}\hat{t}}$
4	$q_i \bar{q}_i \to gg$	$\frac{32}{27}\left(\frac{\hat{u}^2 + \hat{t}^2}{\hat{u}\hat{t}}\right) - \frac{8}{3}\left(\frac{\hat{u}^2 + \hat{t}^2}{\hat{s}^2}\right)$
5	$gg \to q_i \bar{q}_i$	$\frac{1}{6}\left(\frac{\hat{u}^2 + \hat{t}^2}{\hat{u}\hat{t}}\right) - \frac{3}{8}\left(\frac{\hat{u}^2 + \hat{t}^2}{\hat{s}^2}\right)$
6	$q_i g \to q_i g$	$-\frac{4}{9}\left(\frac{\hat{u}^2 + \hat{s}^2}{\hat{u}\hat{s}}\right) + \left(\frac{\hat{u}^2 + \hat{s}^2}{\hat{t}^2}\right)$
7	$gg \to gg$	$\frac{9}{2}\left(3 - \frac{\hat{u}\hat{t}}{\hat{s}^2} - \frac{\hat{u}\hat{s}}{\hat{t}^2} - \frac{\hat{s}\hat{t}}{\hat{u}^2}\right)$

* Taken from R. Horgan and M. Jacob, Nucl. Phys. B179, 441 (1981).

The kinematical variables of the subprocesses are:

$$\hat{s} = \frac{1}{2} x_T s \left(x_1 \operatorname{tg} \frac{\Theta}{2} + x_2 \operatorname{cot} \frac{\Theta}{2} \right) = x_1 x_2 s$$

$$\hat{t} = \frac{1}{2} x_T s x_1 \operatorname{tg} \frac{\Theta}{2}$$

$$\hat{u} = \frac{1}{2} x_T s x_2 \operatorname{cotg} \frac{\Theta}{2}$$

From the luminosity values of the different parton-parton systems (Fig. 38) and from the cross-sections of the subprocess scattering it is possible to compute the relative yield of the $u\bar{u}$ scattering to the gg scattering for a given x_T at the SPS $p\bar{p}$ collider energy (E = 540 GeV):

$$\frac{\left(\frac{d\sigma}{d\hat{p}_T^2}\right)_{u\bar{u}}}{\left(\frac{d\sigma}{d\hat{p}_1^2}\right)_{gg}} = \frac{2}{10} \frac{140}{27} \frac{8}{243} \sqrt{\frac{30}{10}} e^{20x_T} = 0.015 e^{20x_T}$$

Thus for $x_T < 0.21$ the gg scattering has a larger yield than the $u\bar{u}$ one.

4.8.1 Experimental results on the inclusive jet yield

The successful operation of the CERN $p\bar{p}$ collider is the ideal tool for the study of high transverse momentum (p_T) hadrons jets. At $\sqrt{s}$ = 540 GeV the yield of jets with transverse energy $E_T > 20$ GeV is expected to increase by about four orders of magnitude with respect to the top ISR energy. The recent data collected by the UA1 and UA2 Collaborations can be compared with the expectation computed using the QCD approach.

4.8.2 Results from the UA1 Collaboration

The UA1 detector is a large-solid-angle apparatus with charged particle tracking and electromagnetic-hadronic shower separation capability. The tracking region is a cylindrical drift chamber with tridimensional (x,y,z) read-out of the track coordinates. The drift chamber has powerful pattern recognition as demonstrated by Fig. 40a, which shows the reconstruction of a high particle multiplicity event. The central chamber is surrounded by barrel and end-cap (bouchon) electromagnetic calorimeters of 26 and 27 radiation lengths of lead-scintillator sandwich. The tracking region and the electromagnetic calorimeters are inside a dipole magnetic field of 0.7 T.

The outer hadron calorimetry is realized by the laminated return yoke of the magnet instrumented with scintillating material. The penetrating muons are detected after the hadron calorimeter filter by long drift chambers. A schematic view of the UA1 apparatus is shown in Fig. 41. The distribution of the events in the interval of pseudorapidity $|\eta| < 1.5$, given as a function of the transverse energy E_T, is shown in Fig. 42a. The detailed analysis of the large-E_T events shows clear evidence for jet production indicated by the energy clusters and their space correlation, as shown in Fig. 43.

4.8.3 Results from the UA2 Collaboration

The apparatus used by the UA2 collaboration is shown schematically in Fig. 44. Its central part is a track detector composed of a set of cylindrical proportional and drift chambers in a region without magnetic field. The track detector is surrounded by a highly segmented electromagnetic and hadronic calorimeter, which covers an interval of pseudo-rapidity $-1 \leq \eta \leq 1$. Each calorimetric cell covers an angular interval of $\Delta\theta = \Delta\phi = 10°$. This angular granularity allows the on-line formation of a trigger for jet-like events with large transverse energy E_T.

The data recently published correspond to an integrated luminosity of 79 μb^{-1}. The majority of the events with large E_T are of a jet-like nature; Fig. 45 shows the energy cluster of an event with E_T = 120 GeV.

The E_T distribution for the inclusive jet events is shown in Fig. 46. The experimental data are compared with the QCD calculation of Horgan and Jacob indicated in the figure by the solid line.

The results from both the UA1 and UA2 Collaborations on the inclusive jet transverse energy distribution show that events with $E_T > 60$ GeV around 90° with respect to the beam have a dominant jet structure at $\sqrt{s}$ = 540 GeV. This is an important new result in hadron physics from the $p\bar{p}$ collider in contrast with the previous data from the ISR and fixed-target physics at $\sqrt{s}$ = 24 GeV. The inclusive jet cross-section is easily extracted from the background owing to the tail of the soft scattering physics and the preliminary experimental results agree with the QCD predictions that had foreseen a large increase of the jet cross-section at a large E_T value.

The $p\bar{p}$ collider at high energy has shown clear evidence of the parton-parton nature of the hard hadron-hadron interaction. The contribution of the collider experiments to hadron physics and comparison with QCD predictions is expected to make important progress during the coming high-luminosity runs.

5. EXPERIMENTAL CONSEQUENCES OF GRAND UNIFIED THEORIES

5.1 Introduction

The success of gauge theories in describing the known interactions among the fundamental particles (leptons and quarks) and the doublet structure in the weak interaction of the lepton and quark families, encourages the search for a more profound connection among leptons and quarks and an attempt to find a large gauge symmetry that encompasses all the known spinor fields. In the lectures of Peccei we have also learned that the coupling constants g_1, g_2, and g_3 of the known interactions defined by the local gauge invariance for $SU(3)_C$, $SU(2)_L$ and U(1) evolve with energy and reach a common value at very high energy ($\sim 10^{14}$ GeV). When we want to observe an electron at energy larger than the mass of the charged weak gauge boson ($E > M_W$) it may have emitted a W and we may find that the electron state is spending part of its time as a neutrino electron.

Assuming that the convergence of the coupling constants g_1, g_2, and g_3 to a single value g, for energy around 10^{14} GeV, indicates a fundamental property of nature, we can put forward the hypothesis that a lepton becomes a quark by the emission of a boson of mass $\sim 10^{14}$ GeV. The new gauge boson carries flavour and colour and has fractional electric

charge; in view of the present separation of the interactions it looks quite exotic, but is not in contradiction with any of the present basic principles from which we derive the gauge interactions.

The composition of matter at the energies that have been explored with the accelerating machines is explained by three families of 15 components. The 15 members of the basic (the lightest) family are:

$$\underbrace{\begin{pmatrix} u \\ d \end{pmatrix}_L \quad \begin{matrix} u_R \\ \downarrow \\ \bar{u}_L \end{matrix} \quad \begin{matrix} d_R \\ \downarrow \\ \bar{d}_L \end{matrix}}_{\times\ 3 \text{ for colour}} ; \quad \begin{pmatrix} \nu_e \\ e^- \end{pmatrix}_L \quad \begin{matrix} e_R^- \\ \downarrow \\ e_L^+ \end{matrix}$$

The left-handed up and down quarks form a colour triplet and weak doublet $(u,d)_L \equiv (3,2)$; the left-handed electron and neutrino form a colour singlet and a weak doublet $(\nu,e)_L \equiv (1,2)$. Since the gauge theories conserve the helicity it is more appropriate to form a lepton-quark family with the weak singlets $\bar{u}_L$, $\bar{d}_L$, and e_L^+ and the basic family can be classified in terms of the symmetry of the colour and of the electroweak interactions as

$$(u,d)_L \equiv (3,2) \; ; \; \bar{u}_L \equiv (\bar{3},1) \; ; \; \bar{d}_L \equiv (\bar{3},1) \; ; \; (\nu_e, e)_L \equiv (1,2)$$
$$e^+_L \equiv (1,1)$$

Simple arguments of group theory show that the group that can most easily be decomposed in $SU(3)_C \times SU(2)_L \times U(1)$ is SU(5), a group of rank 4 containing SU(3). The number of gauge bosons associated with a local gauge invariance for an SU(5) transformation is $24 \equiv (5 \times 5 - 1)$. At the present energy the known interactions $SU(3)_C$, $SU(2)_L$, and U(1) are mediated by twelve gauge bosons, the eight coloured gluons, and the four gauge bosons of the electroweak interactions. The physical effects of the twelve new gauge bosons introduced by the local gauge invariance with an SU(5) symmetry are extremely weak at low energy. The coupling strength of the new bosons to the spinor fields in an effective Lagrangian theory, is similar to the Fermi coupling constant ($G_F/\sqrt{2} = g^2/8M_W^2$), but is weaker since the denominator of the new effective coupling constant $G_{GU}/\sqrt{2} = g^2/8M_{GU}^2$ is given the mass of the heavy gauge bosons $M_{GU} \approx 10^{14}$ GeV. The decays or the interactions due to G_{GU} are much weaker than any other process among fundamental particles, and the only observable consequence of the GUT are very rare phenomena such as the proton decay.

5.2 Identity of the absolute value of the proton and electron electric charge

A remarkable experimental result shows that the absolute value of the electron charge is equal within a few parts in 10^{-20} to the proton electric charge, which is assumed to be the sum of the u, u, and d quark electric charges. A local gauge symmetry between leptons and quarks is a natural explanation for the extremely precise identity of proton and electron charge. In the SU(5) invariance this identity can be derived in the following way: the 15 members of the basic family are naturally assigned to be the $\bar{5}$ and the 10 representations. The $\bar{5}$ representation contains the following members of the basic family.

$$\bar{5} \equiv \begin{pmatrix} \bar{d}_R \\ \bar{d}_G \\ \bar{d}_B \\ e^- \\ \nu_e \end{pmatrix}_L$$

The sum of the conserved quantum number of the members of a representation must be zero. This implies

$$Q_{\bar{d}_R} + Q_{\bar{d}_G} + Q_{\bar{d}_B} - 1 + 0 = 0$$

$$Q_{\bar{d}} = 1/3$$

where the electric charges Q are expressed in units of the electron charge.

From the CC weak-interaction reaction between leptons and quarks $\nu_e d \to e^- u$ we know that $Q_u = Q_d + 1$, so the proton charge

$$Q_p = 2Q_u + Q_d = 1$$

is equal to the electron charge.

5.3 Grand Unified Theory and baryon number non-conservation

The stability of the proton (p) against the possible esoenergetic decays such as $p \to e^+\gamma$ has, in the past, been explained by introducing the baryon and lepton conservation law. This law arbitrarily assigns two quantum numbers: one to the proton (baryon number), the other to the electron (electron-lepton number); this mechanism forbids the reaction $p \to e^+\gamma$ since the right and the left terms of the reaction have different baryon and lepton number. In the scheme of gauge theory, to an exactly conserved quantity must correspond a massless gauge boson. Since the only known massless gauge boson for long-range interactions is the photon it is quite natural to consider only the electric charge as a rigorously conserved quantity and to interpret the baryon and lepton number conservation as a result of a strongly inhibited interaction that proceeds very slowly owing to an effective coupling of the type previously described: $G_{GU}/\sqrt{2} = g/8M^2_{GU}$. In particular, the SU(5) symmetry between the quark and the lepton predicts a quite precise result on the proton lifetime.

The diagrams that induce the transition $p \to e^+u\bar{u}$ or $p \to e^+d\bar{d}$ mediated by the heavy gauge bosons of SU(5) are shown in Fig. 47. To compute the proton lifetime from the graphs in this figure the masses of the heavy gauge bosons are needed, the mass values are computed from the coupling-constant evolution function, and the numerical value is a function of the measured constants of the strong and weak interactions. Considering the present incertitude on $\Lambda_{\overline{MS}}$ and on the number of Higgs particles in the SU(5) theory the predicted proton lifetime is $\tau_p = 3.2 \times 10^{29^{+2}_{-2}:^1_5}$ years. The final hadronization of the $u\bar{u}$ or $d\bar{d}$ system from the proton decay can be computed according to different models. Table 10 gives the expected branching ratio for different channels of the proton decay, computed in 6 different ways labelled (a) to (f). The channel $e^+\pi^0$, where all the proton-decay energy is transformed into electromagnetic radiation, is for most of the models the dominant channel.

Table 10

Predictions for branching ratios for proton decay into the major two-body modes in the SU(5) model. (a) - (f) correspond to different theoretical assumptions concerning the hadronic matrix elements, phase space, quark spins, etc.

Mode	(a)	(b)	(c)	(d)	(e)	(f)		
	REC	NR	R	R	R	NR	REC	R
$e^+\pi^0$	31	37	9	13	31	36	40	38
$e^+\rho^0$	15	2	21	20	21	2	7	11
$e^+\eta$	11	7	3	0.1	5	7	1.5	0
$e^+\omega$	18	18	56	46	19	21	25	26
$\nu_e^c\pi^+$	12	15	3	5	11	14	16	15
$\nu_e^c\rho^+$	6	1	8	7	8	1.0	2.6	4
μ^+K^0	1	19	--	7	0.5	18	8	5
$\nu_\mu^cK^+$	2	0	--	0.5	--	0	0.2	0.6

5.4 Proton-decay experiments

As an introduction to the description of the vigorous experimental effort invested in the most spectacular prediction of the unified gauge theory -- the proton decay -- it is useful to give some general arguments that define the experimental difficulties of the proton-lifetime detectors. The proton-decay signature is the release of an energy corresponding to the proton mass ($\sim$ 1 GeV) taking place somewhere in the matter and with a topology corresponding to an energy flow (for the π^0e^+ channel and the free proton) of two back-to-back components, each one carrying $\sim$ 0.5 GeV of energy. Protons bound in the nuclei can decay in two energy flows that deviate from back-to-back topology by as much as 25°.

The main qualities of the proton-decay detector are: large sensitive volume, to push the lifetime to a value that can definitively check the SU(5) prediction ($\tau = 10^{29^{+2}_{-2}:1^{}_{5}}$ years), and good signal-to-noise rejection. The ultimate noise is coming from the cosmic neutrino interactions in the sensitive volume of the detector; the signal-to-noise ratio is enhanced by a good energy resolution and by geometrical or timing information on the topology of the event.

The operating proton decay detectors can be classified according to two main categories:

i) fine-grained wire calorimeters,

ii) water calorimeters based on the detection of the Čerenkov light emitted by the fast particles produced by the two energy flows emerging from the proton decay.

The most well-known proton-decay detectors operating or near to operation are listed in Table 11.

Table 11

Present proton-decay experiments

Experiment	Collaboration	Fiducial volume (t)	Energy resolution (%)	Topological information	Cosmic μ shielding (m.w.e.)*)	Status
Homestake	Pennsylvania-Brookhaven	150	-	-	4500	Operating
Soudan I	Minnesota-Argonne	35		coarse	1700	Operating
Kolar Gold Fields	Tate Institute-Osaka-Tokyo	140	~ 40	coarse	7600	Operating
Nusex (Mt. Blanc)	Frascati-Milan-Turin-CERN	150	~ 20	fine	5000	Operating
IMB	Irvine-Michigan-Brookhaven	9000 (4000 fid. vol.)	~ 10	$\Delta\theta \sim 12°$ for shower	1700	Operating
Harvard-Purdue-Wisconsin	Harvard-Purdue-Wisconsin	800	~ 10	-	1700	Close to operation
Kamioko Japan	KEK-Tokyo-Tsukuba	3400 (1000 fid. vol.)	< 10	$\Delta\theta \leq 10°$ for shower	2700	Close to operation

*) Metre water equivalent.

The future proton-decay experiments, which are all based on fine-grained calorimetry techniques, are the following: Fréjus tunnel, Soudan II, Homestake upgrade, Pennsylvania and Gran Sasso. The Fréjus experiment is the only one in an advanced state of construction and installation is foreseen to begin in autumn 1983.

Among the operating proton-decay detectors two of them have reported candidates coming from proton decay. The Kolar Gold Fields detector is composed of 140 t of iron plates, approximately 1.2 cm thick, with 10×10 cm^2 proportional tubes in between. After approximately 500 days of operation the detector has recorded on paper tape 11 events attributed to neutrino interactions in the detector and 6 events -- 3 of them fully contained -- that can be attributed to proton decay. The published figures of the 3 contained proton-decay candidates are shown in Fig. 48.

The Mont Blanc Collaboration using a more fine grained calorimeter (iron plate 0.5 cm and digital streamer tube), well calibrated, with electron, pion and neutrino beams (Figs. 49, 50) have collected over a period of 150 days the expected number of neutrino interactions in the detector and proton-decay candidate shown in Fig. 51. The event of Fig. 51 is interpreted as a proton-decay candidate. It is fully contained and is unlikely to be a neutrino interaction according to the analysis of the data collected at the CERN PS during the neutrino-beam exposure. The energy and topology of the event is compatible with one of the following types of proton decay

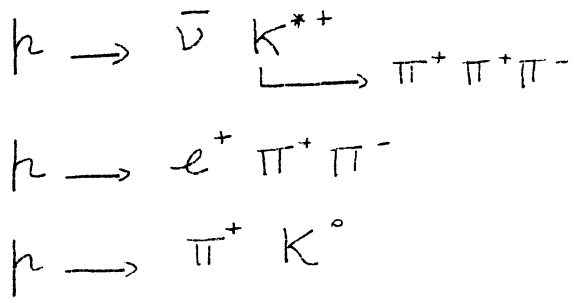

The IMB Collaboration very recently have presented the first results obtained with their detector that uses water calorimetry (Fig. 52). The detector has recorded 160 neutrino interactions and no candidates for proton decay in the $e^+\pi^0$ channel. The expected pattern of photomultipliers for a simulated $p \to \pi^0 e^+$ event is shown in Fig. 53. This last result puts a severe lower limit on the proton lifetime, which is

$$\tau_p > 2 \times 10^{30} \text{ years} \quad \text{for a free proton}$$

$$\tau_p > 6 \times 10^{30} \text{ years} \quad \text{for a proton bound in the nuclei}$$

The situation of the proton lifetime experiments is evolving very fast and the different technical solutions are just demonstrating their capability of detecting proton decay in matter. In my opinion in less than one year from now the prediction of SU(5) will be checked at a good level of confidence, and a critical analysis of the results will indicate which way to follow in order to continue the search for proton decay beyond the limit of SU(5). It is interesting to note that the future detectors for proton-decay experiment rely entirely on refined calorimetry techniques; probably the large tonnage of the IMB detector can hardly be increased and future experiments will try to improve on the product of the amount of material times the efficiency for the different proton-decay channels.

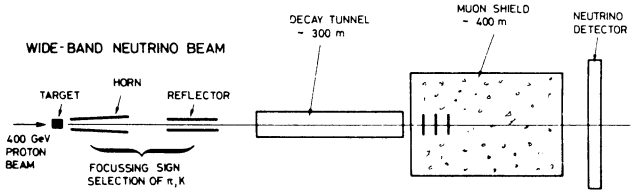

Fig. 1 Schematic view of the neutrino Wide Band Beam (WBB) layout

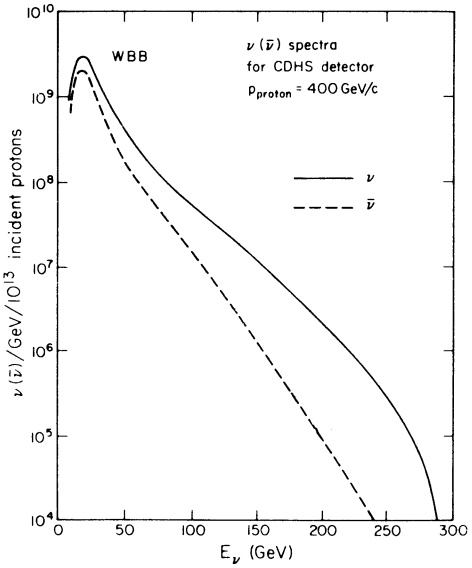

Fig. 2 Energy spectrum of CERN SPS neutrino WBB

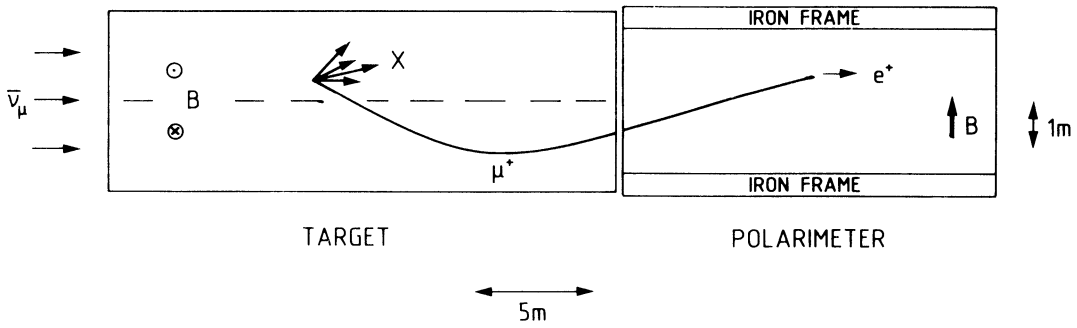

a) Layout of the μ^+ polarization experiment showing the CDHS neutrino detector used as a target and the CHARM fine-grain calorimeter used as a polarimeter.

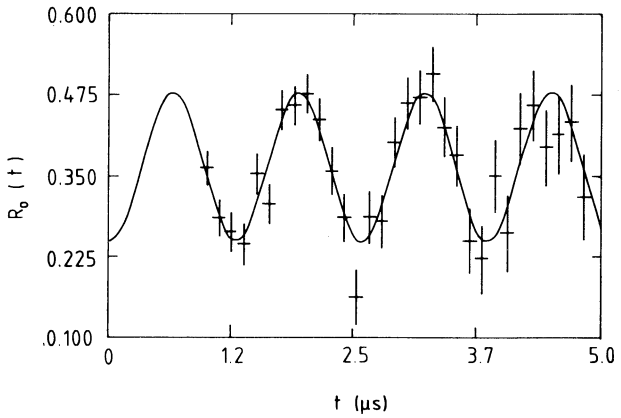

b) Observed time dependence of the relative backward-forward positron (from μ^+ decay) oscillation amplitude, $R_0(t) = [N_B(t) - N_F(t)]/[N_B(t) + N_F(t)] = R_0 \cos(\omega t + \phi) + R_1$.

Fig. 3

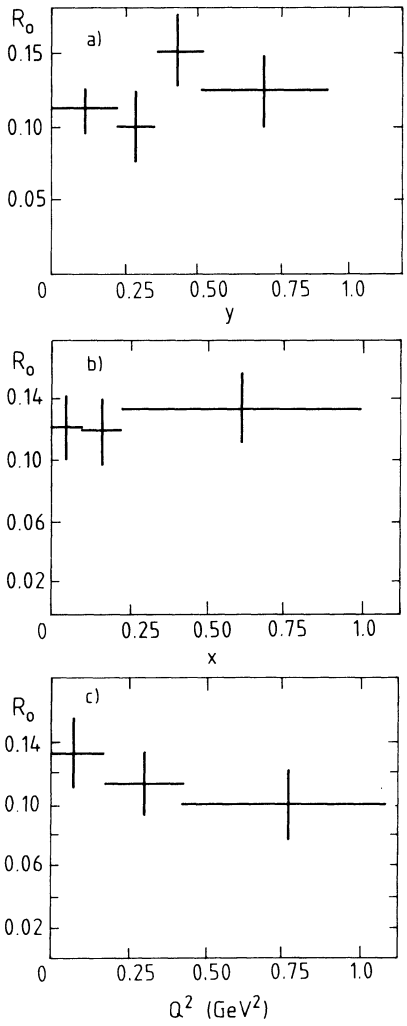

Fig. 4 Measured oscillation amplitude R_0: a) as a function of the inelasticity $y = E_h/E_\nu$; b) as a function of $x = Q^2/2ME_x$; c) as a function of Q^2.

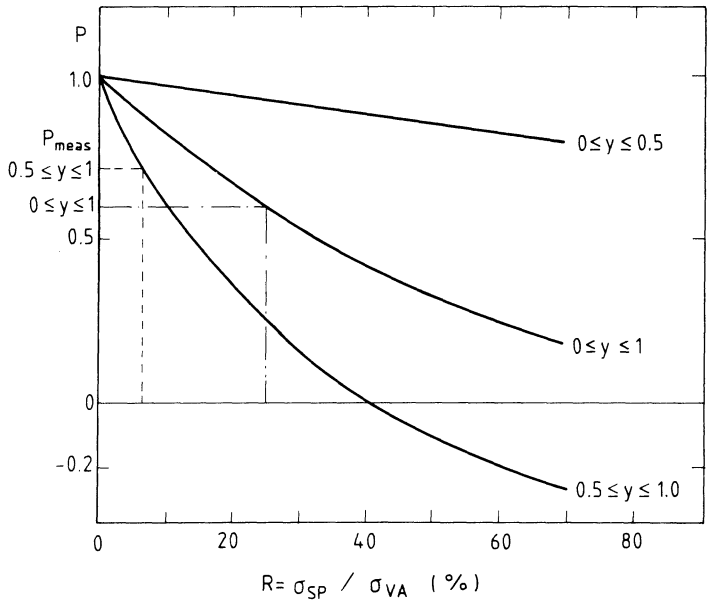

Fig. 5 Expected polarization for different regions of y as a function of S and P contributions, illustrating the sensitivity of the experiment.

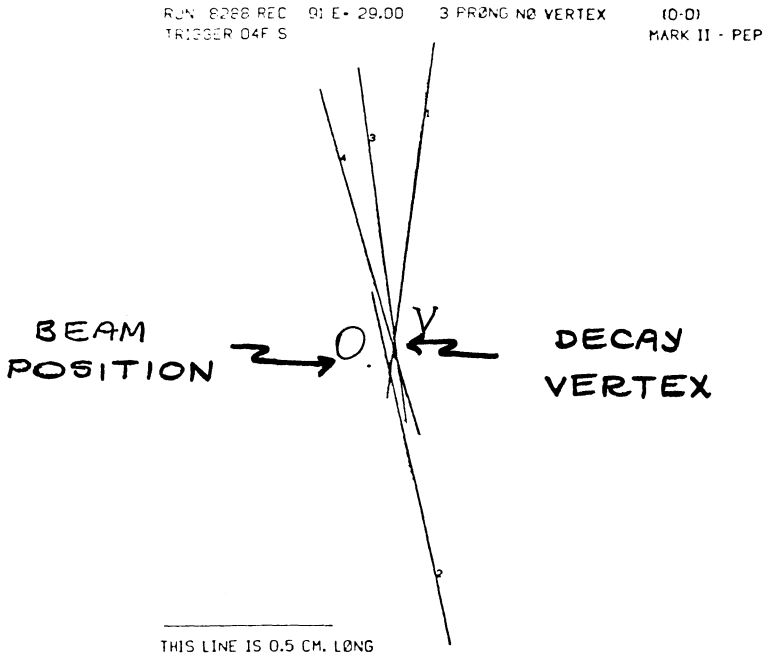

Fig. 6 Geometry of the τ decay. The topology of the τ decays is one-prong against three-prongs decay.

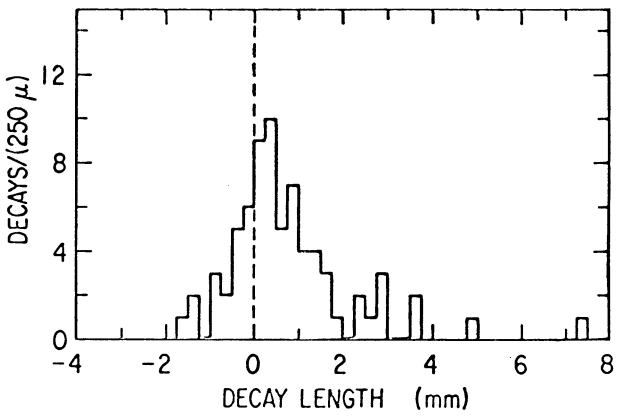

Fig. 7 Distribution of the τ decay lengths in the Mark II experiment

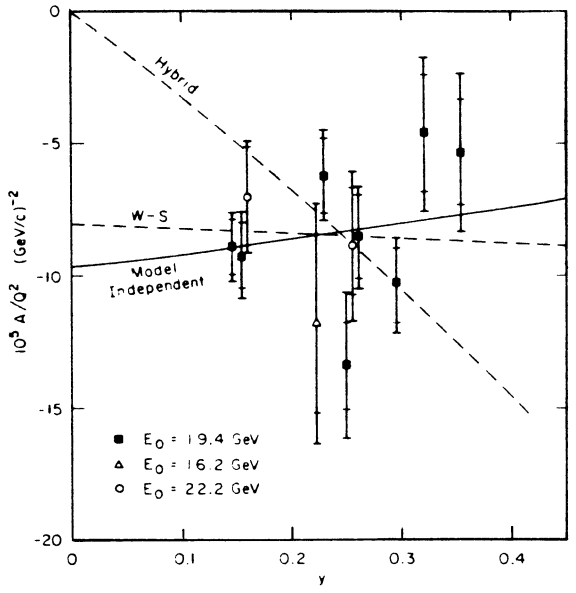

Fig. 8 Asymmetries measured at three incident electron energies are plotted against the inelasticity $y = (E_0 - E')/E_0$

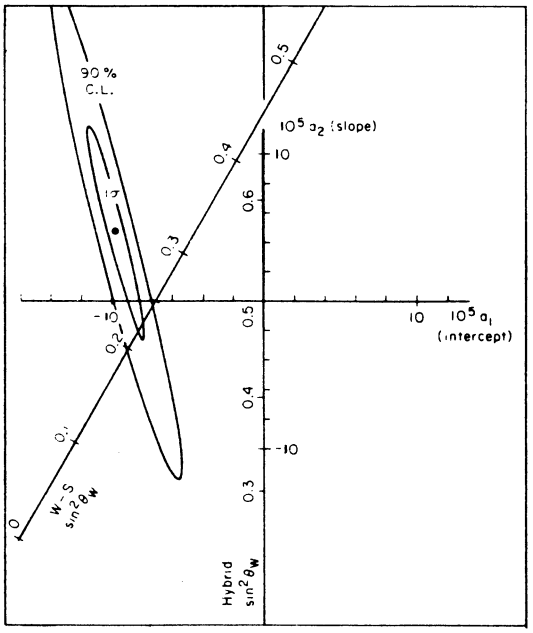

Fig. 9 The solid dot and the associated ellipses represent the fit to Eq. (5)

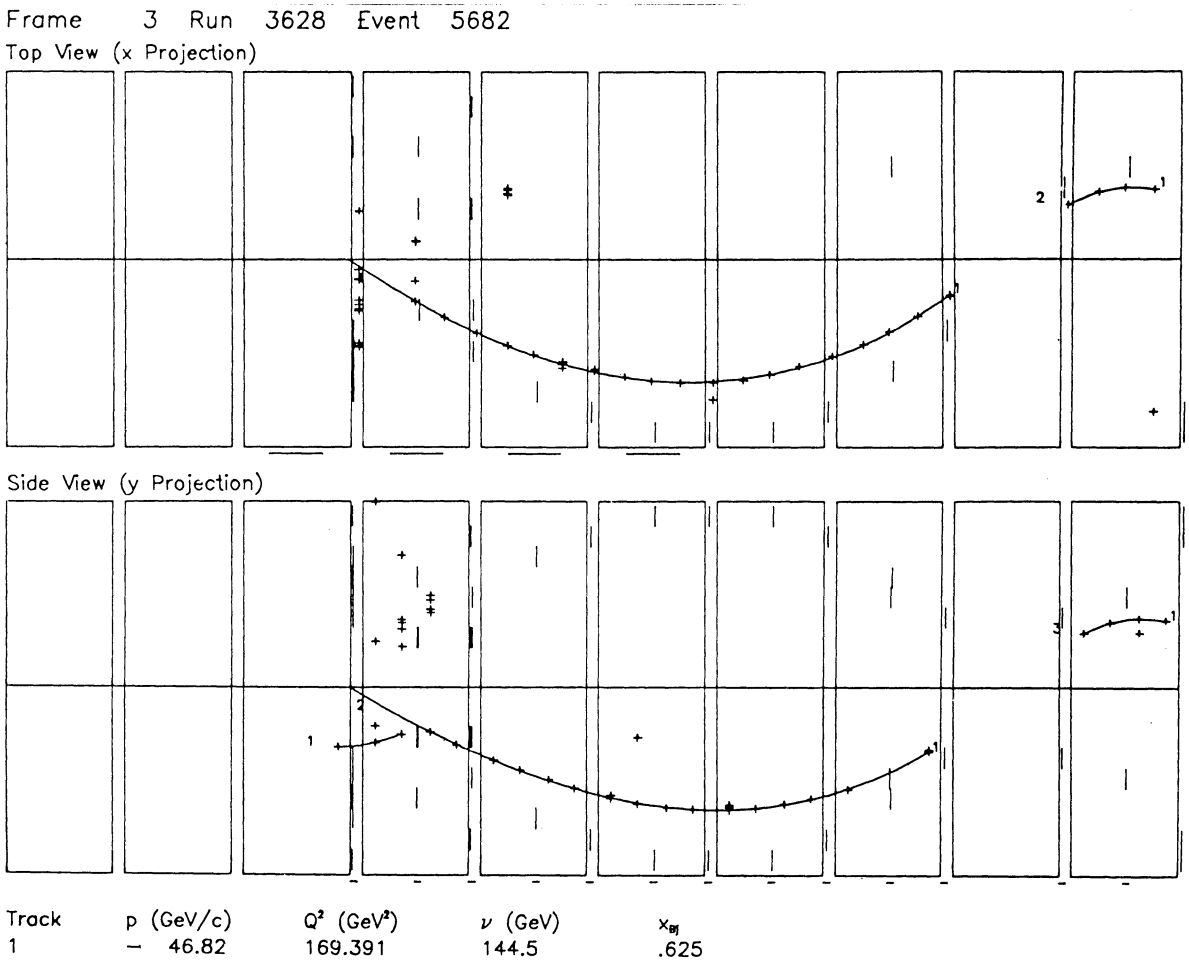

Fig. 10 On-line display of an event of deep inelastic μC scattering in the BCDMS apparatus

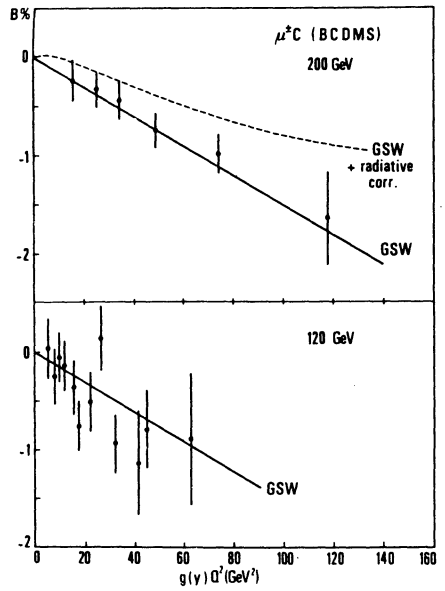

Fig. 11 The $\mu^{\pm}$ beam asymmetries measured in deep inelastic μC scattering by the BCDMS Collaboration

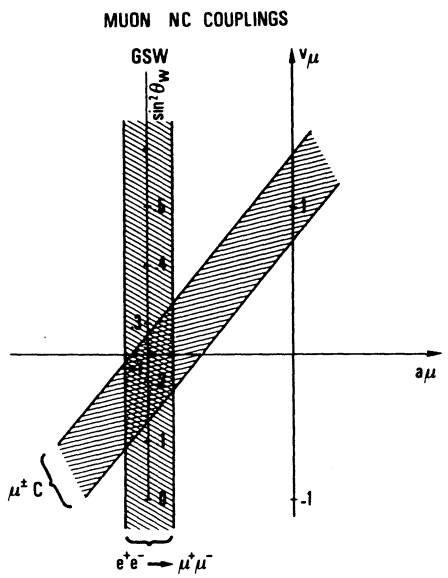

Fig. 12 Determination of the vector and axial muon couplings from μC deep inelastic scattering and the $e\bar{e} \to \mu\bar{\mu}$ asymmetries measured at PETRA

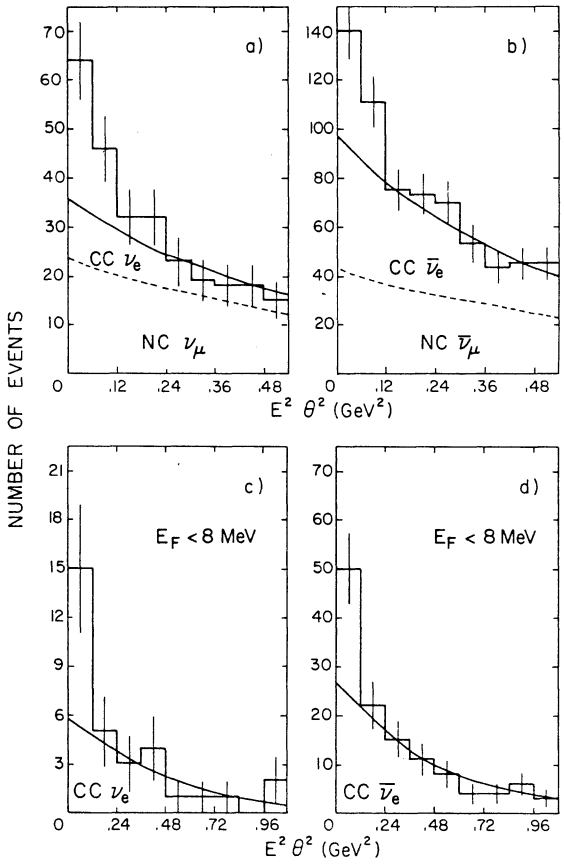

Fig. 13 Distribution of (a) the neutrino and (b) the antineutrino electron scattering events as a function of the electron kinematical variable $E^2\theta^2$

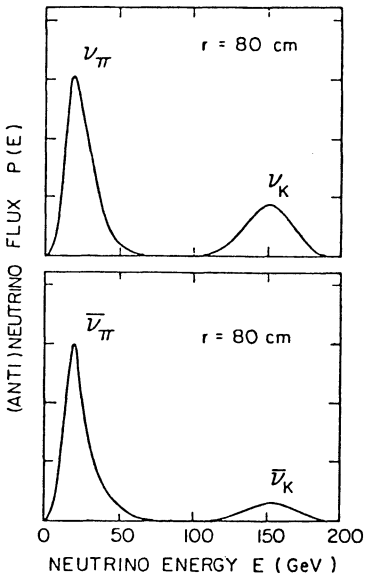

Fig. 15 Narrow-band beam (NBB) neutrino and antineutrino spectra at a fixed radial distance of 80 cm from the nominal beam line

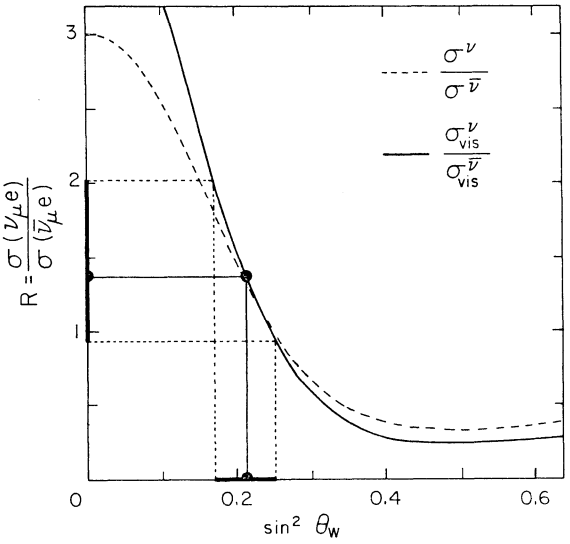

Fig. 14 Theoretical value of the ratio of the neutrino-electron scattering cross-section to that of antineutrino-electron scattering (dashed line). The full line gives the deviation from the total cross-section ratio introduced by the experimental acceptance of the CHARM detector. The solid dot is the experimental value.

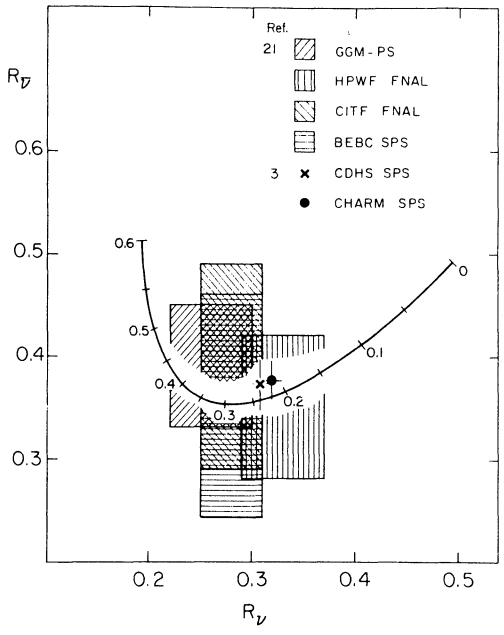

Fig. 16 Comparison of the results of various experiments on R and $\bar{R}$ with the Weinberg-Salam model. The data are taken with different cuts in shower energy. The cuts are $\sim$ 0 GeV, 4 GeV, 12 GeV, 15 GeV, and 20 GeV for the experiments GGM, HPWF, CITF, BEBC, and CDHS, respectively. The CHARM data have a cut at 2 GeV. Radiative corrections are not applied.

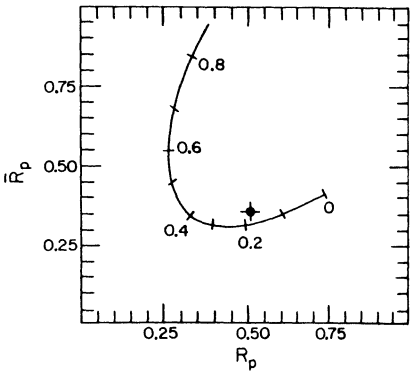

Fig. 17 Measured value of $\bar{R}_p$ versus the world average value of R_p

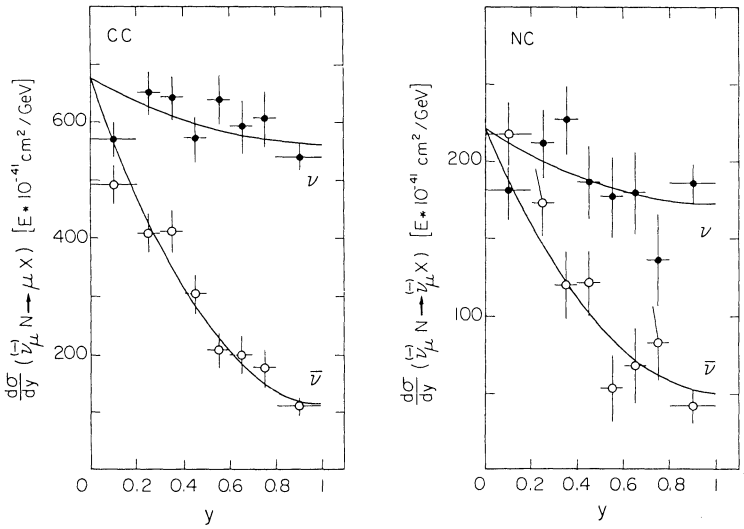

Fig. 18 Inelasticity distribution of the CC and NC events induced by neutrino and antineutrino NBB in the CHARM detector

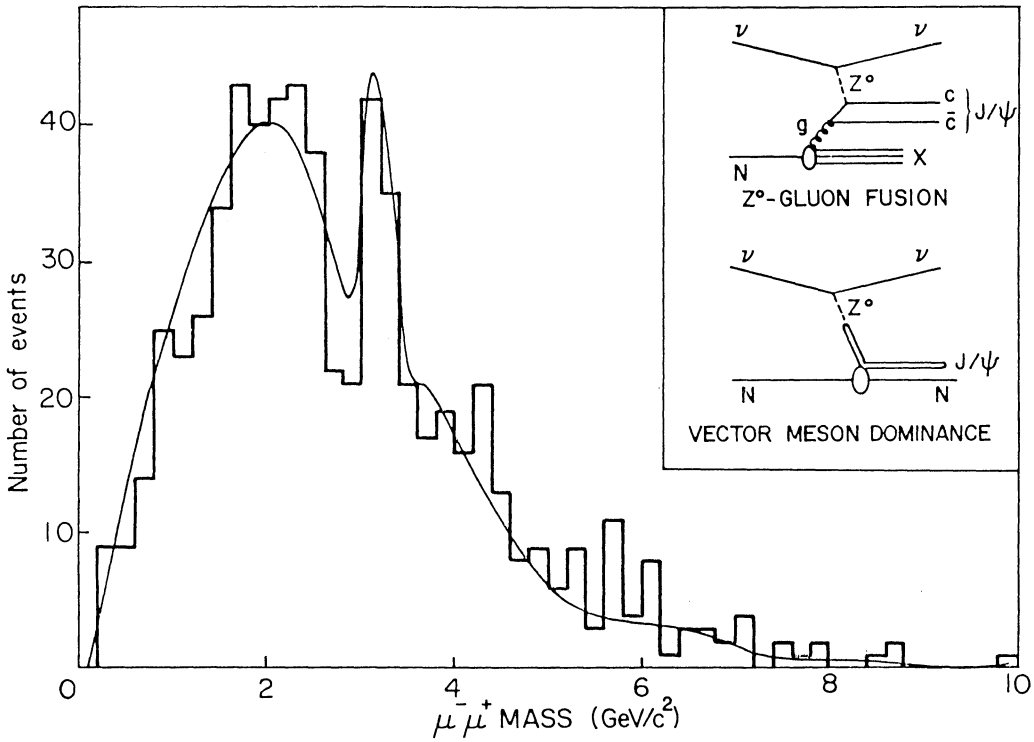

Fig. 19 Dimuon mass distribution of the events with μ^+ and μ^- in the final state produced by the WBB in the CDHS detector

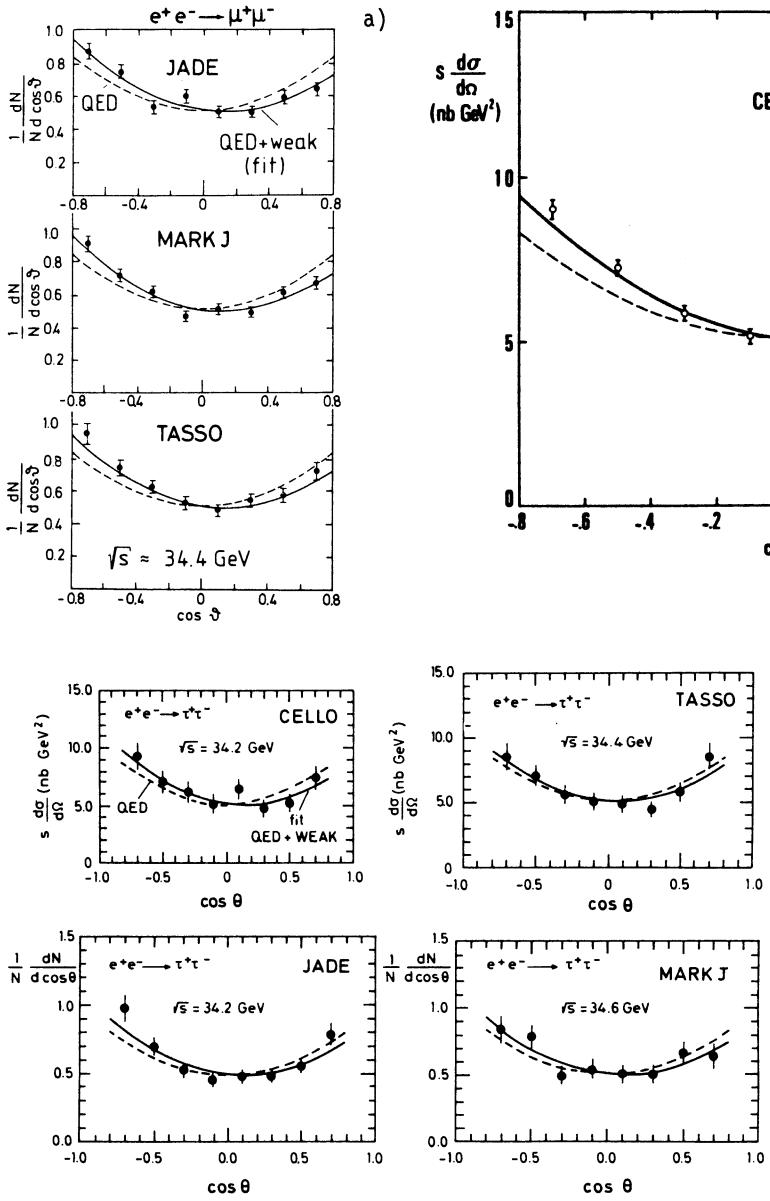

Fig. 20 a) Angular distribution of the reaction $e^+e^- \to \mu^+\mu^-$ measured by the PETRA experiments JADE, MARK-J, and TASSO. b) Compilation of PETRA high-energy data for the angular distribution of $e^+e^- \to \mu^+\mu^-$. c) Compilation of PETRA high-energy data for the angular distribution of $e^+e^- \to \tau^+\tau^-$. d) Angular distribution of $e^+e^- \to \tau^+\tau^-$ measured by CELLO, TASSO, JADE, and MARK-J at PETRA.

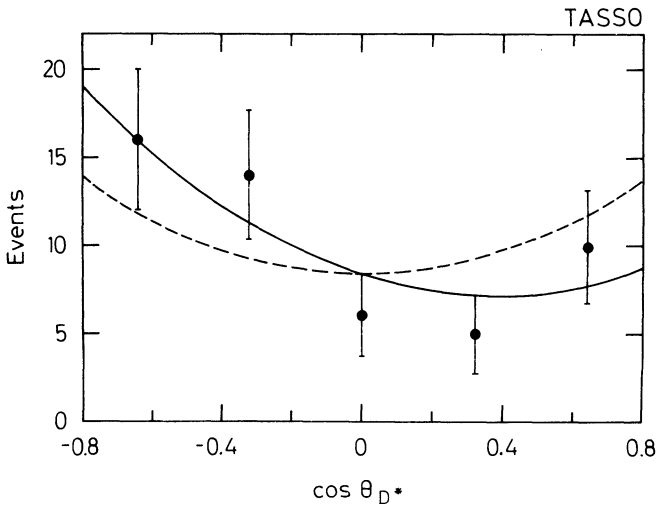

Fig. 21 Angular distribution of the reaction $e^+e^- \to D^*X$ measured by TASSO at PETRA

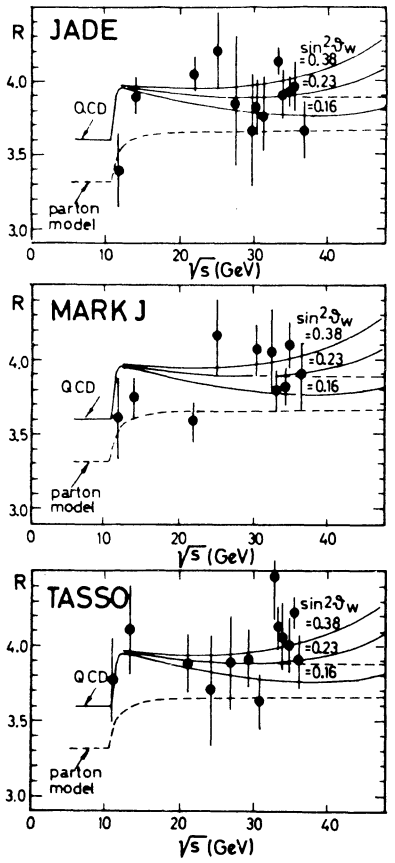

Fig. 22 Measurements of R as a function of the c.m. energy. The data from JADE, MARK-J and TASSO are compared with the prediction of the parton model and of QCD, where the weak interaction is included with different values of $\sin^2 \theta$.

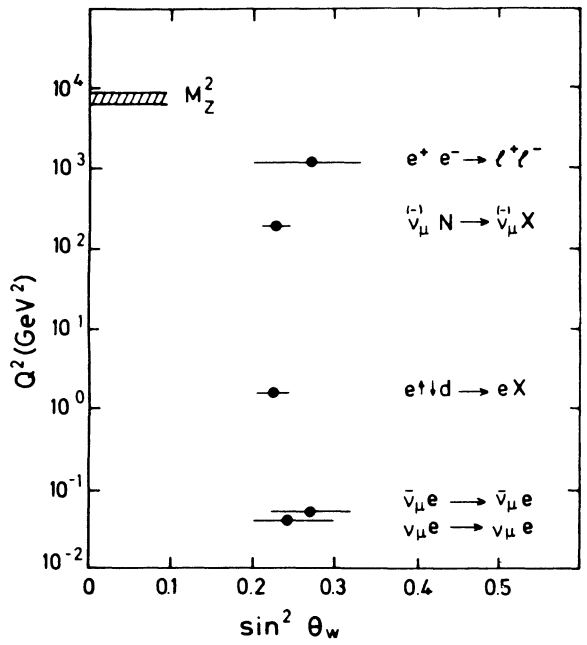

Fig. 23 The measurements of $\sin^2 \theta$ from different reactions are plotted as a function of Q^2. Note that, contrary to the other reactions, the Q^2 is mainly time-like in the $e^+e^- \to \ell^+\ell^-$ reactions.

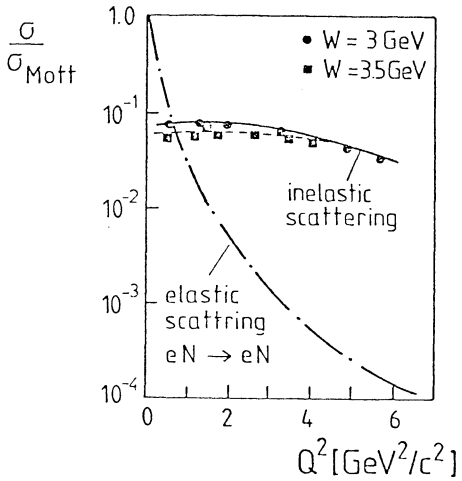

Fig. 24 The differential cross-section $d\sigma/dQ^2$ for the inclusive inelastic scattering of electrons from nucleons divided by the point-like cross-section as measured at SLAC in 1968/69. Also shown is the corresponding distribution for elastic scattering.

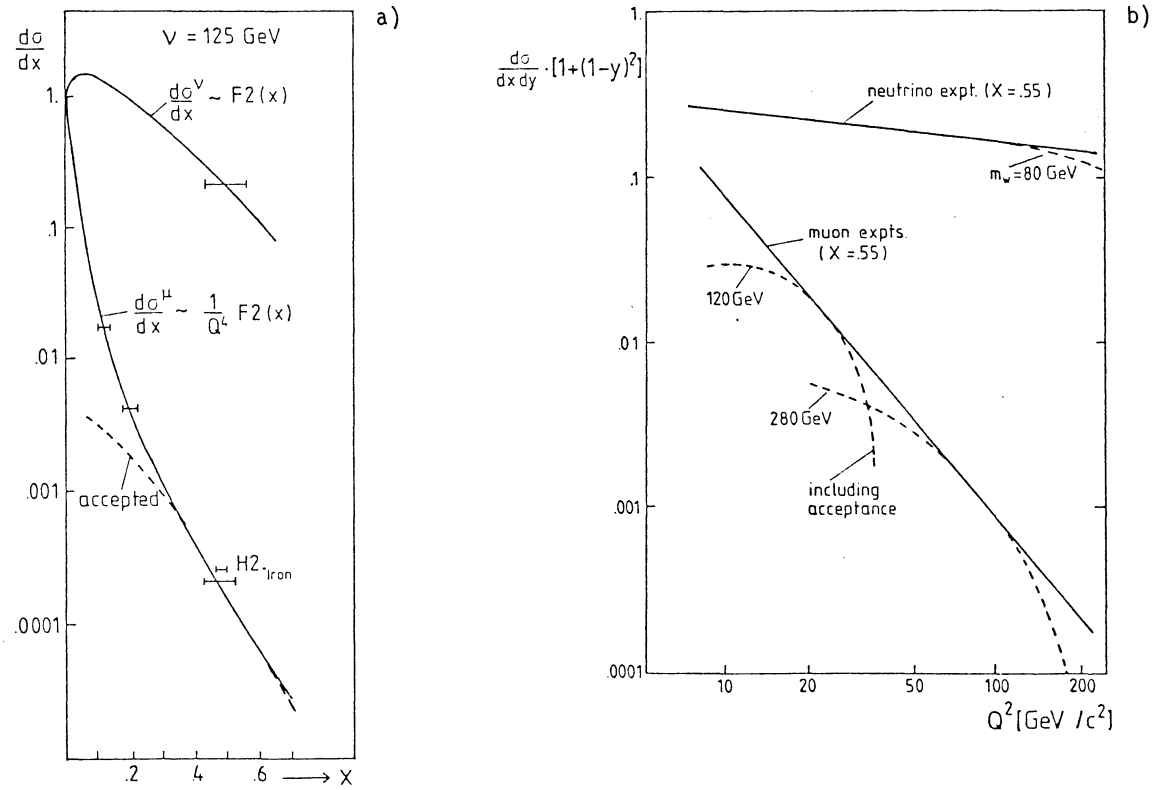

Fig. 25 a) $d\sigma/dx$ for neutrino and muon experiments at fixed ν. b) $(d\sigma/dxdy)[1 + (1-y)^2]$ for neutrino and muon experiments at fixed x as a function of Q^2.

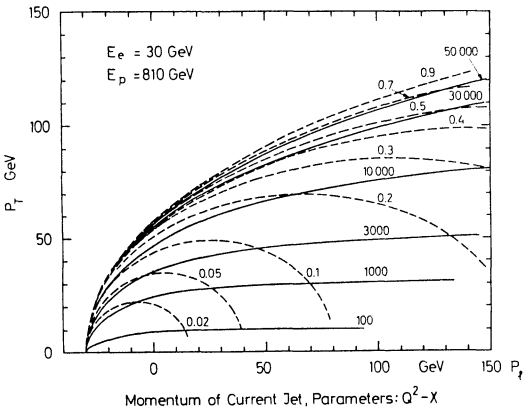

Fig. 26 Kinematical region of the electron-proton deep inelastic scattering allowed by the HERA project

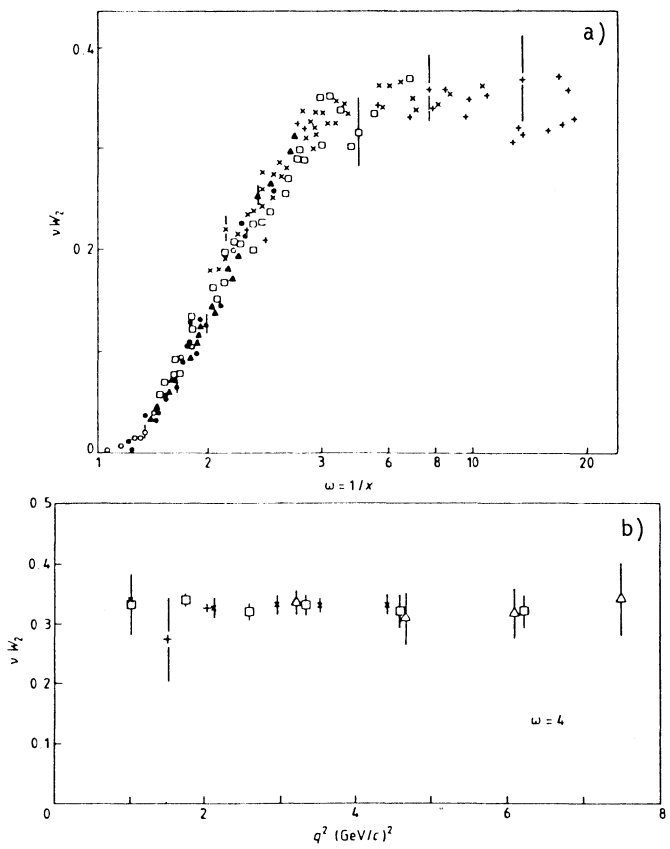

Fig. 27 a) Bjorken scaling: the structure function νW_2 plotted against $\omega = 1/x$ for different Q^2 values. b) The νW_2 structure function plotted against Q^2 for a fixed value of x = 0.25.

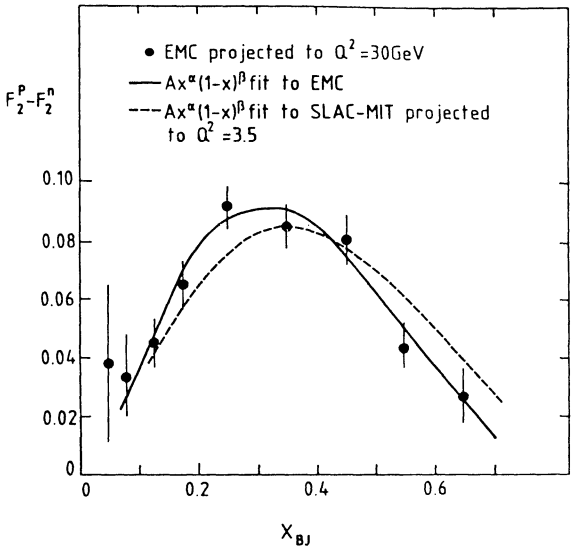

Fig. 28 Difference between the proton and neutron structure functions, F_2^p and F_2^n, versus the x variable at two Q^2 values (3.0, 3.5 GeV^2). The solid dots are experimental values from the EMC collaboration. The solid and dashed lines are fits to the CERN and SLAC data.

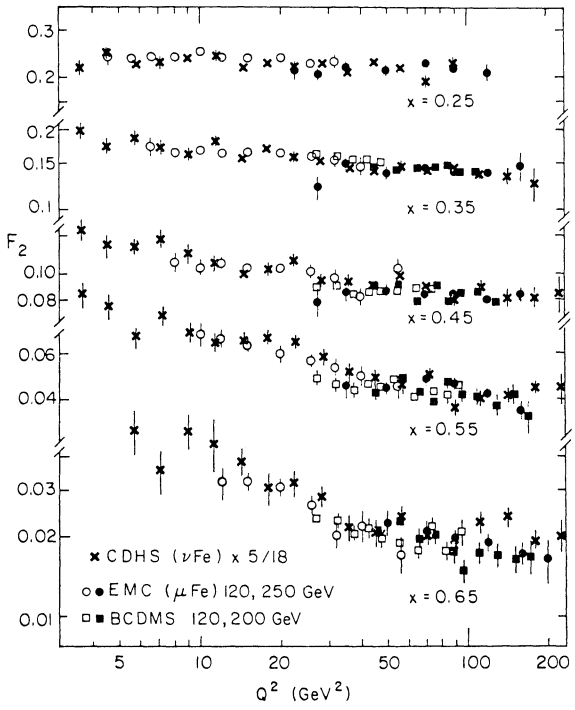

Fig. 29 Nucleon structure functions F_2 (x,Q^2) as measured in neutrino-iron scattering by the CDHS Collaboration (crosses), in muon-iron scattering by the EMC Collaboration (solid and empty dots), and in muon-carbon scattering by the BCDMS Collaboration (solid and empty squares). The relative normalization between neutrino and muon data is 5/18.

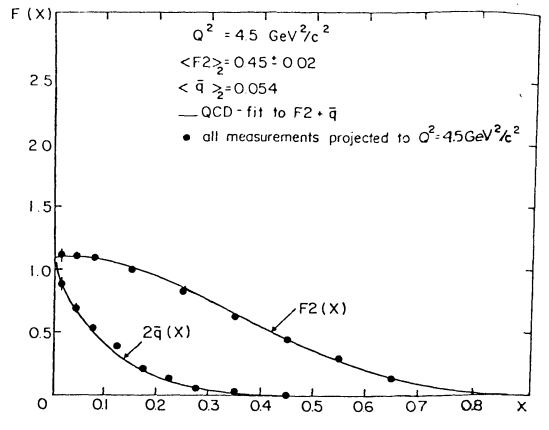

Fig. 30 Nucleon structure function $F_2(x)$ and antiquark nucleon x distribution as derived by the CDHS Collaboration projecting all Q^2 values at Q^2 = 4.5 GeV/c^2.

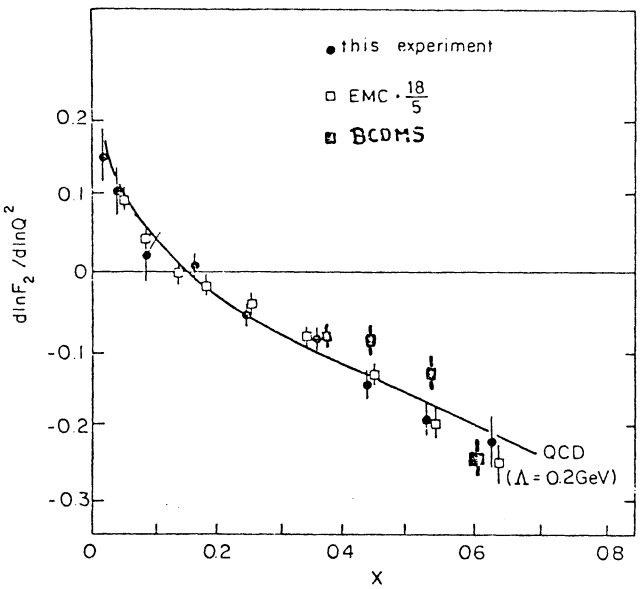

Fig. 31 The slopes d ln $F_2^{\nu N}$/d ln Q^2 for three experiments (CDHS, EMC, BCDMS) as obtained from power law fits to the whole Q^2 range. The full line is the QCD prediction for $\Lambda_{L.O.}$ = 0.2 GeV.

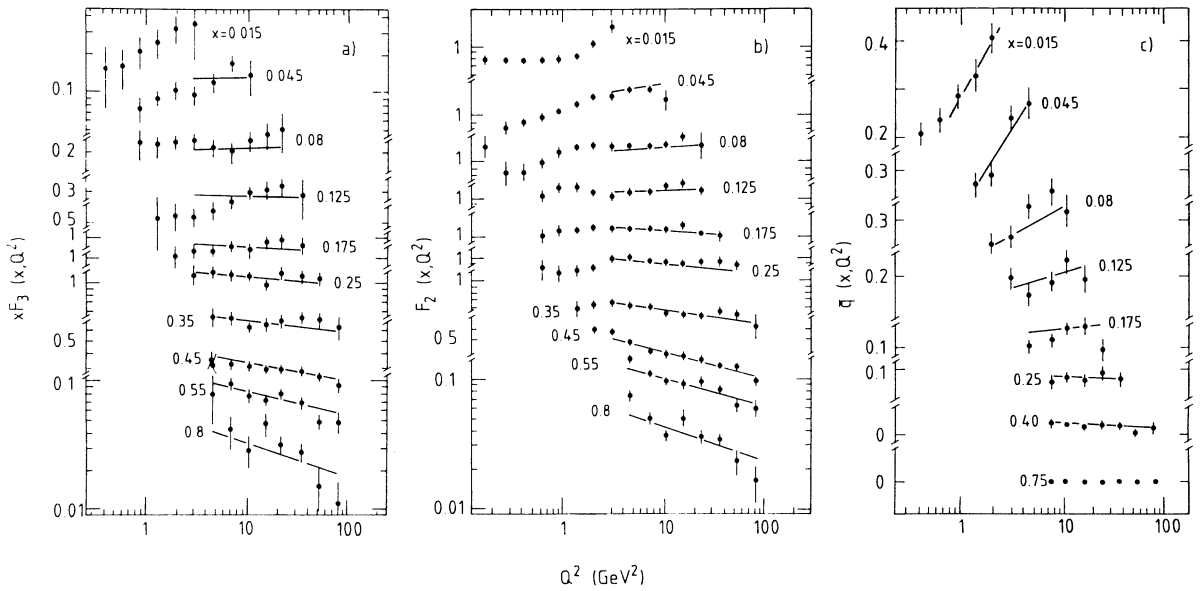

Fig. 32 Experimental results from the high statistics data of the CHARM Collaboration on nucleon structure functions derived from inclusive scattering of neutrinos on marble using the CERN SPS neutrino WBB

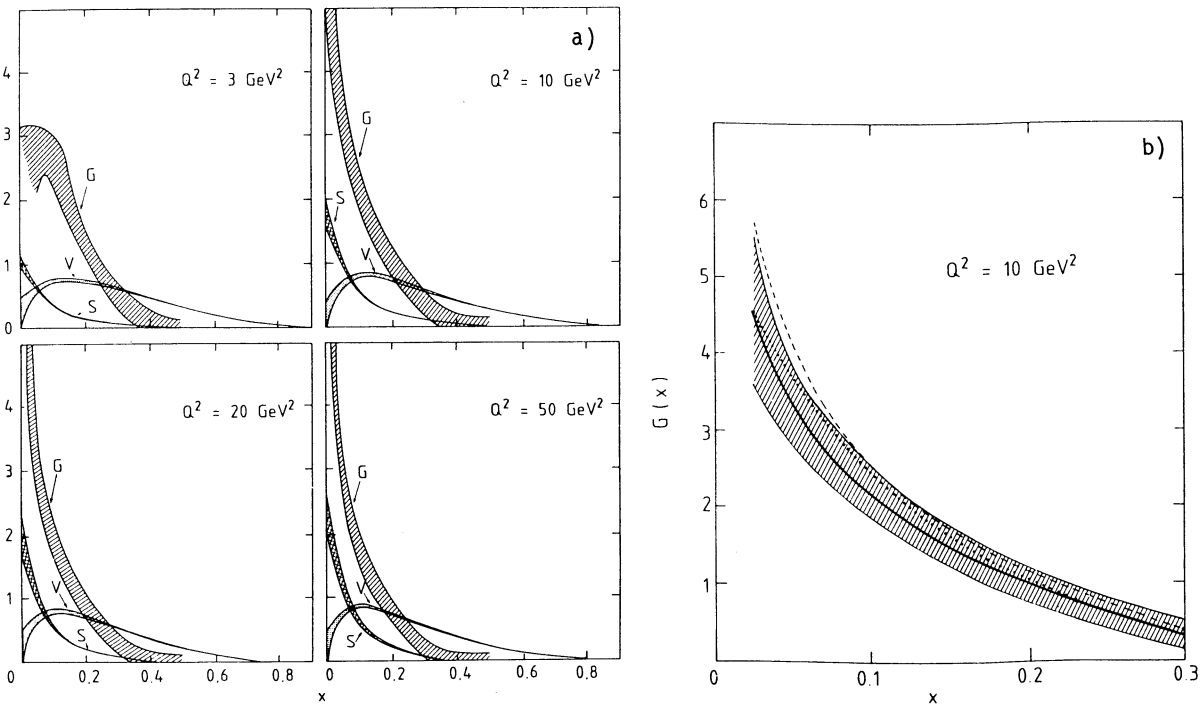

Fig. 33 a) Evolution of the x distribution of the gluons, and the valence and sea quarks as a function of Q^2 as derived by solving the Altarelli-Parisi equation. The experimental input is the high-statistics data from the CHARM Collaboration on inclusive neutrino-marble scattering. b) The gluon x distribution at Q^2 = 10 GeV/c^2.

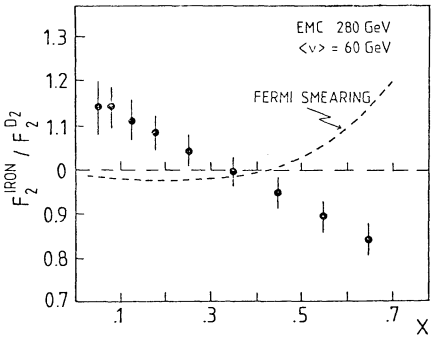

Fig. 34 The ratio of the structure functions $F_2^{\mu N}$ as measured on iron and deuterium as a function of x (EMC Collaboration). The dashed curve gives the expected effect due to Fermi motion.

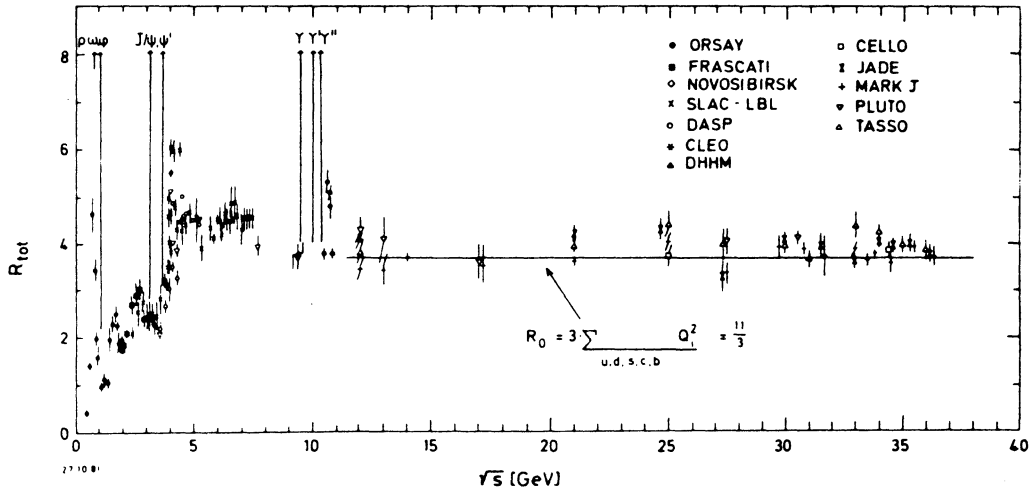

Fig. 35 Compilation of R values from the different PETRA experiments together with data from lower energies. The horizontal line indicates the quark parton model (QPM) prediction.

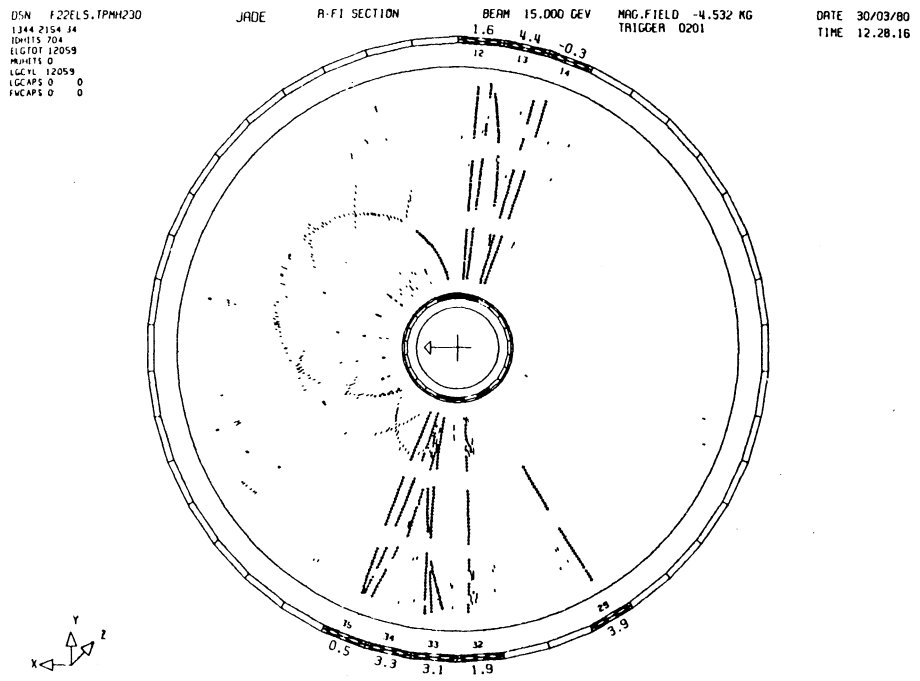

Fig. 36 Typical two-jet e^+e^- annihilation event as recorded in the JADE apparatus at PETRA

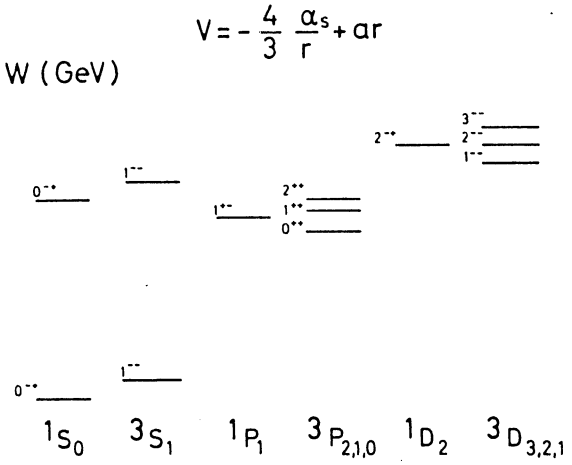

Fig. 37 Energy level predicted for a bound system of a quark-antiquark. The potential is given by a Coulomb term and an attractive rising component $V(R) = -4/3\ [\alpha_s(m^2)/r] + ar$.

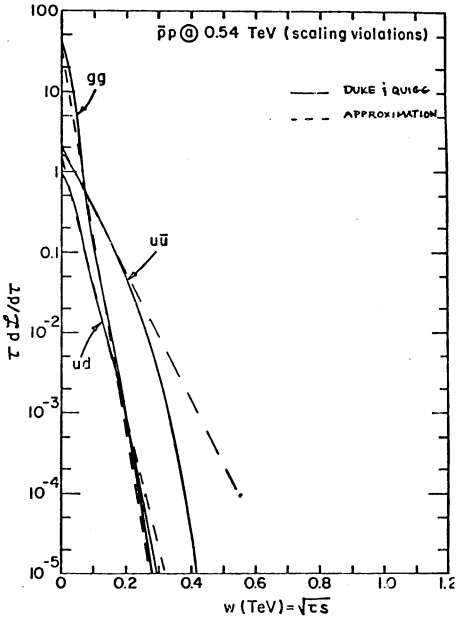

Fig. 38 Effective luminosity for three parton-parton subsystems (gg, $u\bar{u}$, ud), computed for the CERN SPS $p\bar{p}$ collider (E_{tot} = = 0.54 TeV) by the nucleon structure function (solid line due to Duke and Quigg). The dashed line is the result of an approximation for the product of the two-parton x distributions.

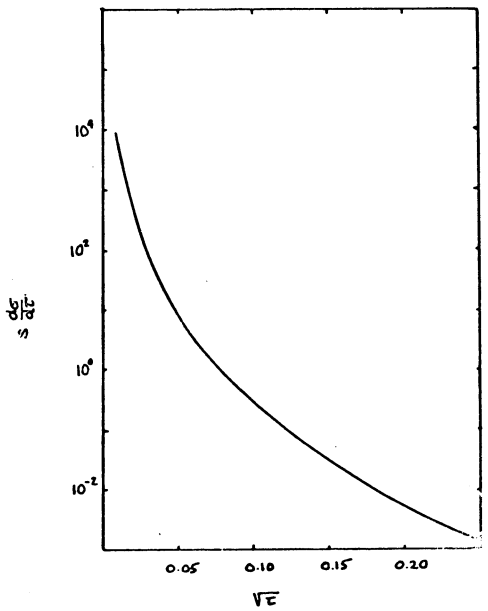

Fig. 39 Drell-Yan cross-section for lepton pair production at $p\bar{p}$ colliders as a function of the variable $\sqrt{\tau} = \sqrt{x_1 x_2}$

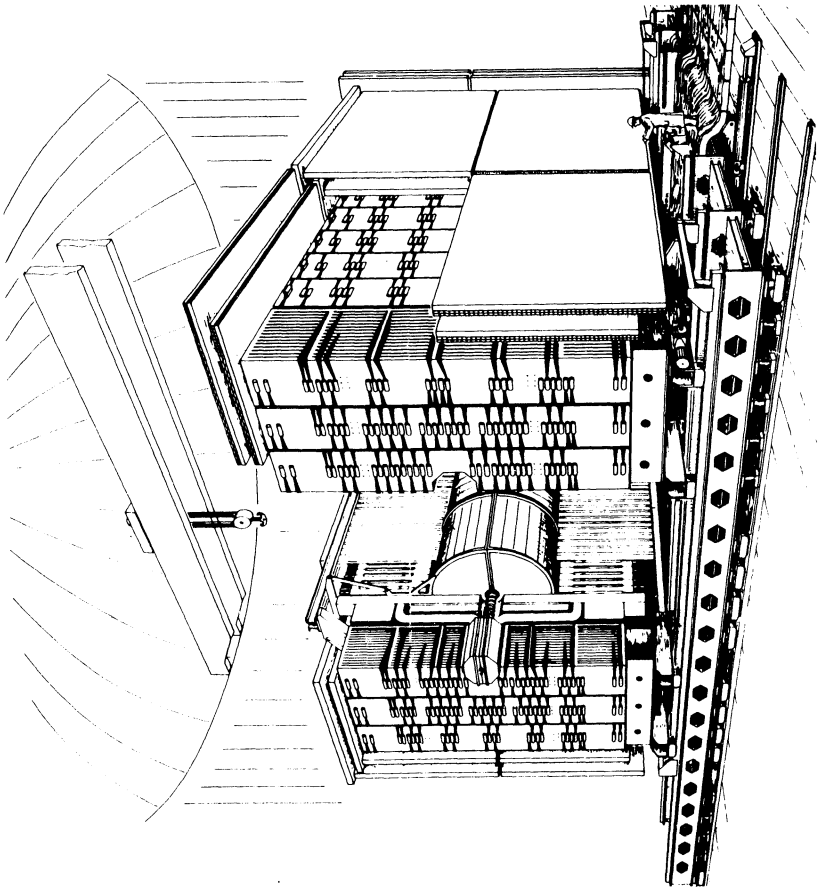

Fig. 40 A multitrack $p\bar{p}$ collision as recorded by the UA1 central tracking detector using a low-bias trigger in an early run of the CERN SPS $p\bar{p}$ collider

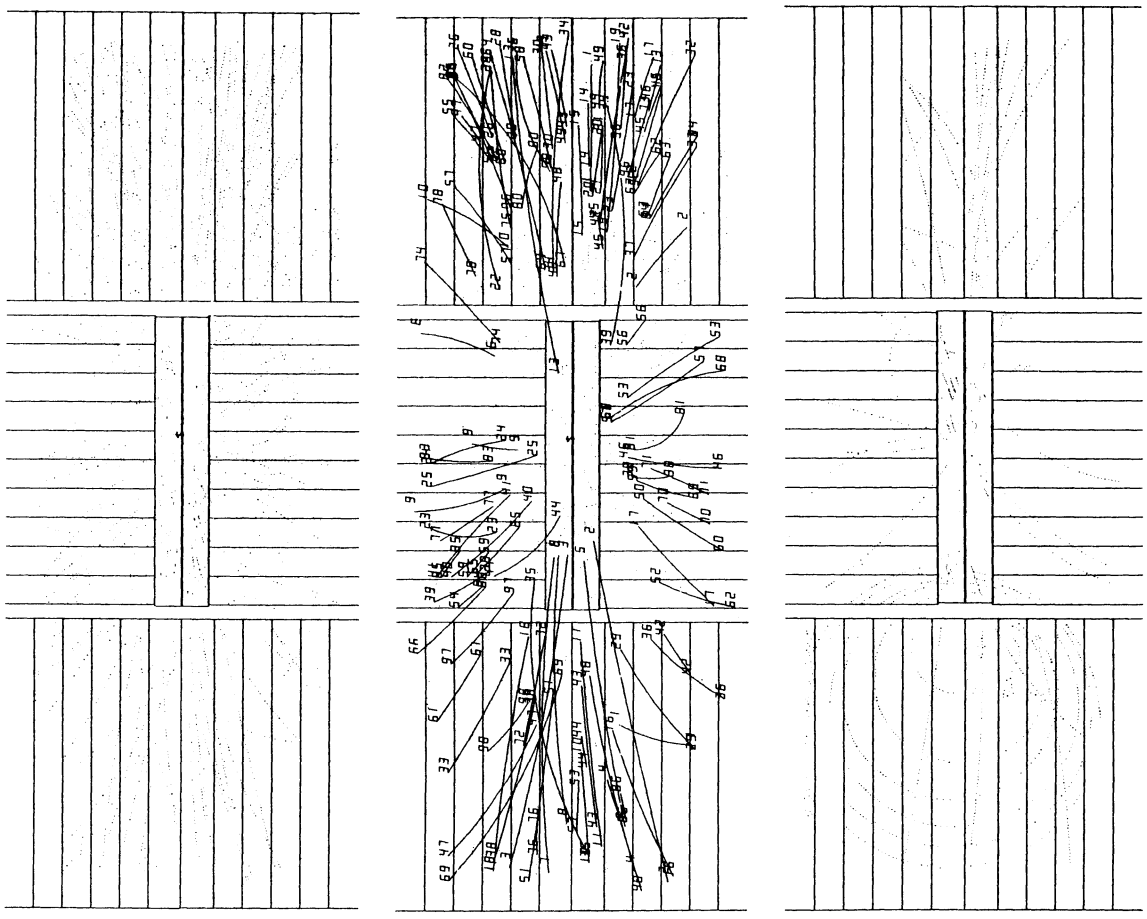

Fig. 41 Schematic view of the UA1 experimental set-up, showing the central detector, outer calorimeters, and muon chambers.

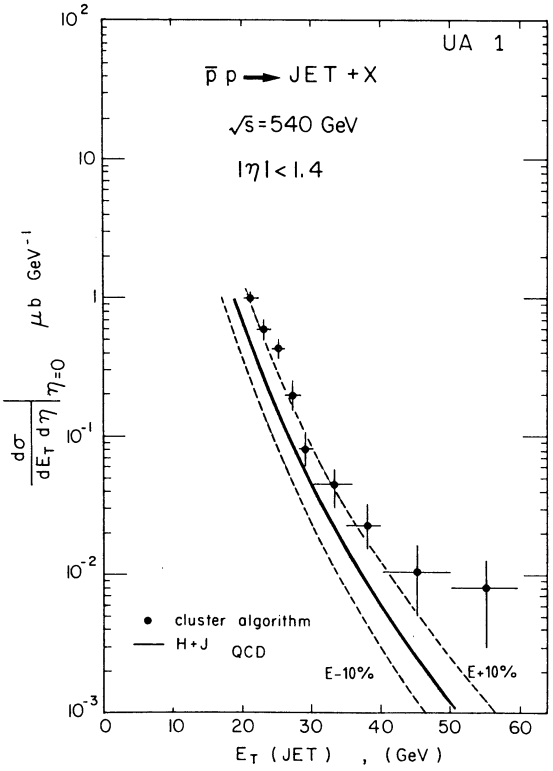

Fig. 42 Distribution of the jets as a function of the jet energy perpendicular to the $p\bar{p}$ beam line. The events have pseudorapidity $|\eta| \leq 1.4$. The solid line is the QCD prediction previously computed by Horgan and Jacob.

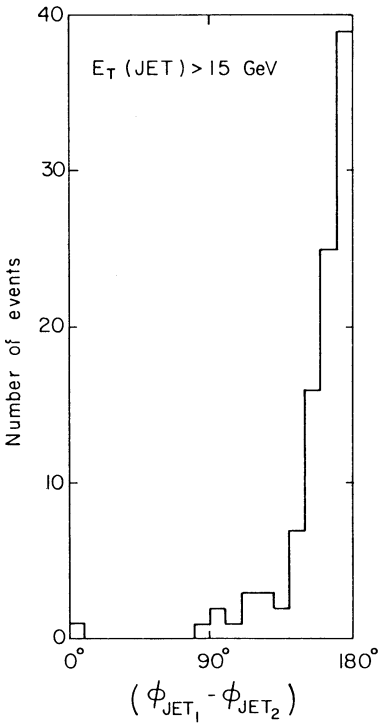

Fig. 43 Angular correlation of two jets of the same $p\bar{p}$ collision; the transverse energy for both jets is larger than 15 GeV. The events are measured in the UA1 detector.

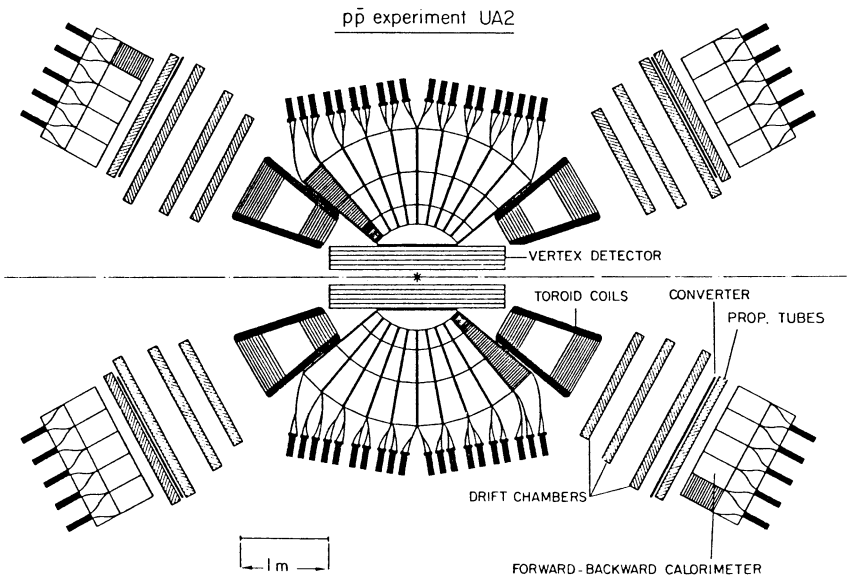

Fig. 44 The UA2 detector: schematic cross-section in the vertical plane containing the beam

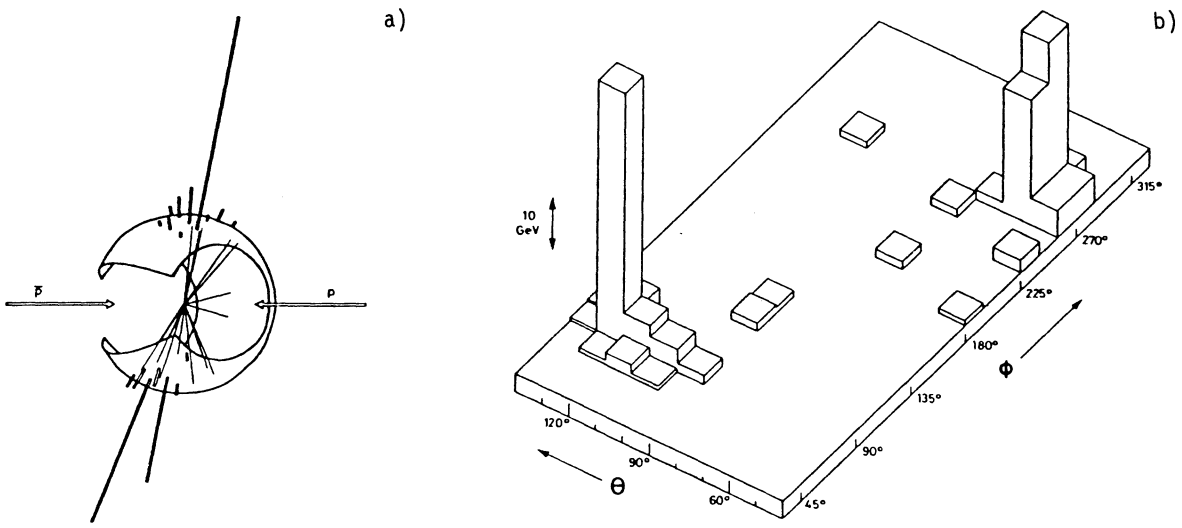

Fig. 45 Configuration of the UA2 event with the largest value of $\sum E_T$, 127 GeV (M = 140 GeV). a) Charged tracks pointing to the inner face of the central calorimeter are shown together with cell energies (indicated by heavy lines with lengths proportional to cell energies). b) The cell-energy distribution as a function of polar angle θ and azimuth ϕ.

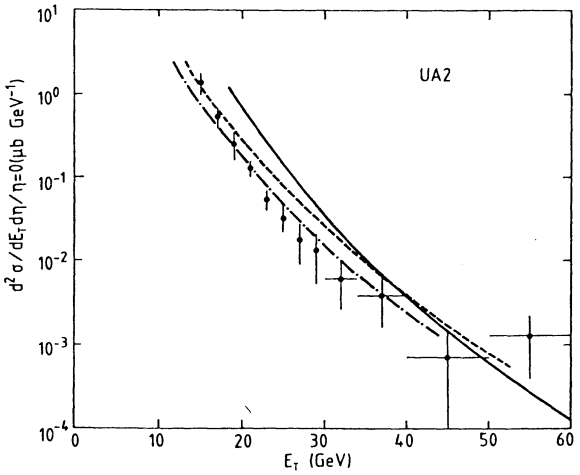

Fig. 46 Inclusive jet production cross-section as measured by the UA2 Collaboration. The solid line is the predicted QCD distribution computed by Horgan and Jacob with Λ = 0.5 GeV. The dashed and dash-dotted lines are recent calculations of Fox et al., and Paige et al., respectively, both using Λ = 0.1 GeV.

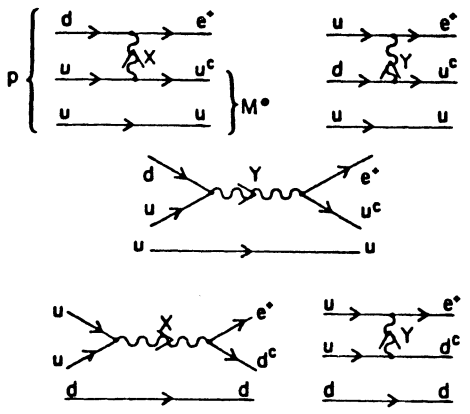

Fig. 47 Diagrams for $p \to e^+\bar{u}u$ or $e^+d\bar{d}$. The $\bar{q}q$ pair can form into neutral mesons such as π^0, ρ^0, ω, η, $\pi^+\pi^-$, etc. The first three diagrams also contribute to the decay of bound neutrons if the spectator u quark is replaced by a d.

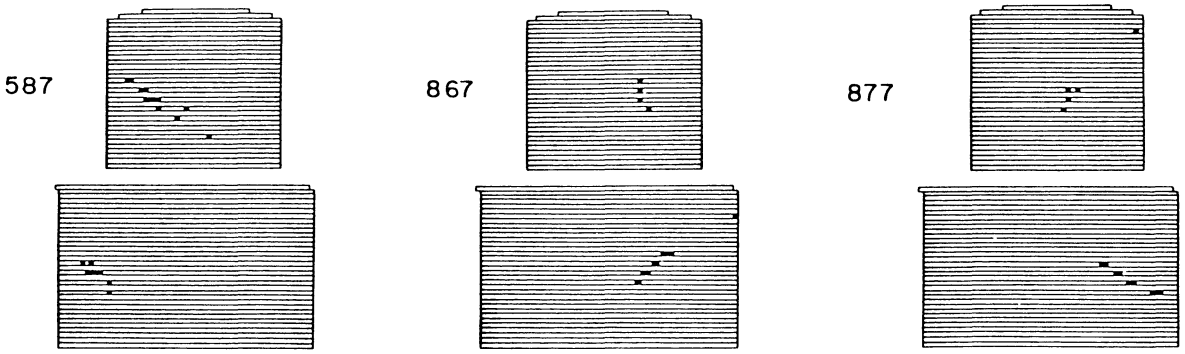

Fig. 48 Overall view of the three, confined baryon decay candidates observed in the Kolar gold field detector.

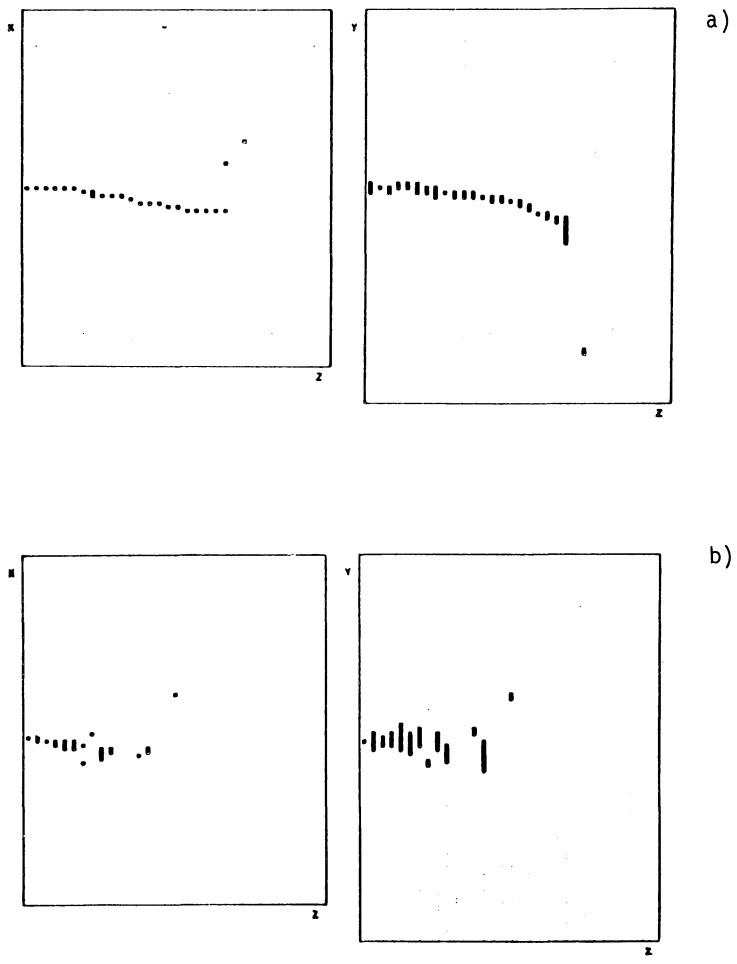

Fig. 49 a) Response of the NUSEX detector to a 500 MeV/c pion.
b) A 500 MeV/c electron in the NUSEX detector.

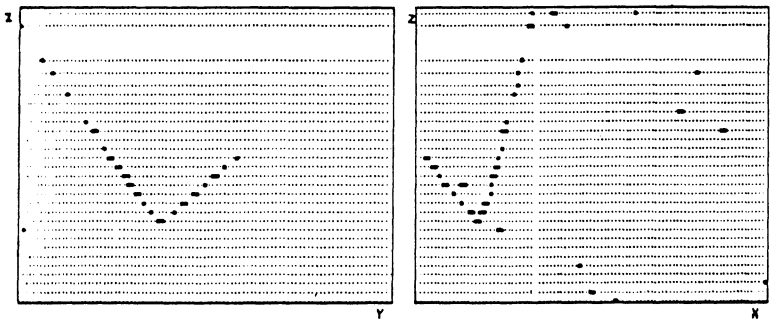

Fig. 50 Observation of a neutrino event in the NUSEX detector while exposed to a neutrino beam at CERN.

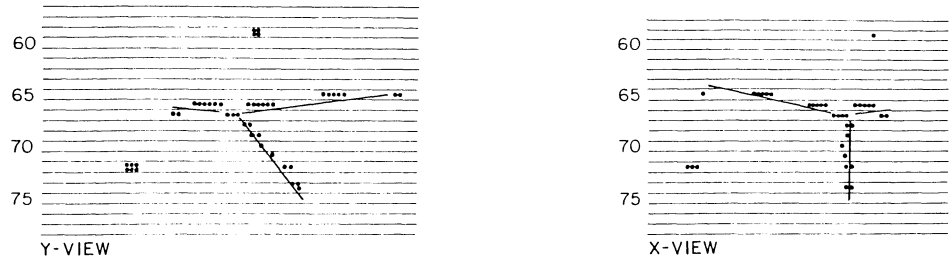

Fig. 51 A proton decay candidate observed in the NUSEX detector. It is not conclusively excluded that a neutrino interaction is the source of the event, though such a topology appears somewhat unlikely.

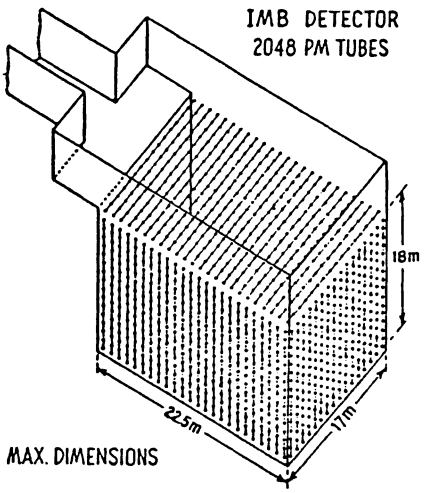

Fig. 52 Schematic of the Irvine-Michigan-Brookhaven (IMB) proton decay experiment located in a Morton salt mine. Approximately two thousand 5″ photomultipliers mounted on the faces of the cube view Čerenkov light produced in the pure water.

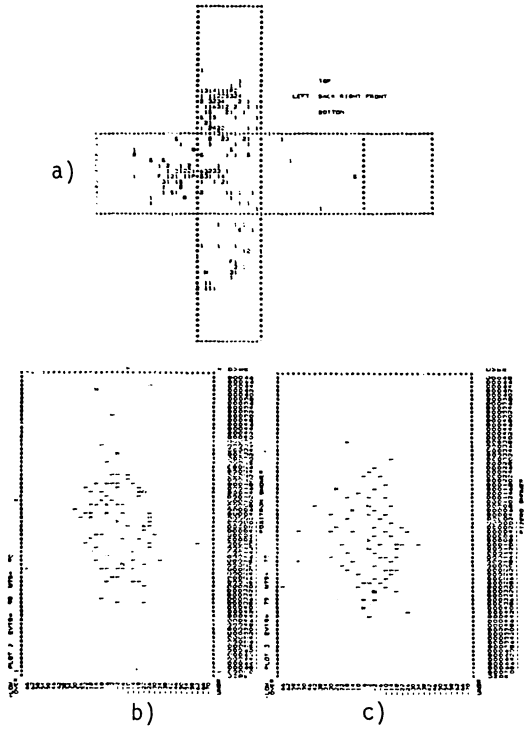

Fig. 53 A Monte Carlo representation of a $p \rightarrow e^{+}\pi^{0}$ decay in the IMB detector

BIBLIOGRAPHY

General

I.J.R. Aitchison and A.J.G. Hey, Gauge theories in particle physics: a practical introduction (Hilger, Bristol, 1982: Graduate Student Series in Physics).

C.H. Llewellyn Smith, Phys. Rep. 3C, 261 (1972).

L.B. Okun, Leptons and quarks (North-Holland, Amsterdam, 1982).

Section 1

S. Coleman, Proc. 13th School of Subnuclear Physics, Erice, Sicily, 1975 (ed. A. Zichichi) (Plenum Press, New York and London, 1977), part A, p. 297.

S.L. Glashow, J. Iliopoulos and L. Maiani, Phys. Rev. D 2, 1285 (1970).

J. Iliopoulos, CERN 76-11 (1976).

J. Iliopoulos, Proc. 1977 CERN-JINR School of Physics, Nafplion, Greece, CERN 77-18 (1977), p. 36.

L. Maiani, Proc. 1976 CERN School of Physics, Wépion, near Namur, Belgium, CERN 76-20 (1976), p. 23.

S. Weinberg, Phys. Rev. D 5, 1412 (1972).

Section 2

F. Büsser, Proc. Int. Conf. on Neutrino Physics and Astrophysics, Maui, Hawaii, 1981 (eds. R.J. Cence, E. Ma and A. Roberts) (Univ. of Hawaii, Honolulu, 1981), Vol. 2, p. 351.

M. Davier, Proc. 21st Int. Conf. on High Energy Physics, Paris, 1982, J. Phys. 43, Suppl. 12, C-3, 471 (1982).

J.A. Jaros, Proc. 21st Int. Conf. on High Energy Physics, Paris, 1982, J. Phys. 43, Suppl. 12, C-3, 106 (1982).

M. Jonker et al. (CHARM Collaboration), Phys. Lett. 86B, 229 (1979).

J.G. Morfin et al., Phys. Lett. 107B, 450 (1981).

L.B. Okun, Weak interactions of elementary particles (Pergamon, Oxford, 1965).

M.L. Perl, Phys. Rev. Lett. 35, 1489 (1975).

J. Steinberger, Proc. 1976 CERN School of Physics, Wépion, near Namur, Belgium, CERN 76-20 (1976), p. 57.

G.H. Trilling, Proc. 21st Int. Conf. on High Energy Physics, Paris, 1982, J. Phys. 43, Suppl. 12, C-3, 57 (1982).

Section 3

H. Abramowicz et al. (CDHS Collaboration), Phys. Lett. 102B, 67 (1981).

J.D. Burger, Proc. 21st Int. Conf. on High Energy Physics, Paris, 1982, J. Phys. 43, Suppl. 12, C-3, 63 (1982).

M. Davier, Proc. 21st Int. Conf. on High Energy Physics, Paris, 1982, J. Phys. 43, Suppl. 12, C-3, 471 (1982).

P. Hung and J. Sakurai, Ann. Rev. Nucl. Part. Sci. 31, 375 (1981).

M. Jonker et al. (CHARM Collaboration), Phys. Lett. 105B, 242 (1981).

J.E. Kim et al., Rev. Mod. Phys. 52, 211 (1981).

F. Niebergall, Neutrino '82, Proc. 12th Int. Neutrino Conf., Balatonfüred, Hungary, 1982 (eds. A. Frenkel and L. Jensk) (Central Research Institute for Physics, Budapest, 1982), Vol. 2, p. 62.

E. Paschos and L. Wolfenstein, Phys. Rev. D 7, 91 (1973).

C. Prescott et al., Phys. Lett. 77B, 347 (1978).

G. Wolf, Selected topics on e^+e^- physics, DESY 80-13 (1980).

Section 4

J.J. Aubert et al., Phys. Lett. 105B, 315 (1981).

J.J. Aubert et al., Phys. Lett. 105B, 322 (1981).

M. Banner et al. (UA2 Collaboration), Phys. Lett. 115B, 59 (1982).

W. Bartel (JADE Collaboration), DESY 82-060 (1982).

H.J. Behrend (CELLO Collaboration), DESY 82-061 (1982).

J.D. Bjorken, Phys. Rev. 179, 1547 (1969).

D. Bollini et al., Phys. Lett. 104B, 403 (1981).

R. Brandelik et al. (TASSO Collaboration), Phys. Lett. 94B, 437 (1980).

J.G.H. de Groot et al., Z. Phys. C1, 143 (1979).

F. Eisele, Proc. 21st Int. Conf. on High Energy Physics, Paris 1982, J. Phys. 43, Suppl. 12, C-3, 337 (1982).

D. Hardt, Proc. 21st Int. Conf. on High Energy Physics, Paris 1982, J. Phys. 43, Suppl. 12, C-3, 5 (1982).

R. Horgan and M. Jacob, Nucl. Phys. B179, 441 (1981).

J. Lefrançois, Proc. 20th Int. Conf. on High Energy Physics, Madison, 1980 (Amer. Inst. Phys., New York, 1981), p. 1318.

A. Martin, Proc. 21st Int. Conf. on High Energy Physics, Paris, 1982, J. Phys. 43, Suppl. 12, C-3, 96 (1982).

A. Michelini, Proc. EPS Int. Conf. on High Energy Physics, Lisbon, Portugal, 1981 (eds. J. Dias de Deus and J. Soffer) (EPS, Lisbon, 1982), p. 261.

J.P. Repellin (UA2 Collaboration), Proc. 21st Int. Conf. on High Energy Physics, Paris, 1982, J. Phys. 43, Suppl. 12, C-3, 571 (1982).

C. Rubbia, P. McIntyre and D. Cline, Proc. Int. Neutrino Conf. Aachen, 1976 (Vieweg, Braunschweig, 1977), p. 683.

A. Silverman, Proc. 10th Int. Symposium on Lepton and Photon Interactions at High Energies, Bonn, 1981 (ed. W. Pfeil) (Phys. Inst., Univ. Bonn, 1981), p. 138.

G. Smadja, Proc. 10th Int. Symposium on Lepton and Photon Interactions at High Energies, Bonn, 1981 (ed. W. Pfeil) (Phys. Inst., Univ. Bonn, 1981), p. 444.

M. Strovink, Proc. 10th Int. Symposium on Lepton and Photon Interactions at High Energies, Bonn, 1981 (ed. W. Pfeil) (Phys. Inst., Univ. Bonn, 1981), p. 594.

G. Wolf, Proc. 21st Int. Conf. on High Energy Physics, Paris, 1982, J. Phys. 43, Suppl. 12, C-3, 525 (1982).

Section 5

J. Ellis, Ecole d'Eté de physique théorique, Les Houches, France, August 1981 and preprint CERN TH-3174 (1981) (Proc. to be published by North Holland, Amsterdam).

L. Sulak, Proc. 21st Int. Conf. on High Energy Physics, Paris, 1982, J. Phys. 43, Suppl. 12, C-3, 205 (1982).

H.H. Williams, Grand unification, proton decay and neutrino oscillations, talk presented at the SLAC Summer Institute on Particle Physics, August 1982.